VILNIUS UNIVERSITY

VAIDAS JUKNEVIČIUS

SPATIO-TEMPORAL BEHAVIOR IN CONTINUUM SURFACE GROWTH MODELS

Doctoral dissertation
Physical Sciences, Physics (02P)

Vilnius, 2017

The research was performed in 2012 - 2016 at Vilnius university.

Scientific supervisor:

Habil. Dr. Bronislovas Kaulakys (Vilnius University, Physical Sciences, Physics – 02 P)

VILNIAUS UNIVERSITETAS

VAIDAS JUKNEVIČIUS

ERDVININIS IR LAIKINIS ELGESYS PAVIRŠIŲ AUGIMO KONTINUUMO MODELIUOSE

Daktaro disertacija
Fiziniai mokslai, fizika (02 P)

Vilnius, 2017

Disertacija rengta 2012 - 2016 Vilniaus universitete.

Mokslinis vadovas:

habil. dr. Bronislovas Kaulakys (Vilniaus universitetas, fiziniai mokslai, fizika – 02 P)

Contents

List of abbreviations

BD	Ballistic deposition
EW	Edwards-Wilkinson equation or universality class
FFT	Fast Fourier transform
gKS	Generalized Kuramoto-Sivashinsky equation
KPZ	Kardar-Parisi-Zhang equation or universality class
KS	Kuramoto-Sivashinsky equation
lhs	left-hand side (mostly referring to the position of a term in a mathematical expression)
PDE	Partial differential equation
RG	Renormalization group
rhs	right-hand side (see 'lhs')
2D	Two-dimensional
3D	Three-dimensional

Preface

Various surfaces found in nature, produced in laboratories or manufactured during technological processes are interesting and important not only because of their vast practical applications, but also from the theoretical point of view — as complex systems evolving in non-equilibrium conditions.

The geometric form of the surfaces often determines their physical properties. It is therefore useful to have a theoretical apparatus for the description of surface structures and a basic understanding of processes that create them. Surface roughness, characteristic length and other statistical quantities derived from the height distributions and autocorrelation functions are used to describe surface properties. However, since many disordered surfaces of scientific interest possess self-affinity — statistically similar features appearing on a wide range of scales — the values of these quantities depend on the scale of observation. Therefore the properties of such systems are described not as much by the values of the quantities themselves, but, rather, by their relation to the observation scale — the scaling properties. According to their scaling behavior, many physical systems can be classified into a small number of universality classes that describe common properties arising in very different models.

Modeling plays an important role in surface investigations. Simplified models that reproduce surfaces with features equivalent to those observed experimentally allow a better understanding of the actual surface forming processes. However, most of the models that accurately describe disordered surface formation cannot be solved analytically and one has to resort to numerical simulations.

This work focuses on one successful example of such models based on the generalized Kuramoto-Sivashinsky (gKS) equation. Equations of this type reproduce, quite accurately, the experimental results in amorphous thin film growth and, moreover, their terms can be convincingly related to the physical processes taking place at the surface. In the rescaled dimensionless form, the gKS equation depends on a single parameter whose value determines the evolution of the surface: from kinetic roughening leading to the saturation and stationary chaotic dynamics at small parameter values to the nonstationary coarsening behavior when the parameter values are large.

The dynamical behavior and scaling properties of gKS have not, as of yet, been sufficiently investigated. Even the scaling properties of the much more researched Kuramoto-Sivashinsky equation (KS), a special case of the gKS model considered here, have caused controversy. Many of the difficulties arising when attempting to look for the universal properties are due to the fact that these equations produce a band of exponentially growing modes selected by the linear part of the equation. This linear instability which is not present in the paradigmatic models of the universality classes, interacting with the nonlinear terms, produces patterns of definite characteristic size on top of the scale-free height variations obscuring the universal properties of the latter. Thus, the resulting scaling properties strongly depend on the parameter value even for the largest system sizes considered, even though the renormalization group arguments suggest that this dependence should not come about on the large scales.

This work systematically investigates the patterns, the scaling properties and the dynamics of surfaces evolving according to gKS by analysing both the surface morphologies and the kinetics of the global surface roughness in order to extract the scaling properties in finite size systems. While these properties might not be universal in the sense that they would, perhaps, differ from those expected in the infinite size systems, the results presented here are still valid and, hopefully, make a useful contribution to the understanding of surface formation in this finite-size world.

1 Introduction

A detailed understanding of surface growth physics has fueled several advances in science and technology, including more accurate dating in archeology [1], better integrated circuit technology [2], as well as production of novel materials [3]. In many cases of scientific and technological interest, the evolution of growing surfaces can be described by so-called *continuum models* that consist of nonlinear partial differential equations and often display rich and interesting dynamics [4]. Even though not all of this dynamics is currently accessible experimentally, it still is worthwhile to investigate, especially in the view of rapid experimental [5] and theoretical [6] progress.

The object of this study is a continuum surface growth model described by the two-dimensional *generalized* Kuramoto-Sivashisky equation with a single independent parameter α,

$$\partial_t h = -\nabla^2 h - \nabla^4 h - \alpha \nabla^2 (\nabla h)^2 + (\nabla h)^2 \,, \tag{1}$$

considered in [7], that produces chaotically evolving disordered spatial patterns. Equations of this type (with and without added noise) have been successfully used as models for amorphous solid surface growth [8–10] and nano-scale pattern formation induced by ion beam sputtering (IBS) [11–15].

Eq. (1) in two spatial dimensions describes the evolution of a (2+1)-dimensional interface, i.e., a surface whose height $h(\boldsymbol{r}, t)$ is defined as a function on a two-dimensional plane $\boldsymbol{r} \in \mathbb{R}^2$ that is growing in the direction h perpendicular to that plane as time t goes by. Numerical studies of Eq. (1) in one dimension have also been performed by Muñoz-Garcia et. al. [16], and a good correspondence to the IBS experiments has been found [17].

Eq. (1) has the celebrated Kuramoto-Sivashinsky (KS) equation [18–21]as its special case when parameter $\alpha = 0$:

$$\partial_t h = -\nabla^2 h - \nabla^4 h + (\nabla h)^2 \,. \tag{2}$$

The latter equation stands as a paradigmatic model for chaotic spatially extended systems and has been used to study the connections between chaotic dynamics at small scales and apparent stochastic behaviour at large scales [22–24].

Various generalizations and modifications of the KS equation (2) with local and non-local damping terms, anisotropy, and noise have been used to study pattern formation due to ion-beam erosion [25–30]. Eq. (2) itself in one- and two-dimensional cases has been a subject of active research for about three decades, and its scaling properties have even been an object of controversy.

It has been suggested by Yakhot [31] and subsequently confirmed and reiterated by different authors (see e.g., [22, 23, 32]) that the large-scale behaviour of the deterministic KS equation (2) in the one-dimensional case can be described by a stochastic equation

$$\partial_t h = \nabla^2 h + (\nabla h)^2 + \eta \tag{3}$$

where η represents random uncorrelated Gaussian noise.

Equation (3) has become known as the Kardar-Parisi-Zhang (KPZ) equation [33]. It was originally proposed as a continuum model for surface growth due to ballistic deposition [34], since it showed the same large-scale dynamic scaling behaviour [35]. [1]

However, the correspondence between KS and KPZ in two-dimensions has led to disagreements by the same authors [23, 32, 41, 42], because of the lack of conclusive analytical results. More recent results [24, 43] tend to support the conjecture that KPZ and KS equations belong to the same universality class, although the numerical results for the deterministic (noiseless) KS are not conclusive due to the extremely long transient effects. Recent numerical results for the two-dimensional KS [7] with much longer simulation times show the same scaling properties of the saturated surface roughness as obtained by Manneville and Chaté [44] where the Edwards-Wilkinson (EW) [45] type of behaviour is observed. The EW regime is the pre-asymptotic (in terms of system size) behaviour, and is expected to cross over to the KPZ scaling at much larger system sizes [46], thus, further supporting the argument that the two-dimensional KS and KPZ equations, in the large size limit, belong to the same universality class. However, [7] has reported a finite-size scaling behaviour that is different from

[1] Correspondence of large-scale properties in models that are very different in their microscopic details is quite common in the field of complex systems. One of the most successful examples of such a correspondence are the so-called *lattice gas models*. Such discrete, cellular-automaton-type models are capable of reproducing fluid dynamics described by Navier-Stokes equations [36–39]. An article on this topic [40] has been published by the author of this dissertation.

both the EW and the KPZ scaling in the less researched generalized KS case (1) with $\alpha > 0$.

1.1 Objective of the dissertation

This work attempts to “scratch the surface" of the wast discipline of disordered surface growth by presenting author’s research on one particular less-investigated model from this field.

One of the main purposes of this work is to introduce the reader to the continuum model for amorphous solid surface growth that is able to reproduce experimentally observed surface structures. The model is expressed in a nonlinear partial differential equation that contains the widely known and much researched Kuramoto-Sivashinsky equation as its special case. Even this — simpler — continuum model has caused some controversy concerning its scaling properties in the two-dimensional case. A systematic investigation of those properties in the much less researched equation presented in this thesis — another purpose of this thesis — thus, seems interesting and timely.

The goal is to demonstrate, in a wider parameter range, the validity of the scaling relations for the surface roughness reported in the previous work by the author [7], and to present the recent investigation of dynamics of the scale-free low-wavenumber spatial variations that these relations imply [47].

1.2 Scientific novelty

The scaling properties, although quite thoroughly investigated in similar equations, are relatively little researched in the case presented in this thesis. The investigation of the finite-size scaling and analysis of surface dynamics by analyzing the time series of the global surface roughness presented in the publications by the author [7, 47] have not been previously done for this particular model. Also, the simulations of unprecedented length with higher parameter values reveal, in addition to the previously reported global coarsening of the surface patterns, the occurrence of local coarsening behavior that has not been reported in the literature.

1.3 Scientific statements

The research conducted by the author allows to make the following statements supported by the results presented in this thesis:

1. The continuum model for amorphous solid thin film growth expressed by the generalized Kuramoto-Sivashinsky equation (gKS) on small scales produces cellular patterns that possess a characteristic length and, simultaneously, generates long-range height variations of self-affine character.

2. The gKS equation in its dimensionless form has a single independent parameter that determines the structure and dynamics of the surfaces evolving according to this equation. The parameter obtained for the surface growth model has to be non-negative, and there are two limiting cases for the gKS:

   (a) Kuramoto-Sivashinsky (KS) equation is obtained producing stationary spatio-temporal chaos when the parameter is zero, and

   (b) Conserved Kuramoto-Sivashinsky (cKS) equation producing a mound-like pattern coarsening in a non-stationary way is obtained by different rescaling as the parameter value goes to infinity.

   The dynamics for finite parameter values lies in between these limiting cases, as specified in further statements.

3. The KS — a special case of the gKS — demonstrates the finite-size scaling of the same type that is expected for the KPZ equation in the pre-asymptotic regime, suggesting that KS equation belongs to the KPZ universality class.

4. The gKS in the range of small positive parameter values produces stationary dynamics in the saturated regime, but with scaling properties that are different from those of the KS (and the KPZ) equation and vary with parameter value in the range of system sizes considered.

5. Small-scale patterns are also influenced by the equation parameter: the saturated pattern becomes coarser when the parameter value is increased, but the shape of mounds remains similar on average, as can be shown by

a simple geometrical argument. Therefore, the same argument allows for indirect, but many times faster estimation of the characteristic length in the cellular surface pattern.

6. The time series analysis of the global roughness for varying system sizes produces relations between the dynamical time scales of the long range height variations and the spatial scales. The resulting relations are power laws whose exponents are equivalent to the dynamic exponents of the model. They are found to decrease with increasing parameter value.

7. Further increase in parameter value results in non-stationary evolution of surfaces. The observed non-stationary behavior coincides with the occurrence of local coarsening structures that eventually become much higher than the rest of the surface.

1.4 Outline of the dissertation

The model for amorphous thin film growth expressed in the generalized two-dimensional isotropic Kuramoto-Sivashinsky equation (gKS) with a stochastic term is introduced in Sect. 2. The form of the model equation is first derived using the underlying symmetries and low-order expansion (Subsect. 2.1). Then, in Subsect. 2.2, the terms in the resulting model equation are related to the physical processes taking place during the surface growth, thus, also determining the signs of the coefficients before at each term. Subsect. 2.3 presents the numerical schemes used for computer simulations presented in this thesis.

Sect. 3 considers the deterministic version of the gKS. In Subsect. 3.1, it is demonstrated how the equation can be brought into dimensionless form with a single independent parameter. In the proposed scaling, the parameter value zero results in the famous Kuramoto-Sivashinsky (KS) equation that produces stationary spatio-temporal chaos. It is also shown how, in a different rescaling, the limit of the same parameter going to infinity results in another equation (cKS) that produces non-stationary coarsening of the surface profile. Subsects. 3.2 and 3.3 then discuss the behavior of gKS that is in between the above mentioned KS and cKS limits that results, after some initial transient period, in a stationary regime with surface patterns of different coarseness.

Next, Sect. 4 presents, in some detail, the measures for the characterization of disordered surface patterns, such as: the height distribution (Subsect. 4.1), height autocorrelation function and surface spatial spectrum (Subsect. 4.2). These are then calculated for surfaces resulting from numerical simulations of gKS (Subsect. 4.3) showing how the parameter value influences both, the small scale cellular patterns and the long-range height variations. The latter are shown to become more distinct in larger systems while the small scale patterns remain virtually unchanged. Subsect. 4.4 then shows how the assumption of the power-law behavior of the surface spectrum, at small-wavenumbers may give rise to the certain finite-size scaling relations for the global surface roughness and demonstrates a remarkable agreement between these relations and the numerical results obtained from gKS.

Sect. 5 investigates the small-scale cellular patterns where the individual surface elements (cells) appear as round humps of similar size giving a charac-

teristic length for the patterns. This length can be estimated from the position of the peak in the surface spectrum defined in the previous section, as explained in Subsect. 5.1. The characteristic length is obviously related to the surface roughness and the surface area. Subsect. 5.2 explores this connection. By making an ansatz relating the size, height and surface area of a single surface element, the scaling relation for a pattern of statistically similar elements is derived. This scaling relation is then compared to the corresponding numerical results produced by the gKS in a wide parameter range and a good agreement with the theoretical considerations is demonstrated indicating that the disordered surface patterns of different coarseness are, nevertheless, geometrically similar on average.

Sect. 6 and Sect. 7 focus on the dynamics of the surface evolution in the stationary regime. By analyzing the time series of the global surface roughness, the slowest time scales are estimated for the systems of different sizes. These time scales are related to the large-scale spatial variations and are found to increase with the system size as a power law. Since the exponent in this power law relates the spatial scales with the time scales, it must be connected to the dynamic exponent of the system.

The non-stationary dynamics that sets in for larger parameter values in the gKS model is considered in Sect. 8. The non-stationary regime sets in when the coarsening starts locally at some place on the surface. This results in a formation of a mound-like structure that peaks above the rest of the surface and exhibits peculiar pentagonal symmetry in its center while being surrounded by disordered smaller humps. The fast increase (by several times) of the global roughness caused by this local growth times is shown to have almost no effect on the surface area. Some arguments are presented, supporting the notion that this previously ureported effect is not merely an artifact of the numerical scheme.

Finally, Sect. 9 summarizes the results presented in this work and draws some conclusions.

2 A continuum model for amorphous solid thin film growth

Experimentally grown or eroded amorphous surfaces tend to exhibit pattern formation on the coarse-grained mesoscopic scale — the nanoscale [48–50]. In order to investigate such structures, one does not necessarily need to look at the complicated interatomic interactions between the depositing particles and the surface atoms. In many important cases coarse-grained continuum models describe the roughening and smoothing mechanisms at the surface which lead to the formation of mesoscopic — regular or irregular — patterns [51]. The surface in these models is described by a continuous function called *the surface morphology* $H(\boldsymbol{r}, t)$ — the height of the surface above the point $\boldsymbol{r} = (x, y)$ on the (in the simplest case) flat substrate at time t (see Fig. 1, left). The evolution of the surface can then be described by a partial differential equation (PDE).

The goal of this section is to present the derivation of a *minimal continuum model for the spatio-temporal evolution of the surface morphology* which contains all dominant relaxation mechanisms, and to compare some characteristic statistical measures (surface roughness, correlation length) for surfaces resulting from numerical simulations of this model to the results from experiments with ZrAlCu thin films [8, 48, 49]. The most of what is presented in this section is based on the works by Raible et. al. [8–10, 52, 53].

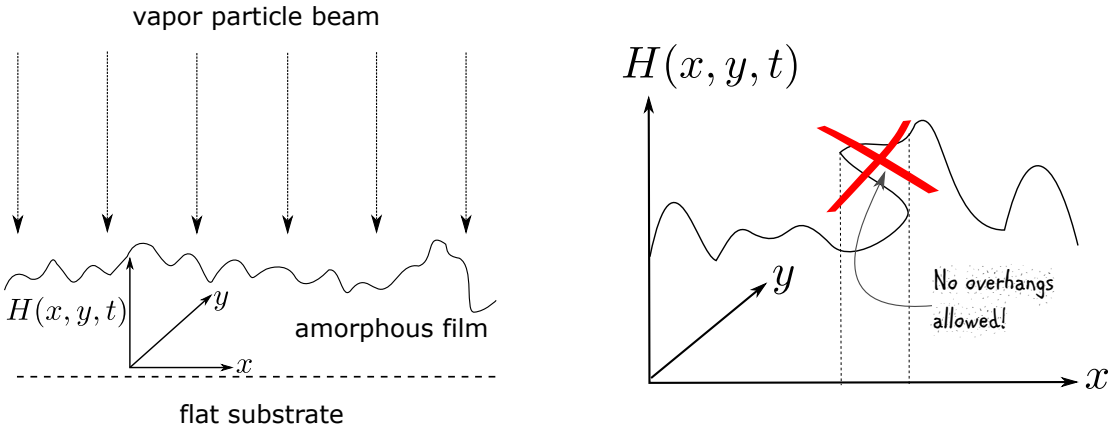

Figure 1: Left panel: schematic experimental setup of the amorphous thin film growth by particle deposition. Right panel: schematic example of an overhang that is not permitted by a 2D continuum growth model described by a PDE.

2.1 Physical symmetries

Here we begin our theoretical description of amorphous surface growth. We focus on the growth of solid, *amorphous* thin films, generated by vapor deposition. There are no long-range ordering phenomena are present and therefore the characteristics of the growing film should be spatially isotropic. The formation of disordered mound-like or cellular patterns observed in amorphous film growth experiments [48,49,54–56], however, suggests some underlying ordering mechanism that must stem from the interplay between roughening and relaxation phenomena taking place on the growing surface.

The system is schematically shown in Figure 1. The growth process starts from an initially flat substrate. The beam of incoming particles is directed perpendicular to the substrate. It is assumed to be *low-energetic*, so that no kick-off or desorption of the already deposited particles is possible, and almost constant in space and time — with only weak superimposed fluctuations. The growing layer built up by deposited particles forms a spatio-temporally evolving free surface that could be described at any time t by the surface morphology $H(\boldsymbol{r}, t)$, i.e. the height of the surface above the flat substrate where $\boldsymbol{r} = (x, y)$ is the point on the substrate. Therefore, the model can be called a $(2+1)$-dimensional system (a two-dimensional surface growing in the third dimension), following the notation that is common in theoretical description and modeling of surface growth [51,57,58].

A model equation for amorphous solid surface growth described above must include the height changes due to the deposition and relaxation (surface diffusion) of just deposited particles before finally sticking and becoming a part the solid surface. A well-established phenomenological approach suggests an underlying partial differential equation of first order in time. The most general ansatz for such an equation is

$$\partial_t H(\boldsymbol{r}, t) = G[H, \{\nabla^k H\}, \boldsymbol{r}, t] + I(\boldsymbol{r}, t). \tag{4}$$

Here, $G[H, \{\nabla^k H\}, \boldsymbol{r}, t]$ is a functional that contains all physical mechanisms leading to growth, relaxation and pattern formation processes taking place on the surface. For simplicity, it is assumed that all these mechanisms are *local*. Thus, the functional G can not contain any non-local contributions such as in-

tegration over space or time, time delay or instantaneous interactions over distance. In this case G can still include the surface height H and all its spatial derivatives $\{\nabla^k H\}$ in various combinations. It can also explicitly depend on the position $\boldsymbol{r}$ and time t. $I(\boldsymbol{r}, t)$ represents the flux of depositing particles, which also depends on the position and time.

Assuming some underlying *symmetries* in description of the growth process puts further constraints in the form of the functional G in (4). We assume the following symmetries:

- Stationarity (homogeneity of time). For a steady process in a constant environment, there is no dependence on the specific choice of the origin of time — invariance against translations in time. Thus G can not depend on t.

- Homogeneity of space. The physical processes on the surface should not depend on the specific choice of the origin of the coordinate system on the substrate — invariance against translations parallel to the substrate (perpendicular to the growth direction). Thus no dependence of G on $\boldsymbol{r}$ is allowed.

- Invariance under translations in growth direction, which implies that no dependence on the specific choice of the origin of H is possible. Together with the assumption of a low-energetic beam of depositing particles, this leads to independence of G on H. [2]

Therefore, under the symmetries given above the functional G can only depend on the various combinations of spatial derivatives of H:

$$G[H, \{\nabla^k H\}, \boldsymbol{r}, t] \longrightarrow G[\{\nabla^k H\}] \,.$$

[2] Note that this symmetry does not completely exclude the dependence of G on H, but rather the dependence on the average surface height $\bar{H} = \langle H \rangle_{\boldsymbol{r}}$. This leaves the possibility that G could still depend on the height, relative to the average surface height $h = H - \bar{H}$, if no further assumptions are made. The dependence on h would allow the so-called damping terms [25, 59] that might cause the appearance of hexagonal patterns. These damping terms correspond to the desorption or kick-off of the deposited particles from the surface and are equivalent to the redeposition terms in surface erosion models [28, 59–61], where the effect is that some of the eroded particles land back on the surface, i.e. are redeposited. The nonlocality of the term h can be disposed of by mapping it on the local equation by a simple transformation, as shown in [60]. However, in the model considered here, it is assumed that the particle beam is low-energetic, so that kick-off of the surface particles is negligible.

In the model considered here the deposition flux $I(\boldsymbol{r},t)$ is assumed to be basically constant F, with some small fluctuations, and these fluctuations do not have any noticeable effect on the relaxation processes described by G: they only result in some small, additive spatio-temporal noise $\eta(\boldsymbol{r},t)$ in the deposition flux $I(\boldsymbol{r},t)$,

$$I(\boldsymbol{r},t) = F + \eta(\boldsymbol{r},t)\,, \tag{5}$$

where $F \equiv \langle I \rangle$ is a constant (in space and time) mean deposition flux and η is assumed to be Gaussian (normally distributed) white (totally uncorrelated) noise

$$\langle \eta(\boldsymbol{r},t)\eta(\boldsymbol{r}',t')\rangle_\eta = 2D\delta^2(\boldsymbol{r}-\boldsymbol{r}')\delta(t-t') \tag{6}$$

with zero mean

$$\langle \eta(\boldsymbol{r},t)\rangle_\eta = 0\,, \quad \forall \boldsymbol{r},t\,.^3 \tag{7}$$

Here $\langle\cdots\rangle_\eta$ denotes ensemble average, and D is the fluctuation strength (in the sense that $2Dt$ is the variance a half of the mean square fluctuation produced by the noise in time t per unit area). Since the mean deposition flux is constant, it is useful to introduce the *profile* of the surface morphology, $h(\boldsymbol{r},t) = H(\boldsymbol{r},t) - Ft$, which is the surface morphology $H(\boldsymbol{r},t)$ transformed into frame of reference which is co-moving with the mean deposition flux[4] (moving along the H axis with a constant speed F). This transformation has no effect on the spatial derivatives of the height ($\nabla^k h = \nabla^k H,\ \forall k \geq 1$), thus, the equation for the surface profile $h(\boldsymbol{r},t)$ is simply

$$\partial_t h(\boldsymbol{r},t) = G[\{\nabla^k h\}] + \eta(\boldsymbol{r},t). \tag{8}$$

Amorphous surface growth with set up in such a way that the incoming particle beam is perpendicular to the substrate (as schematically shown in Fig. 1) implies one more symmetry for G:

- *Isotropy* of the growth process — invariance under rotations and reflections in the plane, perpendicular to the growth direction. Thus, there can be only scalar combinations of spatial derivatives of h in G, for example:

[3] also $\langle \eta(\boldsymbol{r},t)\rangle_{\boldsymbol{r}} = 0\,,\ \forall t$ and $\langle \eta(\boldsymbol{r},t)\rangle_t = 0\,,\ \forall \boldsymbol{r}$.

[4] If no density inhomogeneities occur in the growing surface, then $Ft = \langle H(\boldsymbol{r},t)\rangle_{\boldsymbol{r}}$ which means that the average surface height grows at the constant rate with the mean deposition flux F, and $\bar{h} = \langle h(\boldsymbol{r},t)\rangle_{\boldsymbol{r}}$ is a conserved quantity [52].

- even derivatives of h: $\nabla^k h$, where $k = 2, 4, 6, \ldots$
- odd derivatives multiplied in couples by scalar multiplication: $(\nabla^m h) \cdot (\nabla^n h)$, with $m, n = 1, 3, 5, \ldots$
- even derivatives of the latter: $\nabla^k (\nabla^n h)^2$.
- or terms like this: $\nabla^m \cdot ((\nabla^n h)(\nabla^k h))$.

For a *minimal* model of the surface evolution G is expanded in a series where of all terms allowed by the above mentioned symmetries only those terms which are linear or quadratic in h and only posses a maximum of fourth order spatial derivatives are kept. These terms are: $\nabla^2 h$, $(\nabla h)^2$, $\nabla^4 h$, $\nabla^2 (\nabla h)^2$, $(\nabla^2 h)^2$ and $\nabla \cdot [(\nabla h)(\nabla^2 h)]$. The latter term can be expanded:

$$\nabla \cdot [(\nabla h)(\nabla^2 h)] = \frac{1}{2} \nabla^2 (\nabla h)^2 + 2M \,,$$

where

$$M = \det \begin{pmatrix} \partial_x^2 h & \partial_y \partial_x h \\ \partial_x \partial_y h & \partial_y^2 h \end{pmatrix} . \tag{9}$$

Finally, after all of the above considerations, the general form (4) becomes *minimal model equation* which reads:

$$\partial_t h = a_1 \nabla^2 h + a_2 \nabla^4 h + a_3 \nabla^2 (\nabla h)^2 + a_4 (\nabla h)^2 + a_5 (\nabla^2 h)^2 + a_6 M + \eta \,. \tag{10}$$

The evaluation of the coefficients and further simplifications of this model can be made by considering the underlying processes governing the surface growth.

2.2 Underlying physical processes

The derivation of the model equation (10) from the underlying symmetries and assumptions, as presented in the previous subsection, does not give any information yet about the size or even a sign of the coefficients a_i, $i = 1, \ldots, 6$. Also no insight in to the physics of the growth process has yet been provided in the previous argument. Thus, in this subsection, a possible interpretation of the terms in the model equation is proposed, in which each term corresponds to some physical process that can take place on the surface. The deposited particles

interact with the surface atoms and each other. They therefore experience various steering processes due to interatomic interactions and relaxation processes (surface diffusion) before they stick to the surface. As demonstrated in [9], the density inhomogeneities in the growing surface should also be taken into account, that is, the possibility that newly arriving particles stack up with different densities, depending on the height gradients and curvatures of the already formed surface.

There are four most important competing microscopic mechanisms which lead to smoothing, roughening and pattern formation on the surface:

- Surface tension
- Concentration equilibration of deposited particles
- Steering of arriving particles
- Inhomogenous density distribution

This subsection discusses discusses the processes listed above in more detail relating them to the terms in the model equation (10) that has been obtained in the previous subsection using only some basic assumptions and symmetry arguments.

Interaction with the surface atoms

The terms in the model equation (10) proportional to a_1 and a_6 are found to be responsible for the surface roughening and can be related to the microscopic processes of deflection of the arriving particles [53, 62] and not, as previously suggested, to the finite size of particles being deposited, [63]. The basic idea is that the incoming particles experience a deflection close to the surface due to the attractive interatomic interaction with the already condensed surface atoms. The arriving particles do not hit the surface perpendicular to the substrate (in the growth direction), but rather perpendicular to the surface itself as schematically shown in Fig. 2. This results in the effect that more particles arrive at the positions with negative surface curvature $-\nabla^2 h < 0$ (peaks) than at the positions with a positive curvature $-\nabla^2 h > 0$ (valleys). This, in turn, produces a growth instability which causes surface roughening, since the peaks

tend to grow faster and the valleys slower than the average deposition rate F (see right panel of Fig. 2).

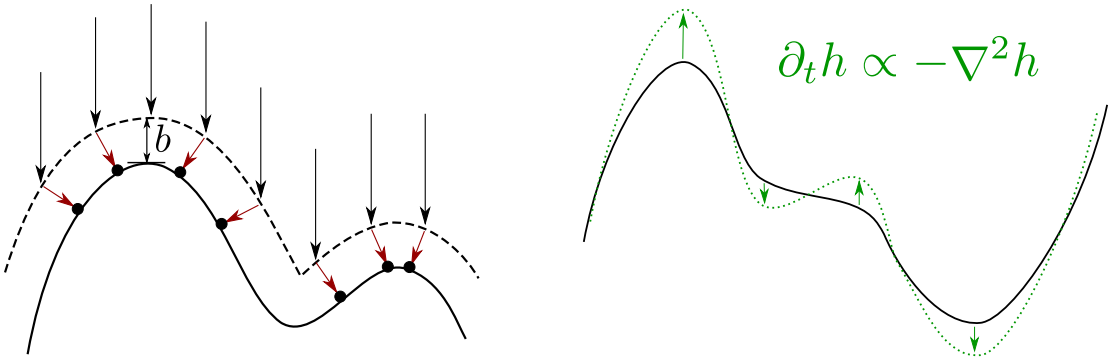

Figure 2: A schematic representation of the deflection of the arriving particles due to the attractive interaction with the surface atoms (left panel) and the effects of this process on the surface profile (right panel).

The effect of the particle deflection described above can be demonstrated mathematically when suitable simplifications are applied. An idealization used in [53] assumes that the arriving particles undergo the change in direction mentioned above instantaneously when they reach a critical distance b (left panel of Fig. 2), the effective range of interaction, from the surface.

The unit vector perpendicular to the surface $h(\boldsymbol{r},t)$ can be expressed as

$$\boldsymbol{n}(\boldsymbol{r},t) = \frac{1}{\sqrt{1+(\nabla h)^2}} \begin{pmatrix} -\nabla h \\ 1 \end{pmatrix} \tag{11}$$

where $\nabla h \equiv \hat{\boldsymbol{x}}\partial_x h + \hat{\boldsymbol{y}}\partial_y h$ is the gradient of the surface height h on the flat substrate — the (x,y)-plane. Then, the coordinates[5] of a point $\boldsymbol{R'} = (x',y',h')$ on an imaginary surface located a distance b in the $\boldsymbol{n}$-direction from point $\boldsymbol{R} = (x,y,z)$ on the real surface can be expressed as

$$\boldsymbol{R'} = \boldsymbol{R} + b\,\boldsymbol{n}\,, \tag{12}$$

that is, using (11),

$$\begin{aligned} x' &= x - \tfrac{b}{\sqrt{1+(\nabla h)^2}}\partial_x h\,, \\ y' &= y - \tfrac{b}{\sqrt{1+(\nabla h)^2}}\partial_y h\,, \\ h' &= h + \tfrac{b}{\sqrt{1+(\nabla h)^2}}\,. \end{aligned} \tag{13}$$

[5]Now meaning the coordinates in tree-dimensional space $\big(x,y,h(x,y)\big)$.

Now, the amount of incoming particles deposited on the surface above an infinitesimal area $\mathrm{d}S = \mathrm{d}x\mathrm{d}y$ on the substrate is actually the amount of particles passing through the area $\mathrm{d}S' = \mathrm{d}x'\mathrm{d}y'$. Therefore, the local deposition flux is equal to the mean particle flux F multiplied by the factor $\mathrm{det}A$, since $\mathrm{d}S' = \mathrm{det}A\ \mathrm{d}S$, where A is the transformation matrix

$$\begin{pmatrix} dx' \\ dy' \end{pmatrix} = A \begin{pmatrix} dx \\ dy \end{pmatrix} , \tag{14}$$

which, according to (13), is

$$A = \begin{pmatrix} \partial_x x' & \partial_y x' \\ \partial_x y' & \partial_y y' \end{pmatrix} = \begin{pmatrix} 1 - b\partial_x \frac{\partial_x h}{\sqrt{1+(\nabla h)^2}} & -b\partial_y \frac{\partial_x h}{\sqrt{1+(\nabla h)^2}} \\ -b\partial_x \frac{\partial_y h}{\sqrt{1+(\nabla h)^2}} & 1 - b\partial_y \frac{\partial_y h}{\sqrt{1+(\nabla h)^2}} \end{pmatrix} . \tag{15}$$

The continuum model equation describes the coarse-grained scales where the radii of the surface curvature are much larger than the effective reach of the interatomic interaction, and thus, $b|\nabla h| \ll 1$. Therefore, b can be considered a small parameter, and the terms proportional to b^2 can be omitted when calculating $\mathrm{det}A$. This leads to

$$\mathrm{det}A = 1 - b\nabla \cdot \left(\frac{\nabla h}{\sqrt{1 + (\nabla h)^2}} \right) . \tag{16}$$

By using the small gradient expansion,

$$\frac{1}{\sqrt{1 + (\nabla h)^2}} \approx 1 - \frac{1}{2}(\nabla h)^2 , \tag{17}$$

and taking only the lowest order terms, one ends up with the following transformation for the local deposition flux

$$F \longrightarrow F - Fb\,\nabla^2 h \tag{18}$$

which not only accounts for the term $\propto \nabla^2 h$ in the model equation (10), but also relates its coefficient a_1 to the physical quantities $F > 0$ and $b > 0$ showing that its sign must be negative:

$$a_1 = -Fb < 0 . \tag{19}$$

A more detailed derivation would show that this scenario of particle deflection due to interatomic interaction simultaneously gives rise to the two contributions in the model equation (10): $a_1\nabla^2 h$ and $a_6 M$ with M given by (9). Moreover , the coefficients a_1 and a_6 can be related to the mean deposition flux F and the effective range of interaction b yielding $a_1 = -Fb$ and $a_6 = Fb^2$. Since, as mentioned before, the size of b should typically be of the order of one atomic diameter and therefore much smaller than the curvature of the coarse-grained surface, the contribution of the term proportional to a_6 can be considered small in comparison to the contribution of a_1-term and can therefore be neglected leaving only the term $a_1\nabla^2 h$ (with $a_1 < 0$) to account for the surface roughening due to the deflection of incoming the particles. This term, if it was alone on the rhs of (10) would result in extreme roughening of the surface, which can be seen by substituting a single mode of wavenumber $\boldsymbol{k}$, $h(\boldsymbol{r}, t) = h_{\boldsymbol{k}}(t)\exp(\mathrm{i}\,\boldsymbol{k}\cdot\boldsymbol{r})$, into the linear equation $\partial_t h = -\nabla^2 h$. The result shows that the amplitude of any mode of wavenumber $\boldsymbol{k}$ would grow exponentially with the rate proportional to $|\boldsymbol{k}|^2$ and would result in the *ultraviolet catastrophe*. This, however, does not happen, because there are other processes in play, that manifest themselves by smoothing the surface.

Surface tension

A surface is an interface between two different media (two different materials or two different phases of the same material), and thus, the particles at the surface interact with either one or the other medium, depending on direction. This leads to asymmetric (anisotropic)of particles interactions with their surroundings (as opposed to the bulk particles) which lead to additional forces known as *surface tension*.

The effect of surface tension is present in many different surfaces. It acts to minimize the potential energy of the surface. In the case of two different materials, if there is a stronger attraction between the same kind of particles, the surface particles experience stronger attraction to the bulk of the same material relative to the bulk of the other material. Thus, their potential energy is lower, when they are surrounded more by the same material.

In the case of two phases of the same material (as in the surface growth model considered here), the particles are more attracted to the denser phase.

Therefore the surface particles have different potential energies depending on their positions relative to the bulk of the material — the potential energy is lower, when the particle is surrounded more densely by other particles.

The particles tend to minimize their potential energy and therefore try to move to the regions on the surface where they would have lower potential energies. In the case of surfaces between fluids (gases or liquids), this surface tension results in spherical or flat surfaces, when a homogeneous field (e.g. gravity) is present.

However in the case of solid growing surfaces, the particles are able to move only for a limited time — before they finally stick to the bulk of material, so that only recently deposited particles may participate in surface restructuring. This results in the so-called *surface diffusion* [64] which acts as a kind of surface tension [52]. The strength of the effect of surface tension then depends on the *diffusion length* of the particles (the mean distance a deposited particle is able to move until it sticks to the surface).

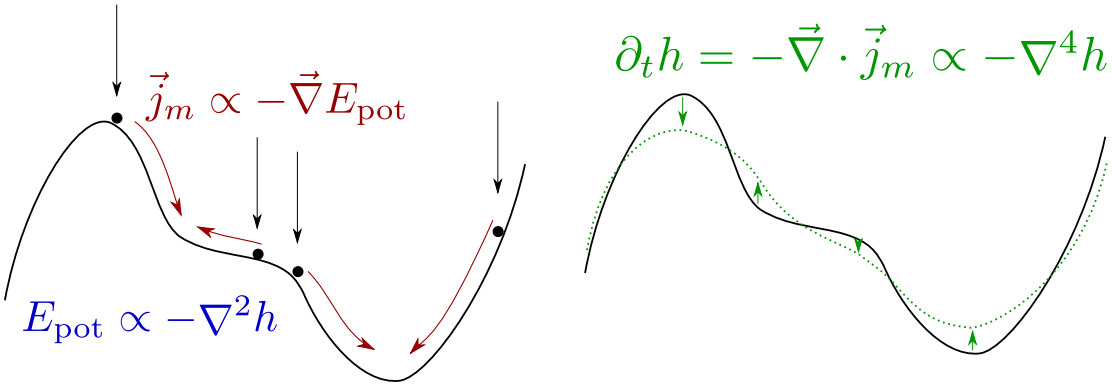

Figure 3: A schematic representation of surface diffusion of deposited particles (left panel) resulting in the effect of to the surface tension which smooths the surface (right panel).

In the model equation (10) the above described surface diffusion is accounted for by the term proportional to a_2. As already mentioned, the deposited particles tend to move to the regions of lower potential energy (higher binding energy) before they stick. These are the regions with positive surface curvature $\nabla^2 h > 0$ (valleys). Thus, the potential energy of the particle at the surface is assumed to be proportional to the negative surface curvature $E_{pot} \propto -(\nabla^2 h)$. The diffusion current is proportional to the negative gradient of the potential energy $\boldsymbol{j}_m \propto -\nabla E_{pot} \propto \nabla(\nabla^2 h)$, so that, depending on the local curvature, the

current can be uphill or downhill (Fig. 3). Analogously to the continuity equation, this diffusion current contributes to the rate of change of surface height $\partial_t h$ as $-\nabla \cdot \boldsymbol{j}_m \propto -\nabla^4 h$. The coefficient a_2 in (10) must therefore be negative in order to give the correct sign for the term $a_2 \nabla^4 h$, so it would be able to account for the effect of surface diffusion described above. This term basically tries to minimize the area of the surface and, as a consequence, to smooth the surface morphology as illustrated in the right panel of Fig. 3.

The smoothing of the surface due to the term $-\nabla^4 h$ can be demonstrated by, again, looking at how the amplitude $h_{\boldsymbol{k}}(t)$ a single mode of wavenumber $\boldsymbol{k}$, $h(\boldsymbol{r}, t) = h_{\boldsymbol{k}}(t) \exp(\mathrm{i}\, \boldsymbol{k} \cdot \boldsymbol{r})$ changes according to the linear equation $\partial_t h = -\nabla^4 h$. The result shows that the amplitude of any mode of wavenumber $\boldsymbol{k}$ would decay exponentially with the rate proportional to $|\boldsymbol{k}|^4$ and would result in the *flat surface* if the surface diffusion term $-\nabla^4 h$ acted alone.

Lienear instability

As has been demonstrated above, the linear terms $a_1 \nabla^2 h$ and $a_2 \nabla^4$ with $a_1 < 0$ and $a_2 < 0$ in (10) represent physical mechanisms that manifest in roughening and smoothing effects, respectively. It is easy to demonstrate that both of these terms acting together result in the growth instability where a finite band of spatial modes is amplified while the rest of the modes are decaying exponentially. The same reasoning also leads to conclusion that no other combination of the signs of the coefficients a_1 and a_2 would produce such an instability. The demonstration goes as follows.

Taking only the two linear terms on the rhs of (10) produces the linear equation

$$\partial_t h = a_1 \nabla^2 h + a_2 \nabla^4 h \tag{20}$$

which can be solved analytically with the surface profile $h(\boldsymbol{r}, t)$ expressed as the sum of its Fourier modes

$$h(\boldsymbol{r}, t) = \sum_{\boldsymbol{k}} h_{\boldsymbol{k}}(t) \exp(\mathrm{i}\, \boldsymbol{k} \cdot \boldsymbol{r})\,. \tag{21}$$

By substituting (21) into (20), one ends up with uncoupled equations for the

amplitude of each mode:

$$\dot{h}_{\boldsymbol{k}}(t) = (-a_1|\boldsymbol{k}|^2 + a_2|\boldsymbol{k}|^4)h_{\boldsymbol{k}}(t)\,. \tag{22}$$

These linear first order ODEs have simple exponential solutions

$$h_{\boldsymbol{k}}(t) = h_{\boldsymbol{k}}(0)\,\exp\big(\sigma(\boldsymbol{k})t\big) \tag{23}$$

with $\sigma(\boldsymbol{k}) = -a_1k^2 + a_2k^4$, $k \equiv |\boldsymbol{k}|$, that is, the amplitudes of the modes with the wave vectors $\boldsymbol{k}$ for which $\sigma(\boldsymbol{k}) > 0$ will be exponentially amplified, whereas the modes whose $\boldsymbol{k}$ is such that $\sigma(\boldsymbol{k}) < 0$ will decay exponentially. It is clear that for only the case where both $a_1 < 0$ and $a_2 < 0$ will result in the finite band of wavenumbers k that are amplified. In this case (see Fig. 4), $0 < k < \sqrt{\frac{a_1}{a_2}}$ are amplified and the rest experience decay. After a short evolution time the mode of wavenumber $|\boldsymbol{k}| =: k_c$ that is amplified the strongest will start to dominate producing patterns of size $l_c = \frac{2\pi}{k_c}$. Obviously, k_c is the value at which $\sigma(k_c)$ has its maximum.

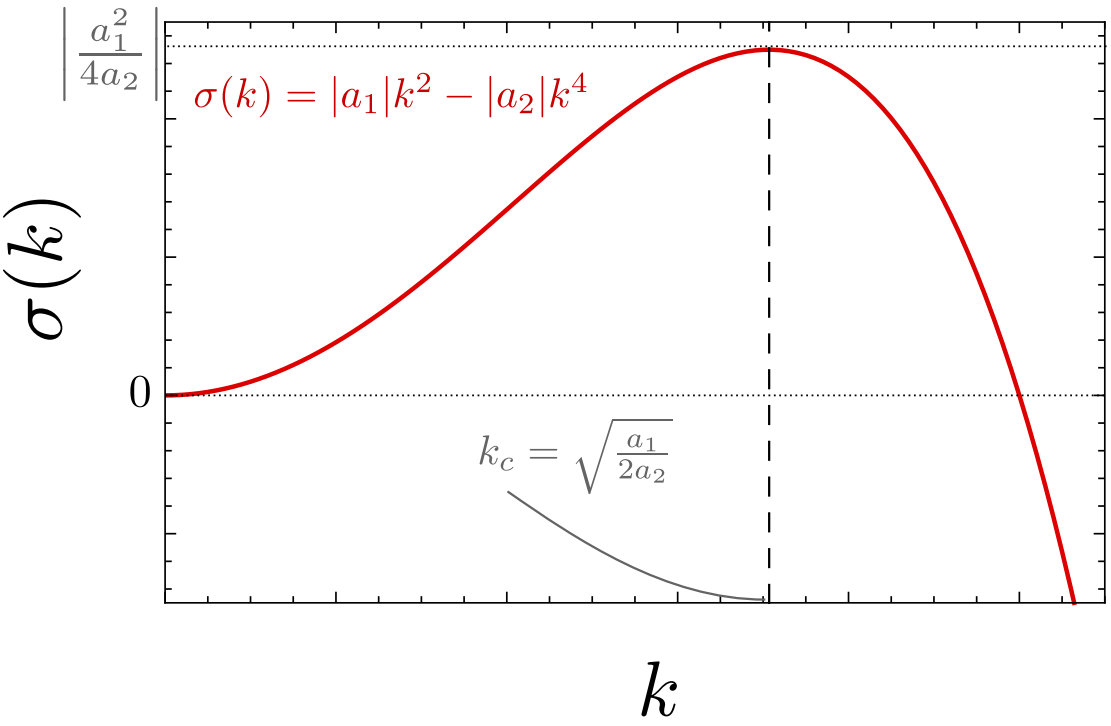

Figure 4: The instability caused by the linear terms of (10), $a_1\nabla^2 h$ and $a_2\nabla^4$, in the case where $a_1 < 0$ and $a_2 < 0$. The graph shows $\sigma(k)$ (thick red line) and the wavenumber k_c of the maximally amplified mode (vertical dashed line).

For an almost flat surface with only minor height variations, the linear

terms dominate the growth process described by (10). In this case, the band of modes whose wave numbers are $0 < k < \sqrt{\frac{a_1}{a_2}}$ grow exponentially. Since the modes with wavenumber $k_c = \sqrt{\frac{a_1}{2a_2}}$ are amplified the most, they begin to dominate the surface morphology creating structures of characteristic length $l_c = \frac{2\pi}{k_c}$ that increase exponentially in height. However, this exponential growth cannot last indefinitely. Once the amplitudes of the modes reach certain size, the nonlinear terms come into play by coupling the modes stopping the exponential increase of their amplitudes.

Concentration equilibration at the surface

The term proportional to a_3 in the model equation (10) can be related to the tendency for the inhomogeneous concentration of the arriving particles to strive towards equilibrium before settling down and sticking to the surface. The reason for the occurrence of these inhomogeneities can be explained in the purely geometrical way.

More particles per surface area arrive at the positions with a small or zero absolute value of the slope $|\nabla h|$ than at the positions which are strongly inclined with respect to the particle beam (see Fig. 5). The local concentration c of the particles arriving at some infinitesimal surface element is inversely proportional to its area divided by the area of its projection on the flat surface. Thus, the local concentration is $c \propto 1/\sqrt{1+(\nabla h)^2}$ or, in the small gradient expansion, $c \propto 1 - \frac{1}{2}(\nabla h)^2$.

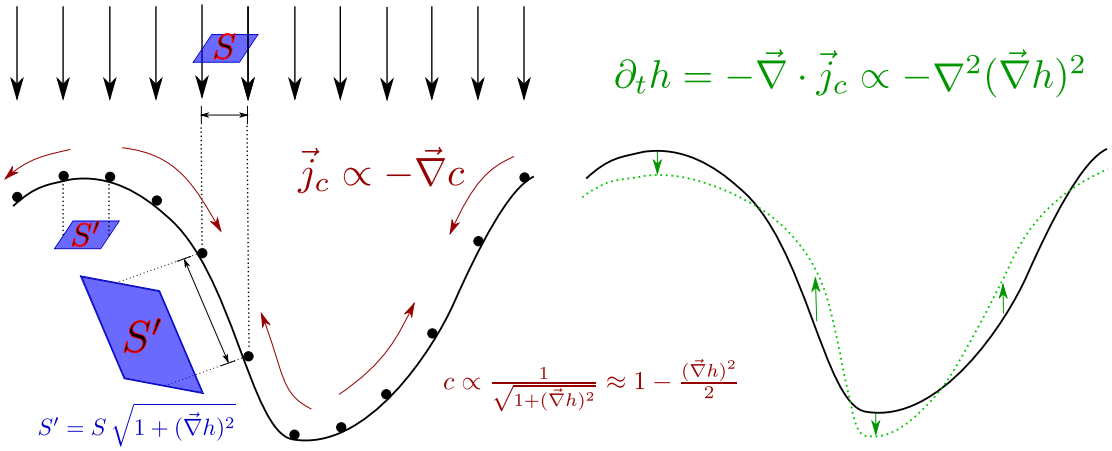

Figure 5: Surface diffusion of deposited particles due to the inhomogeneous concentration of deposited particles.

The inhomogeneous concentration causes the diffusion current $\boldsymbol{j}_c \propto -\nabla c \propto \nabla(\nabla h)^2$, which contributes to the height changes as $-\nabla \cdot \boldsymbol{j}_c \propto -\nabla^2(\nabla h)^2$. Thus, it follows that the contribution of the concentration equilibration can be accounted for by the term $a_3\nabla^2(\nabla h)^2 \equiv -\nabla \cdot \boldsymbol{j}_c$ with $a_3 < 0$. Fig. 5 provides a schematic illustration of this process and its contribution to the surface profile. Note that under the influence of this term (if the other terms are ignored) the valleys become deeper and sharper while the peaks become more blunt and round. In combination with the linear instability, this would produce the pattern of mounds growing in size. In fact, if one considers only the linear terms $a_1\nabla^2 h$ and $a_2\nabla^4$ considered above and the term $a_3\nabla^2(\nabla h)^2$ with $a_1, a_2, a_3 < 0$, the resulting equation

$$\partial_t h = a_1\nabla^2 h + a_2\nabla^4 h + a_3\nabla^2(\nabla h)^2 \tag{24}$$

would be of the form of the *conserved Kuramoto-Sivashinsky* (cKS) equation [52] which produces a coarsening pattern that only saturates when the diameter of the growing hills extends to the size of the whole system. Since the surface growth experiments exhibit saturation in the surface patterns [48, 49], further processes must be considered that produce the results consistent with these observations. Raible et. al. [9] have found that in order be able to reproduce the experimental results, density inhomogeneities in the growing surface must be considered.

Effects of density inhomogeneities

The terms in the model equation (10) that are proportional to a_4 and a_5, in contrast to those previously considered,*cannot* be transformed to represent a divergence of some current. These terms also cannot result from the particle desorption since it is assumed that the energy of the particles in the vapour is too low to cause such effects and therefore *all* arriving particles finally contribute to the surface growth.[6] As a consequence, these terms can only arise from changes of the coarse grained density. Assuming for a moment that the deposition noise is zero $\eta = 0$, particle conservation implies that the rate of change of the number of particles per substrate area above a given position on the substrate, $C(\boldsymbol{r}, t)$,

[6]This assumption is valid in most of the experimental setups for thin films at room- or lower temperatures

is determined by the balance equation

$$\partial_t C = -\nabla \cdot \boldsymbol{j}_C + \rho_0 F \tag{25}$$

The divergence of the current $\boldsymbol{j}_C$ is induced by the combination of all surface relaxation processes (the arguments mentioned before in this section), i.e. $-\nabla \cdot \boldsymbol{j}_C = \rho_0[a_1\nabla^2 H + a_2\nabla^4 H + a_3\nabla^2(\nabla H)^2 + a_6 M]$, where ρ_0 is the constant particle density. Allowing for density variations at the growing surface, the rate of change of C is related to the change of height H by $\partial_t C = \rho(\{\nabla^k H\})\partial_t H$. Here $\rho(\{\nabla^k H\})$ denotes the density at the surface which can depend in the derivatives of the height $\{\nabla^k H\}$. If the density variations are not allowed ($\rho = \rho_0 = \mathrm{const}$), there is a direct proportionality between C and H and therefore $\partial_t C = \rho_0 \partial_t H$. If small density variations are taken into account, $\rho(\{\nabla^k H\})$ can be expanded in the derivatives of H[7] yielding $\rho(\{\nabla^k H\}) = \rho_0[1 + q_1(\nabla H)^2 + q_2\nabla^2 H]$ in the lowest order approximation. Therefore

$$\partial_t H = \rho^{-1}(\{\nabla^k H\})\partial_t C \tag{26}$$

holds with the inverse of the density (again, in the lowest order approximation)

$$\rho^{-1}(\{\nabla^k H\}) = \rho_0^{-1}[1 - q_1(\nabla H)^2 - q_2\nabla^2 H] \tag{27}$$

By putting (25) into (26) with (27) one finally gets

$$\partial_t H = a_1\nabla^2 H + a_2\nabla^4 H + a_3\nabla^2(\nabla H)^2 \underbrace{-q_1 F(\nabla H)^2}_{=:a_4(\nabla H)^2} \underbrace{-q_2 a_1(\nabla^2 H)^2}_{=:a_5(\nabla^2 H)^2} + a_6 M + F \tag{28}$$

Thus, it is shown that the terms proportional to a_4 and a_5 in the model equation (10) can indeed arise from density inhomogeneities.

From the physical point of view , however, the density changes are primarily connected to the gradients of the surface profile reflecting the local arrangement of particles at the surface and not so much to the surface curvature. This implies that the a_5-term can be disregarded in the minimal model. Furthermore, since the density variations result from an increase of the mean interparticle

[7] The allowed derivatives in this expansion are given by the same argument from symmetry as was used in the previous subsection for the derivation of (10), because for the density the same symmetries must hold

distances at the surface positions with larger absolute values of height gradients $|\nabla H|$, one has to expect that the local particle density is decreased, which implies that $a_4 > 0$ holds.

Finally, after considering the above arguments (neglecting the terms proportional to a_5 and a_6, transforming into the moving frame of reference $h = H - Ft$ and adding the noise term), the *minimal model equation for the amorphous thin film growth* can be given by:

$$\partial_t h = a_1 \nabla^2 h + a_2 \nabla^4 h + a_3 \nabla^2 (\nabla h)^2 + a_4 (\nabla h)^2 + \eta \tag{29}$$

with $a_1, a_2, a_3 < 0$ and $a_4 > 0$. This is a nonlinear stochastic partial differential equation. Since such an equation cannot be solved analitically, it has to be investigated by numerical methods (computer simulations). The methods used for this thesis will be discussed in the next section.

The terms in the equation (29) proportional to a_1, a_2 and a_3 can be written as divergence of some current. Thus, the equation without a term proportional to a_4 would have a form of a continuity equation and would give a constant mean of the height profile h: $\langle h \rangle_{\boldsymbol{r}} = \text{const}$. This would correspond a linear increase of the mean height in time with a velocity F: $\langle H \rangle_{\boldsymbol{r}} = Ft + \text{const}$, the constant, of course, being zero for any initial condition with $\langle h \rangle_{\boldsymbol{r}} = 0$.[8] Only the term proportional to a_4 does not fit in the form of the continuity equation. It is also clear that the contribution of this term can only be positive (or equal to zero for a completely flat surface). Thus, the a_4-term causes the mean height $\langle H \rangle_{\boldsymbol{r}}$ grow with the velocity higher than the mean deposition rate F, that is $\langle \partial_t H \rangle_{\boldsymbol{r}} = F + \langle \partial_t h \rangle_{\boldsymbol{r}} = F + \langle a_4 (\nabla h)^2 \rangle_{\boldsymbol{r}} =: F + v_{ex}$, where $v_{ex} > 0$ is a so-called *excess velocity*.

After applying all of the above considerations to (10), one ends up with the equation

$$\partial_t h = a_1 \nabla^2 h + a_2 \nabla^4 h + + a_3 \nabla^2 (\nabla h)^2 + a_4 (\nabla h)^2 + \eta \tag{30}$$

where $a_1, a_2, a_3 < 0$ and $a_4 > 0$.

[8] It is, of course, for the boundary conditions that do not allow particles to leave the system, e.g. periodic boundary conditions

2.3 Numerical methods

This subsection introduces some of the numerical methods that have been used in the research presented in this work for computer simulations of the model equation (30). In [53], three numerical methods for this equation have been presented and compared: the finite difference approximation, the spectral Galerkin method and the Finite Element method. It has also been found that the finite difference approximation and the spectral Galerkin method yield, for this particular problem, the same results within the same accuracy and roughly the same computation time.

Since the *finite difference approximation* is the simplest to implement and also more intuitive, this method has been chosen for the research presented in this thesis. It is also the most common method to integrate stochastic field equations like (30) numerically. The method is based on a direct spatio-temporal discretization on a square grid (for two spatial dimensions) and discrete moments in time t_k, $k \in \mathbb{N}$ with, in general, variable time step $\Delta t_n = t_{n+1} - t_n$.

The height profile $h(\boldsymbol{r}, t)$ is defined for every instance t on a square region of the two-dimensional space $[0, L]^2 \subset \mathbb{R}^2$. In the finite difference approximation this region is divided into a lattice of N^2 squares with the lattice constant $\Delta x = \Delta y = L/N$. This way the continuous surface h is approximated by the average height $h_{i,j}^{(n)}$ of each of the squares (i, j) having the side length Δx and center coordinates $((i - \frac{1}{2})\Delta x, (j - \frac{1}{2})\Delta x)$ where $i, j = 1, \ldots, N$, at time t_n, i.e.

$$h_{i,j}^{(n)} = \frac{1}{(\Delta x)^2} \int_{(i-1)\Delta x}^{i\Delta x} \mathrm{d}x \int_{(j-1)\Delta x}^{j\Delta x} \mathrm{d}y \; h(x, y, t_n) \tag{31}$$

and its continuous evolution in time is approximately expressed by calculating $h_{i,j}^{(n)}$ for discrete times t_n. The first order finite difference scheme for the equation of the general form $\partial_t h = G[\{\nabla h\}] + \eta$ (see Eq. (4)) of the stochastic growth equation with time step Δt_n can then be expressed as:

$$h_{i,j}^{(n+1)} = h_{i,j}^{(n)} + \Delta t_n G_{i,j}[\{h_{k,l}^{(n)}\}] + q_{i,j}^{(n)} \,. \tag{32}$$

Here $q_{i,j}^{(n)}$ is the set of uncorrelated random numbers representing the contribution of the stochastic term η. Each stochastic contribution $q_{i,j}^{(n)}$ on the

rhs of equation (32) represents the noise η integrated over the time interval $[t_n, t_n + \Delta t_n]$ and spatially averaged on the (i,j)-th lattice square with the center at the point $((i-1/2)\Delta x, (j-1/2)\Delta y)$ as in the definition of $h_{i,j}^{(n)}$, equation (31):

$$q_{i,j}^{(n)} = \frac{1}{(\Delta x)^2} \int_{t_n}^{t_n+\Delta t_n} \mathrm{d}t \int_{(i-1/2)\Delta x}^{(i+1/2)\Delta x} \mathrm{d}x \int_{(j-1/2)\Delta x}^{(j+1/2)\Delta x} \mathrm{d}y\, \eta(x,y,t) \tag{33}$$

For the spatially and temporally uncorrelated (white) noise $\eta(x,y,t)$ of intensity D, the total variance of the contribution (33), $q_{i,j}^{(n)}$, is given by

$$\mathrm{Var}[q_{i,j}^{(n)}] = 2D\frac{\Delta t_n}{(\Delta x)^2}\,. \tag{34}$$

Thus the noise term can be represented by independent random variables $q_{i,j}^{(n)} = P_n \xi_{i,j}^{(n)}$ where the factor P_n,

$$P_n = \sqrt{2D\Delta t_n/(\Delta x)^2}\,, \tag{35}$$

is the rms deviation on a lattice site produced by the noise during the time Δt_n, and $\xi_{i,j}^{(n)}$ is a normally distributed random variable with the unit variance.

The resulting evolution remains practically unchanged if, instead of normally distributed, one uses uniformly between $-\frac{1}{2}$ and $\frac{1}{2}$ distributed random variables $\xi_{i,j}^{'(n)}$ whose variance is $\frac{1}{12}$ with

$$P_n' = \sqrt{24D\Delta t_n/(\Delta x)^2}\,, \tag{36}$$

because the contribution of $q_{i,j}^{'(n)}$ would produce the same zero mean $\langle q_{i,j}^{'(n)}\rangle = \langle P_n' \xi_{i,j}^{'(n)}\rangle = 0$ and the same variance $\langle (q_{i,j}^{'(n)})^2\rangle = \langle (P_n' \xi_{i,j}^{'(n)})^2\rangle = 2D\Delta t_n/(\Delta x)^2$ as the normally distributed, and their higher moments would be small, that is, of the order of $\mathcal{O}(\Delta t_n^2)$ [65].

For the derivation of the finite difference scheme of equation (29),

$$\partial_t h = a_1\nabla^2 h + a_2\nabla^4 h + a_3\nabla^2(\nabla h)^2 + a_4(\nabla h)^2 + \eta\,, \tag{37}$$

one can decompose this equation into the system of equations[9]

$$\begin{aligned} v &= (\nabla h)^2\,, \\ w &= a_1 h + a_2 \nabla^2 h + a_3 v\,, \\ \partial_t h &= \nabla^2 w + a_4 v + \eta\,. \end{aligned} \tag{38}$$

By using central difference approximations in space and an explicit Euler method in time one obtains the following detailed scheme of the procedure (32) for the model equation (37):

$$\begin{aligned} v_{i,j}^{(n)} &= \frac{1}{3(\Delta x)^2}\big[(h_{i+1,j}^{(n)} - h_{i,j}^{(n)})^2 + (h_{i+1,j}^{(n)} - h_{i,j}^{(n)})(h_{i,j}^{(n)} - h_{i-1,j}^{(n)}) \\ &\quad +(h_{i,j}^{(n)} - h_{i-1,j}^{(n)})^2 + (h_{i,j+1}^{(n)} - h_{i,j}^{(n)})^2 \\ &\quad +(h_{i,j+1}^{(n)} - h_{i,j}^{(n)})(h_{i,j}^{(n)} - h_{i,j-1}^{(n)}) + (h_{i,j}^{(n)} - h_{i,j-1}^{(n)})^2\big] \end{aligned} \tag{39}$$

$$\begin{aligned} w_{i,j}^{(n)} &= a_1 h_{i,j}^{(n)} + \frac{a_2}{(\Delta x)^2}\big[h_{i+1,j}^{(n)} + h_{i-1,j}^{(n)} \\ &\quad +h_{i,j+1}^{(n)} + h_{i,j-1}^{(n)} - 4h_{i,j}^{(n)}\big] + a_3 v_{i,j}^{(n)} \end{aligned} \tag{40}$$

$$\begin{aligned} h_{i,j}^{(n+1)} &= h_{i,j}^{(n)} + \frac{\Delta t_n}{(\Delta x)^2}\big[w_{i+1,j}^{(n)} + w_{i-1,j}^{(n)} + w_{i,j+1}^{(n)} + w_{i,j-1}^{(n)} - 4w_{i,j}^{(n)}\big] \\ &\quad +\Delta t_n a_4 v_{i,j}^{(n)} + P_n \xi_{i,j}^{(n)} \end{aligned} \tag{41}$$

Also a more straight forward finite difference approximation of $v = (\nabla h)^2$ can be used instead of (39):

$$v_{i,j}^{(n)} = \frac{1}{4(\Delta x)^2}\big[(h_{i+1,j}^{(n)} - h_{i-1,j}^{(n)})^2 + (h_{i,j+1}^{(n)} - h_{i,j-1}^{(n)})^2\big]\,. \tag{42}$$

However, [53] insists that the scheme (39)-(41) is produces better numerical stability than the scheme with (42).

In order to reduce the number of operations, one can precalculate the

[9]This decomposition is slightly different from the one presented in [53]. It has been chosen because it requires less arithmetical operations when implemented numerically.

terms that appear in the scheme multiple times:

$$
\begin{aligned}
a &= h^{(n)}_{i+1,j} - h^{(n)}_{i,j}\,, \\
b &= h^{(n)}_{i,j} - h^{(n)}_{i-1,j}\,, \\
c &= h^{(n)}_{i,j+1} - h^{(n)}_{i,j}\,, \\
d &= h^{(n)}_{i,j} - h^{(n)}_{i,j-1}\,.
\end{aligned} \tag{43}
$$

Substituting these into (39) and (40) results in the following scheme:

$$
v^{(n)}_{i,j} = \frac{1}{3(\Delta x)^2}\left[a^2 + ab + b^2 + c^2 + cd + d^2\right], \tag{44}
$$

$$
w^{(n)}_{i,j} = a_1 h^{(n)}_{i,j} + \frac{a_2}{(\Delta x)^2}\left[a + c - (b + d)\right] + a_3 v^{(n)}_{i,j}\,. \tag{45}
$$

Expressions (44),(45) with (43) and (41) with (35) constitute an explicit first order (Euler) scheme, that can be directly used to simulate the stochastic growth equation (37). In order to increase the numerical stability, one might want to implement a higher order scheme. The second order scheme that has been used in most calculations for this thesis follows directly from the so-called *Heun's method* for ordinary differential equations.[10] This method basically applies the first order scheme presented above twice. In fact, the second order scheme,

$$
\begin{aligned}
\tilde{h}^{(n+1)}_{i,j} &= h^{(n)}_{i,j} + \Delta t_n G_{i,j}[\{h^{(n)}_{k,l}\}]\,, \\
h^{(n+1)}_{i,j} &= h^{(n)}_{i,j} + \frac{\Delta t_n}{2}(G_{i,j}[\{h^{(n)}_{k,l}\}] + G_{i,j}[\{\tilde{h}^{(n+1)}_{k,l}\}]) + P_n \xi^{(n)}_{i,j}\,.
\end{aligned} \tag{46}
$$

is constructed from the first order scheme (32) as follows. First, one calculates the intermediate surface profile $\tilde{h}^{(n+1)}_{i,j}$ at time t_{n+1} from the initial profile $h^{(n)}_{i,j}$ at time t_n by using the first order scheme (32), but *without adding the noise term* $P_n \xi^{(n)}_{i,j}$.[11] For this new surface, the values of G, $G_{i,j}[\{\tilde{h}^{(n+1)}_{k,l}\}]$, are found and then

[10] A spatially discretized scheme for a PDE is, of course, equivalent to a system of coupled ordinary differential equations, so the same integration methods can be applied.

[11] In higher order schemes the noise for the intermediate stages can change in some non-trivial way. So instead of trying to evaluate these contributions, it has been chosen here to calculate the new surface by using the second order scheme without the stochastic term and then to add the stochastic term to the final result, therefore leaving it in the same form as in the first order scheme (32). Actually, it does not make a difference for the simulation results in the case of uncorrelated noise of zero mean.

the second order approximation $h_{i,j}^{(n+1)}$ is produced by adding the *average* value of G at the time t_n, $G_{i,j}[\{h_{k,l}^{(n)}\}]$, and the first order approximation of G at time t_{n+1}, $G_{i,j}[\{\tilde{h}_{k,l}^{(n+1)}\}]$, (multiplied by the time step Δt_n) and, finally, contribution of noise $P_n \xi_{i,j}^{(n)}$ to the initial $h_{i,j}^{(n)}$.

All numerical simulations of the surface growth presented in the further this work have been performed using the methods presented in this section with *periodic boundary conditions* and the following parameter values. The time step was held constant equal to $\Delta t = 0.005$ (unless stated otherwise). The lattice constant, unless stated otherwise, has been set to $\Delta x = 0.71086127010534$. Such a seemingly bizarre number for the discretization step Δx is actually a good approximation of the value that is needed in order for the system with periodic boundary conditions to be able to contain hexagonal patterns that appear in some other versions of the generalized KS equation (see for example [25, 30]).

Other numerical methods used in this work consisted mostly of implementations of algorithms for statistical analysis of the data produced by the computer simulations of (30): calculation of height distributions, autocorrelation functions and spectra, and filtering of the simulated surface profiles, also analysis of the time series for global quantities (like surface roughness) during the surface evolution. All of these were written by the author of this thesis using C programming language.

3 Deterministic gKS equation

For most part of this work, the noise term η in (30) is omitted and the deterministic version of the growth equation,

$$\partial_t h = a_1 \nabla^2 h + a_2 \nabla^4 h + a_3 \nabla^2 (\nabla h)^2 + a_4 (\nabla h)^2 \,, \tag{47}$$

is considered.

This section demonstrates how the gKS (47) can be rescaled transforming it into the dimensionless form with only one independent parameter that determines the behavior of the surfaces evolving according to this equation. The transient kinetics and the saturation in the dynamics are shown.

3.1 Dimensionless form

The equation (47) has four parameters a_1, a_2, a_3 and a_4 and three physical dimensions — height, time and length. According to dimensional analysis, it should be possible to rescale this equation and obtain a dimensionless form with only one parameter. Denoting the units for the *height*, *time* and *length* units as S_H, S_T and S_L, respectively, it is possible to express h, t and $\boldsymbol{r}$ in the corresponding dimensionless quantities $\tilde{h}$, $\tilde{t}$ and $\tilde{\boldsymbol{r}}$ as follows:

$$\begin{aligned} h &= S_H \tilde{h} \,, \\ t &= S_T \tilde{t} \,, \\ \boldsymbol{r} &= S_L \tilde{\boldsymbol{r}} \,. \end{aligned} \tag{48}$$

Since the nabla operators represent spatial derivatives, they are expressed accordingly:

$$\nabla_{\boldsymbol{r}} = S_L^{-1} \nabla_{\tilde{\boldsymbol{r}}} \equiv S_L^{-1} \tilde{\nabla} \,. \tag{49}$$

Using (48) and (49) the terms in (47) can be expressed as

$$\begin{aligned}
\partial_t h &= (S_H/S_T)\partial_{\tilde{t}}\tilde{h} \\
\nabla^2 h &= (S_H/S_L^2)\tilde{\nabla}^2\tilde{h} \\
\nabla^4 h &= (S_H/S_L^4)\tilde{\nabla}^4\tilde{h} \\
(\nabla h)^2 &= (S_H^2/S_L^2)(\tilde{\nabla}\tilde{h})^2 \\
\nabla^2(\nabla h)^2 &= (S_H^2/S_L^4)\tilde{\nabla}^2(\tilde{\nabla}\tilde{h})^2
\end{aligned} \tag{50}$$

From the latter expressions and equation (47) follow the dimensions of the coefficients a_1, a_2, a_3, a_4:

$$\begin{aligned}
[a_1] &= \left[\frac{S_L^2}{S_T}\right], \\
[a_2] &= \left[\frac{S_L^4}{S_T}\right], \\
[a_3] &= \left[\frac{S_L^4}{S_H S_T}\right], \\
[a_4] &= \left[\frac{S_L^2}{S_H S_T}\right].
\end{aligned} \tag{51}$$

The signs for the coefficients $\{a_i\}$ in 47 are fixed. They follow from the model and have been determined in Sect. 2 to be $a_1, a_2, a_3 < 0$ and $a_4 > 0$. Since it is more convenient to have all positive coefficients, we can make the following simple transformation to the new set of coefficients $\{b_i\}$,

$$\begin{aligned}
a_1 &\longrightarrow -b_1\,, \\
a_2 &\longrightarrow -b_2\,, \\
a_3 &\longrightarrow -b_3\,, \\
a_4 &\longrightarrow b_4\,,
\end{aligned} \tag{52}$$

thus, putting the gKS (47) in the form

$$\partial_t h = -b_1\nabla^2 h - b_2\nabla^4 h - b_3\nabla^2(\nabla h)^2 + b_4(\nabla h)^2 \tag{53}$$

where all coefficients are positive, i.e. $b_1, b_2, b_3, b_4 > 0$.

By substituting the expressions (50) in the equation (53), one obtains the

dimensionless form of the gKS with four dimensionless coefficients c_1, c_2, c_3, c_4:

$$\partial_{\tilde{t}}\tilde{h} = -\underbrace{b_1\frac{S_T}{S_L^2}}_{c_1}\tilde{\nabla}^2\tilde{h} - \underbrace{b_2\frac{S_T}{S_L^4}}_{c_2}\tilde{\nabla}^4\tilde{h} - \underbrace{b_3\frac{S_H S_T}{S_L^4}}_{c_3}\tilde{\nabla}^2(\tilde{\nabla}\tilde{h})^2 + \underbrace{b_4\frac{S_H S_T}{S_L^2}}_{c_4}(\tilde{\nabla}\tilde{h})^2 \qquad (54)$$

Thus, we have the equation with four dimensionless coefficients c_1, c_2, c_3 and c_4. However, since there are three physical dimensions, only one of these coefficients is independent of scaling. The value of the coefficient c_3 has been chosen as the only independent parameter of the equation in the dimensionless form and will be called α, and all of the remaining three coefficients have been set equal to 1:

$$\begin{aligned} c_1 &= b_1\frac{S_T}{S_L^2} = 1\,, \\ c_2 &= b_2\frac{S_T}{S_L^4} = 1\,, \\ c_3 &= b_3\frac{S_H S_T}{S_L^4} = \alpha\,, \\ c_4 &= b_4\frac{S_H S_T}{S_L^2} = 1\,. \end{aligned} \qquad (55)$$

The choice of the independent parameter to be the coefficient by the nonlinear term $\nabla^2(\nabla h)^2$ has been made because this term generalizes the widely known and much researched Kuramoto-Sivashinsky (KS) equation [18–21],

$$\partial_t h = -\nabla^2 h - \nabla^4 h + (\nabla h)^2\,, \qquad (56)$$

and gKS then has the KS as a special case when $\alpha = 0$.

Solving the system (55) of algebraic equations provides the scaling parameters

$$S_H = \frac{b_1}{b_4}\,, \qquad S_T = \frac{b_2}{b_1^2}\,, \qquad S_L = \sqrt{\frac{b_2}{b_1}}. \qquad (57)$$

which are needed if one desires to return to dimensional quantities.

By setting the values (55) into (54) and omitting the tildes one obtains the final form of the deterministic generalized Kuramoto-Sivashinsky equation

(gKS),

$$\partial_t h = -\nabla^2 h - \nabla^4 h - \alpha \nabla^2 (\nabla h)^2 + (\nabla h)^2 \,, \tag{58}$$

with

$$\alpha = \frac{b_1 b_3}{b_2 b_4} > 0 \tag{59}$$

which is the main object of this thesis.

It is clear from (57) that, with the particular choice (55) of dimensionless coefficients, the length scale parallel to the substrate S_L and the time scale S_T are determined by the values of the coefficients b_1 and b_2 in (53), and the height scale S_H is proportional to b_4^{-1} whereas the behavior of the equation only depends on the ratio b_3/b_4. It is sometimes convenient to have two parameters (at both nonlinear terms) in gKS. By setting $c_3 = \alpha_1$ and $c_4 = \alpha_2$ in (55), the equation can be given as

$$\partial_t h = -\nabla^2 h - \nabla^4 h - \alpha_1 \nabla^2 (\nabla h)^2 + \alpha_2 (\nabla h)^2 \,. \tag{60}$$

However, it is clear that the parameters α_1 and α_2 are not independent. Indeed, the dynamics, resulting from the equation (60) depends only on (α_1/α_2) exactly like dynamics of (58) depends on α, only the height is rescaled in the two-parameter case (60) by the factor α_2^{-1}. Nevertheless, in this form, one can see that reducing the value of α_2 by some finite factor κ^{-1}, $\kappa > 1$, does the same (up to the rescaling of the height by κ) as increasing the value of α_1 by κ.

Moreover, by choosing the single independent parameter α' to be the coefficient by the nonlinear term $(\nabla h)^2$, that is, by setting $c_3 = 1$ and $c_4 = \alpha'$ in (55), one would end up with the equation

$$\partial_t h = -\nabla^2 h - \nabla^4 h - \nabla^2 (\nabla h)^2 + \alpha' (\nabla h)^2 \,, \tag{61}$$

where

$$\alpha' = \frac{b_2 b_4}{b_1 b_3} = \alpha^{-1} \tag{62}$$

and the resulting scaling parameters

$$S_H = \frac{b_2}{b_3} \,, \qquad S_T = \frac{b_1}{b_2^2} \,, \qquad S_L = \sqrt{\frac{b_2}{b_1}} \,. \tag{63}$$

Then the limiting case $\alpha' \to 0$ in this equation resulting in the so-called con-

served Kuramoto-Sivashinsky equation (cKS) [52],

$$\partial_t h = -\nabla^2 h - \nabla^4 h - \nabla^2 (\nabla h)^2 \,, \tag{64}$$

would correspond to the limit $\alpha \to \infty$ in (58).

3.2 Kinetics produced by the gKS: initial stages and saturation

In almost all of the numerical simulations presented in this work we will use the rescaled form of the deterministic gKS equation (58),

$$\partial_t h = -\nabla^2 h - \nabla^4 h - \alpha \nabla^2 (\nabla h)^2 + (\nabla h)^2 \,, \tag{65}$$

with a single independent parameter α.

In this thesis, the generalized gKS without the noise term — as well as the stochastic growth equation (29), discussed in Sect.2 — is interpreted as an evolution equation for some surface profile $h(\boldsymbol{x}, t)$. Computer simulations on the gKS (65) show that the resulting surface morphologies and the kinetics of statistical parameters, like surface roughness, are very similar to those of the stochastic model equation (30) for moderate noise levels. At the initial stages (starting from an almost flat surface), the evolution is also dominated by the linear terms $-\nabla^2 h$ and $-\nabla^4 h$, and thus results in the exponential growth of modes around the critical wavelength $k_c = 1/\sqrt{2}$ (see the argument in Sect. 2, Subsect. 2.2). In the very short time, this critical mode starts to dominate the surface profile and, as a result, the surface roughness w also grows at the exponential rate. At later stages, the nonlinear terms $-\alpha \nabla^2 (\nabla h)^2$ and $(\nabla h)^2$ become more important. The term $(\nabla h)^2$, known from the KPZ equation (3), see Sect. 1, leads to the slowing down of the exponential roughening and, eventually, causes the kinetics to saturate into a stationary behavior which then persists in the long time limit. The other nonlinear term $\nabla^2 (\nabla h)^2$ causes the coarsening of the small scale pattern, that is, it leads to the increase in size of the individual humps in the cellular patterns, as will be demonstrated in later sections.

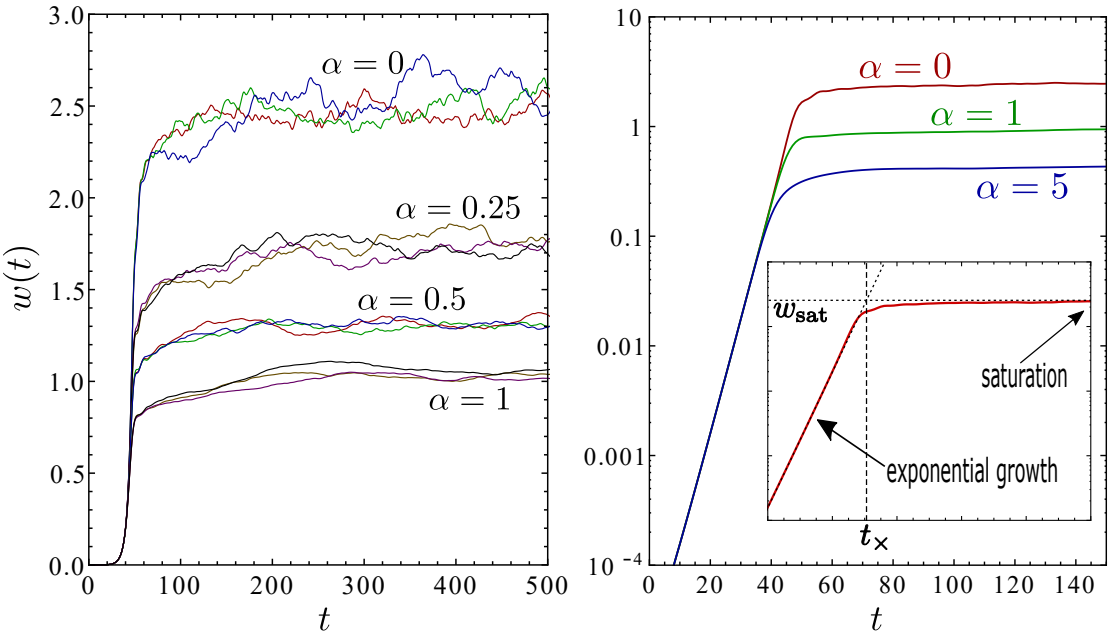

Figure 6: Initial transient kinetics of the roughness $w(t)$, (67), of a surface evolving accourding to (1) with several values of parameter α. Each simulation starts from a random uncorrelated surface profile with initial roughness $w(0) = 10^{-4}$. The left panel shows $w(t)$ on linear scale for 3 realizations with each α. The right panel highlights the initial exponential increase of $w(t)$ by using a semi-logarithmic scale. The inset demonstrates the saturation roughness $w_{\rm sat}$ and the cross-over time $t_\times$.

3.3 Transient dynamics and saturation

In computer simulations presented in this work, the equation (65) is solved numerically for different values of α using the methods presented in Sect. 2, Subsect. 2.3 with periodic boundary conditions, the time step $\Delta t = 0.005$, and spatial discretization step $\Delta x = 0.71086127010534$, unless stated otherwise. The equation is solved for system sizes L ranging from about 36 to about 1422 (i.e., on the $N \times N$ lattices with N from 50 to 2000, where $L = N\,\Delta x$).

In the KS case ($\alpha = 0$), the evolving surfaces reach the regime where the dynamics is chaotic, but statistically stationary. This type of behaviour also persists for $\alpha > 0$, at least up to $\alpha = 5$. However, for larger values of α, this stationary chaotic behaviour gives way to non-stationary effects that prevent the saturation in the surface evolution. Indeed, in the limiting case when $\alpha \to \infty$ in (65), by rescaling h, one arrives at the conserved Kuramoto-Sivashinsky equation [52] (see Subsect. 3.1 of this section),

$$\partial_t h = -\nabla^2 h - \nabla^4 h - \nabla^2 (\nabla h)^2 \,, \tag{66}$$

which produces a non-stationary regime with ever increasing surface roughness due to the uninterrupted coarsening of the surface patterns. Thus, by increasing α, there must be a route from the stationary chaotic evolution (Sect. 6) to non-stationary coarsening behaviour (Sect. 8). The coarsening behaviour for relatively larger parameter values (up to $\alpha = 50$) has been investigated in a one-dimensional case and, to some extent, in the two dimensional case [66]. Nonetheless, the long-time behaviour at the intermediate α values seems to be quite complicated and has not been studied in detail so far. The author of this work offers his humble contribution on the matter in Sect. 8 of this thesis.

Even though negative α values do not follow from surface growth or erosion models (see, e.g., [9,15]), it is desirable to understand the dynamics in that range for completeness.

However, the range of negative α values available for investigation is limited. In our numerical simulations with $\alpha < -0.14$, we find that large local gradients in the surface emerge and grow. They eventually exceed the numerical capacity of the simulation, thus making the required long-time calculations unstable. The reason for this most likely are the so-called *cancellation modes* (see, e.g., [15, 67]). Indeed, when $\alpha < 0$, the contributions of the nonlinear terms in (65) cancel each other out for some mode, so that the dynamics of this mode is governed only by the linear part of (65). If, moreover, the wave number of this mode belongs to the linearly unstable band, then its amplitude blows up exponentially, thus, causing the simulation to break down.

Therefore, this work (with the exception of Sect. 8) focuses on the evolution of surfaces produced by (65) in a moderate range, $-0.12 \leq \alpha \leq 5$, of parameter values where the long time behaviour is stationary.

One of the most important quantities characterizing a surface [51, 57] is the surface *roughness* $w(t)$, also called the *surface width*:

$$w(t) := \sqrt{\left\langle \left(h(\boldsymbol{r},t) - \bar{h}(t)\right)^2 \right\rangle_{\boldsymbol{r}}}\,. \tag{67}$$

The scaling properties of this quantity are often used to characterize and classify various surface growth models into various universality classes [22, 35, 43, 51]. The roughness of an evolving surface changes with time. In the range of parameter values considered here, the kinetics of $w(t)$ due to the surface evolution

according to (65) seems to follow a distinct pattern (see, e.g., [7,9,10,52,68]): starting from a random surface with some small initial roughness $w(t=0) \ll 1$ the instability produced by the linear part of (65) dominates over nonlinear terms, and the roughness begins to grow at an exponential rate, but at some time $t_\times < 100$ this growth slows down significantly, and, eventually, crosses over to a stationary regime where it oscillates about some average (*saturation*) value w_{sat}. This transient behaviour is shown in Fig. 6) for several parameter values. For large enough systems another regime can be observed where $w(t)$ exhibits growth that is much slower than the initial exponential increase. For $\alpha = 0$ (KS case), this growth is approximately $w(t) \sim \sqrt{\log t}$, as shown in Fig. 7 where the growth $w^2(t) \sim \log t$ appears as a straight line in the log-linear scale, which is consistent with pre-saturation behavior reported in [44]. The duration of this regime before finally reaching saturation increases with increasing system size which suggests that this growth is due to the development of large-scale height variations (see Sect. 4).

The value of saturated surface roughness can be defined as follows:

$$w_{\mathrm{sat}} = \lim_{T\to\infty} \left\langle w(t) \right\rangle_{t\in[t_0,\, t_0+T)} . \tag{68}$$

Here $t_0 \gg t_\times$ is a time at which all initial transient effects have decayed and are virtually undetectable, i.e., the time at which the stationary regime has been reached. In practice, the total observation time T has to be much larger than the typical time scale in the kinetics of $w(t)$. In the investigation presented here, the saturation values for surface roughness w_{sat} are calculated using $t_0 = 2 \cdot 10^4$ and $T = 8 \cdot 10^4$. Note that these times are significantly larger than those recently achieved by Muñoz-Garcia et. al. in the numerical investigation of an equation equivalent to (65) in the one-dimensional case [16, 17]. There, although the 'interrupted coarsening' is observed, the saturated stationary regime appears not to have been fully reached.

The surface roughness $w(t)$ represents the integral effect of all modes contributing to the surface morphology. Therefore, in this work, the time series of chaotic fluctuations of $w(t)$ in the stationary regime are used to investigate the long-time dynamics of surfaces, in particular, the temporal behaviour of the large-scale height variations observed in Ref. [7].

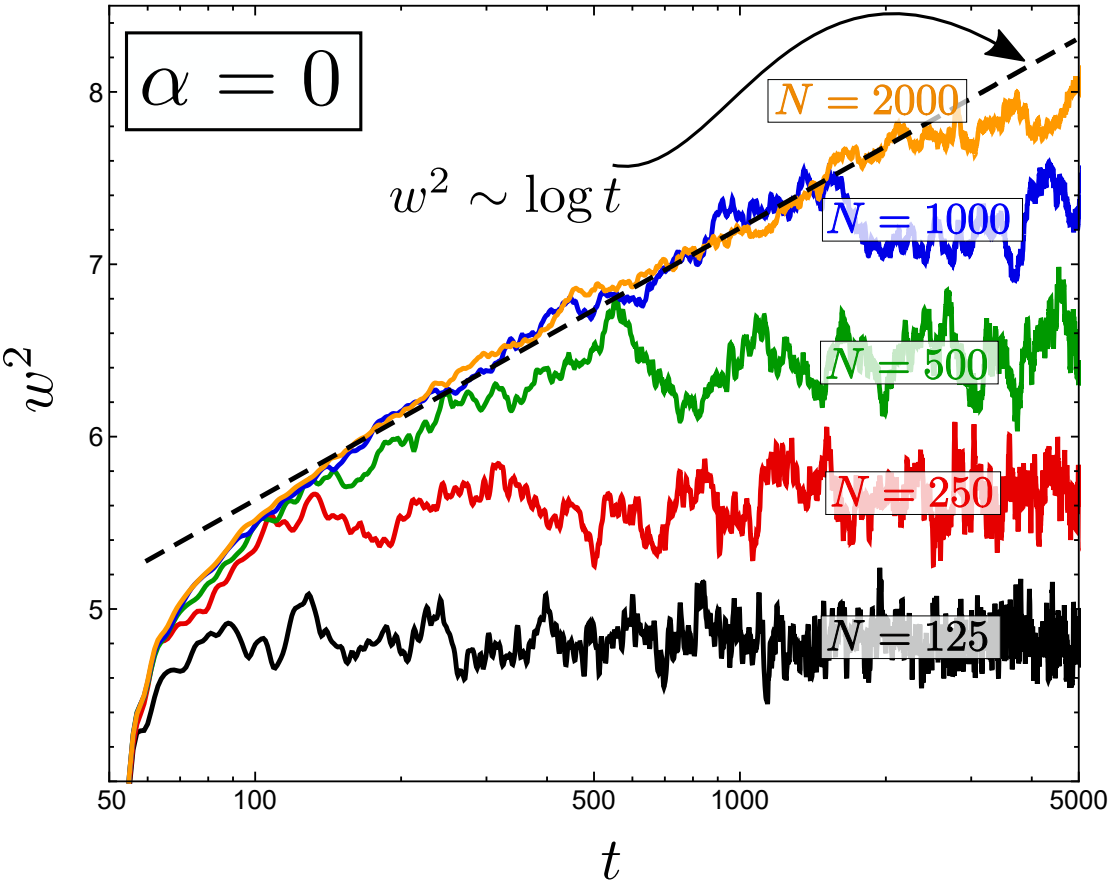

Figure 7: Transient bahavior of $w^2(t)$ (each curve is an ensemble average of 10 to 30 realizations) for $\alpha = 0$ and system sizes (in lattice units) $N = 125$ (black), $N = 250$ (red), $N = 500$ (green), $N = 1000$ (blue), $N = 2000$ (orange). Black dashed line corresponds to the logarithmic fit for the $N = 2000$ case. The corresponding system sizes L can be found from $L = N\Delta x$ where $\Delta x \approx 0.711$ is the spatial discretization step used in the simulations.

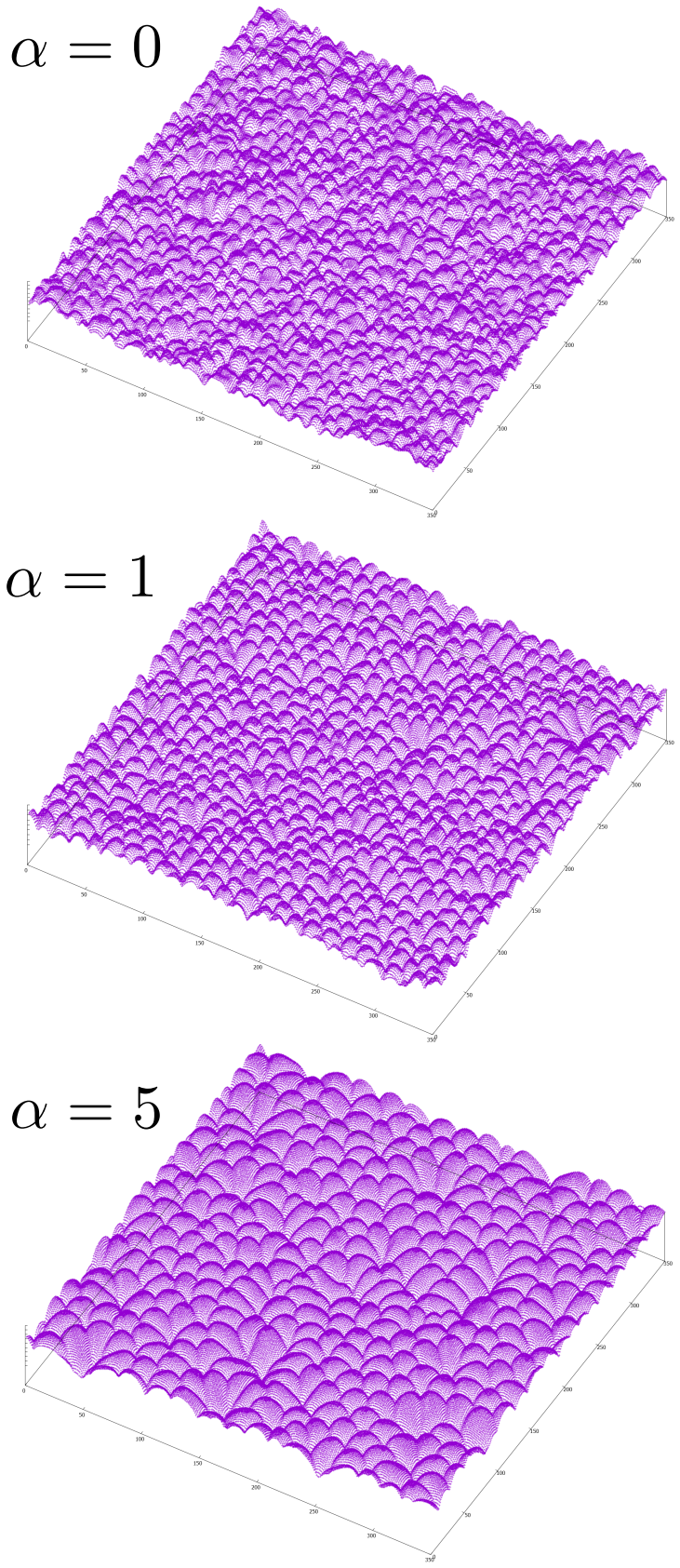

Figure 8: Surface morphologies produced by (69) for different parameter values at system size $N = 350$ ($L \approx 249$).

4 Characterization of surface morphologies and the scaling of roughness

The surface profiles produced by gKS (65),

$$\partial_t h = -\nabla^2 h - \nabla^4 h - \alpha \nabla^2 (\nabla h)^2 + (\nabla h)^2 \,, \tag{69}$$

in the stationary regime have a disordered cellular structure on the small scales and slow height variations over the entire system [7,9] (c.f. Fig. 10 and Fig. 11). This section presents the quantities used to statistically describe the geometry of these surfaces and then goes on to show how these quantities depend on the parameter α and the system size in the gKS (69) model.

4.1 Height distributions

One important characteristic in the statistical description of the morphology of disordered surfaces is its height distribution. Since the average height plays virtually no role in the present investigation, the height fluctuation $\Delta h = h - \bar{h}$, i.e., the deviation from the average $\bar{h}$ is considered. In order to estimate the probability density of Δh, first the rms deviation of the surface height h from its average (equivalent to the surface roughness), $w = \sqrt{\langle (h - \bar{h})^2 \rangle}$, is calculated. Then the interval equal $\mathcal{I} = [-a_{\mathrm{lo}} w, a_{\mathrm{hi}} w)$ is divided into N_{b} non-overlapping subintervals (or 'boxes') of equal size:

$$\mathcal{I}_k = [h_k, h_{k+1}) \tag{70}$$

where

$$h_k = w\Big(\frac{a_{\mathrm{hi}} + a_{\mathrm{lo}}}{N_{\mathrm{b}}}(k-1) - a_{\mathrm{lo}}\Big) \,, \quad k = 1, 2, \ldots, N_{\mathrm{b}} \,. \tag{71}$$

The lower and upper limits (in standard deviation w units) $a_{\mathrm{lo}} > 0$ and $a_{\mathrm{hi}} > 0$ of the interval $\mathcal{I} = [-a_{\mathrm{lo}} w, a_{\mathrm{hi}} w)$ are chosen in such a way that most of the heights on the lattice (usually over 99%) belong to this interval. In this work it has been found that $a_{\mathrm{lo}} = a_{\mathrm{hi}} = 4$ and $N_{\mathrm{b}} = 100$ gives reasonably good results.

The probability density $p(\Delta h)$ is then estimated as

$$p(\Delta h) = \frac{n_k}{n_{\mathrm{tot}}\, s_h} \tag{72}$$

with n_k being the number of points where $\Delta h \in \mathcal{I}_k$, n_{tot} being the total number of points where $\Delta h \in \mathcal{I}$, and $s_h = |\mathcal{I}_k| \equiv w(a_{\mathrm{hi}} + a_{\mathrm{lo}})/N_{\mathrm{b}}$ is the size of the box (subinterval $\mathcal{I}_k$). Some probability densities estimated in this way from the simulation results are shown in Fig. 9.

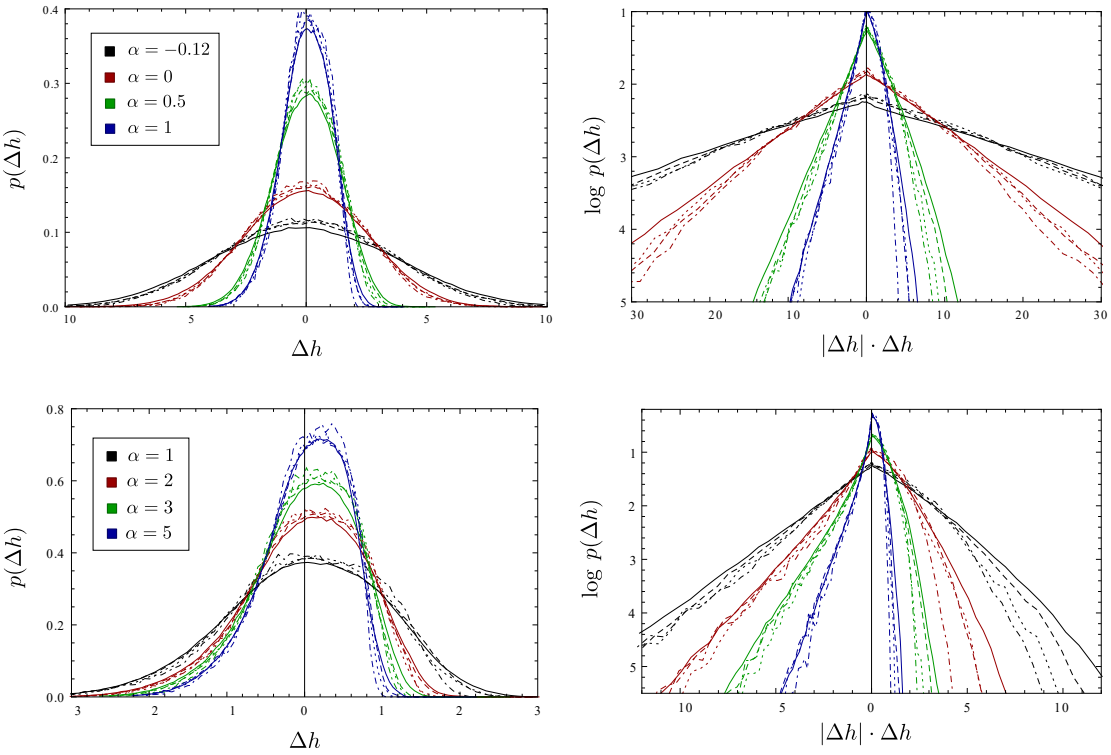

Figure 9: Estimations of the height fluctuation Δh probability densities in the surfaces produced by the gKS (69) in the stationary regime, $t = 10^5$, with different parameter α values and various system sizes (in lattice units N): $N = 150$ (dot-dashed lines), $N = 200$ (dotted lines), $N = 300$ (dashed lines), $N = 500$ (solid lines). Top half: $\alpha = -0.12,\ 0,\ 0.5,\ 1$, bottom half: $\alpha = 1,\ 2,\ 3,\ 5$. Left half: probability densities $p(\Delta h)$ plotted directly. Right half: the same probability densities plotted as $\log p(\Delta h)$ vs $|\Delta h| \cdot \Delta h$ in order to compare them with the normal (Gaussian) distributions which would appear as straight lines forming a triangle with the symmetry axis Δh when plotted this way.

One might wish to compare the resulting probability densities with the normal (Gaussian) probability density,

$$p_{\mathrm{Gauss}}(\Delta h) \propto \exp\left(-\frac{(\Delta h)^2}{2w^2}\right). \tag{73}$$

By denoting $u = \log p_{\mathrm{Gauss}}$ and $v = |\Delta h|\,\Delta h$ one obtains from (73) the following expression:

$$u(v) = \mathrm{const} - \frac{|v|}{2w^2} \tag{74}$$

which has the shape of a 'tent' — an isosceles triangle with the symmetry axis at $v = 0$. Therefore, by plotting the transformed probability densities $\log p$ vs $|\Delta h|\Delta h$, as shown on the right half of Fig. 9, it is easy to visually compare them to those produced by the normally distributed quantities. One can see that at, small parameter values α in (69), the probability densities of Δh are symmetric and quite similar to those of normally distributed quantities, but by increasing the parameter value the resulting distributions become not only narrower, but also increasingly negatively skewed, thus, deviate further from the normal distribution. This negative skew can be explained by considering the morphologies of the surfaces. When the parameter is increased, the long range height variations are diminished and, at the same time, the small-scale surface patterns grow larger in size forming round bumps with peaks at a very similar height separated by deep sharp valleys, as can be clearly seen in their morphologies Fig. 8 and autocorrelation functions Fig. 10. This results in the negatively skewed distributions.

4.2 Height autocorrelation and surface spectrum

The height distributions give the range of the expected surface height fluctuations. However, it does not convey any information about how these height fluctuations are correlated in space. Therefore other quantities must be used in order to describe surface morphology.

The usual way to investigate the surface patterns is by calculating the surface height-height correlation function $C(\boldsymbol{r})$, which is the two-dimensional autocorrelation function of the surface height $h(\boldsymbol{r})$:

$$C_{\mathrm{2D}}(\boldsymbol{r}) = \left\langle (h(\boldsymbol{r'}) - \bar{h})\,(h(\boldsymbol{r'} + \boldsymbol{r}) - \bar{h}) \right\rangle_{\boldsymbol{r'}}. \tag{75}$$

Since (69) is isotropic, and, consequently, the resulting profiles have no distinct direction on the $\boldsymbol{r}$-plane, the surface morphologies can be investigated by using the surface height autocorrelation function averaged over all directions

at a distance $r = |\boldsymbol{r}|$ that only has the radial dependence:

$$C(r) = \left\langle \left\langle (h(\boldsymbol{r'}) - \bar{h})\,(h(\boldsymbol{r'} + \boldsymbol{r}) - \bar{h}) \right\rangle_{\boldsymbol{r'}} \right\rangle_{|\boldsymbol{r}|=r} . \tag{76}$$

The isotropic height-height correlation function $C(r)$ (76) gives a good description of disordered surface morphologies. An equivalent, and in some cases more intuitive, description is given by the surface spectrum which we define in the following.

In order to avoid the zero wavenumber mode, we consider the 'centered' surface profile $h_{\mathrm{c}}(\boldsymbol{r}) = h(\boldsymbol{r}) - \bar{h}$ whose average height is subtracted.

A two dimensional Fourier transformation of such surface profile is

$$h_{\boldsymbol{k}} = \int \mathrm{d}^2\boldsymbol{r}\, h_{\mathrm{c}}(\boldsymbol{r})\, \exp(-\mathrm{i}\boldsymbol{k}\cdot\boldsymbol{r})\,, \tag{77}$$

and its *two-dimensional power-spectral density* can be expressed

$$S_{2\mathrm{D}}(\boldsymbol{k}) = \frac{1}{L^2}|h_{\boldsymbol{k}}|^2\,. \tag{78}$$

Now, from the Parseval's identity it follows that

$$\frac{1}{(2\pi)^2}\int \mathrm{d}^2\boldsymbol{k}\,|h_{\boldsymbol{k}}|^2 = \int \mathrm{d}^2\boldsymbol{r}\,\big(h_c(\boldsymbol{r})\big)^2\,. \tag{79}$$

Therefore, recalling that the square of the surface roughness is defined as the variance of the height profile,

$$w^2 \equiv \mathrm{Var}[h] = \big\langle \big(h_c(\boldsymbol{r})\big)^2 \big\rangle_{\boldsymbol{r}} = \frac{1}{L^2}\int \mathrm{d}^2\boldsymbol{r}\,\big(h_c(\boldsymbol{r})\big)^2\,, \tag{80}$$

from (78) follows that it can be expressed as the integral of the power spectral density:

$$w^2 = \frac{1}{(2\pi)^2}\int \mathrm{d}^2\boldsymbol{k}\, S_{2\mathrm{D}}(\boldsymbol{k})\,. \tag{81}$$

Since the surfaces considered in this work are statistically isotropic, it is desirable to have a $one-dimensional$ surface spectrum $S(k)$ that depends only on the wave number $k = |\boldsymbol{k}|$. The main requirement in defining such a spectrum is that it should relate to the square of the surface roughness w^2 in an analogous

way as the two-dimensional spectrum $S_{2\mathrm{D}}(\boldsymbol{k})$ in (81), that is,

$$w^2 \equiv \mathrm{Var}[h] =: \frac{1}{2\pi}\int \mathrm{d}k\, S(k)\,. \tag{82}$$

By expressing the double integral in (81) in polar coordinates $\boldsymbol{k} = (k, \phi)$,

$$\frac{1}{(2\pi)^2}\int \mathrm{d}^2\boldsymbol{k}\, S_{2\mathrm{D}}(\boldsymbol{k}) = \frac{1}{(2\pi)^2}\int \mathrm{d}k\, k \int_0^{2\pi} \mathrm{d}\phi\, S_{2\mathrm{D}}(\boldsymbol{k}(k,\phi))\,,$$

and performing the integration over the angles ϕ, it is easy to see that the one-dimensional spectrum defined in (82) is expressed as

$$S(k) = k\,\langle S_{2\mathrm{D}}(\boldsymbol{k})\rangle_{|\boldsymbol{k}|=k}\,, \tag{83}$$

or, substituting (78), as

$$S(k) = \frac{k}{L^2}\langle |h_{\boldsymbol{k}}|^2\rangle_{|\boldsymbol{k}|=k}\,. \tag{84}$$

The Wiener-Khinchin theorem, applied for the two-dimensional case, states that the two-dimensional surface power-spectral density $S_{2\mathrm{D}}(\boldsymbol{k})$ (78) can be expressed as the Fourier transform of the two-dimensional autocorrelation function $C_{2\mathrm{D}}(\boldsymbol{r})$ (75),

$$C_{2\mathrm{D}}(\boldsymbol{r}) = \left\langle (h(\boldsymbol{r'}) - \bar{h})\,(h(\boldsymbol{r'}+\boldsymbol{r}) - \bar{h})\right\rangle_{\boldsymbol{r'}}\,. \tag{85}$$

This can be easily shown by substituting (77) into (78),

$$S_{2\mathrm{D}}(\boldsymbol{k}) = \frac{1}{L^2}\int d^2\boldsymbol{r'} \int d^2\boldsymbol{r''}\, h_c(\boldsymbol{r'})\, h_c(\boldsymbol{r''}) e^{-i\boldsymbol{k}\cdot(\boldsymbol{r''}-\boldsymbol{r'})}\,. \tag{86}$$

Changing the variable $\boldsymbol{r''} \to \boldsymbol{r'} + \boldsymbol{r}$ and switching the order of integration results in

$$S_{2\mathrm{D}}(\boldsymbol{k}) = \int d^2\boldsymbol{r}\, e^{-i\boldsymbol{k}\cdot\boldsymbol{r}}\frac{1}{L^2}\int d^2\boldsymbol{r'}\, h_c(\boldsymbol{r'})\, h_c(\boldsymbol{r'}+\boldsymbol{r})\,, \tag{87}$$

where

$$\frac{1}{L^2}\int d^2\boldsymbol{r'}\, h_c(\boldsymbol{r'})\, h_c(\boldsymbol{r'}+\boldsymbol{r}) \equiv \left\langle h_c(\boldsymbol{r'})\, h_c(\boldsymbol{r'}+\boldsymbol{r})\right\rangle_{\boldsymbol{r'}} = C_{2\mathrm{D}}(\boldsymbol{r}) \tag{88}$$

is the height correlation function of the surface $h(\boldsymbol{r})$. Thus, finally, we get

$$S_{2\mathrm{D}}(\boldsymbol{k}) = \int \mathrm{d}^2\boldsymbol{r}\; C_{2\mathrm{D}}(\boldsymbol{r})\, \mathrm{e}^{-\mathrm{i}\boldsymbol{k}\cdot\boldsymbol{r}} \tag{89}$$

which is exactly the statement of Wiener-Khinchin theorem.

From (89) the expression relating the one-dimensional correlation $C(r)$ and spectrum $S(k)$ is obtained as follows.

Taking an average over all directions of $\boldsymbol{k}$ on the lhs of (89) results in the integration over all directions of $\boldsymbol{r}$ on the rhs, since $C_{\mathrm{2D}}(\boldsymbol{r})$ should not depend on the direction of $\boldsymbol{r}$, and the scalar product $\boldsymbol{k} \cdot \boldsymbol{r} = kr\cos\phi$ depends only on the relative angle ϕ, thus, the integration over all $|\boldsymbol{k}| = k$ is equivalent to the integration over all $|\boldsymbol{r}| = r$. Thus, using (83), the final relation between the one-dimensional surface spectrum $S(k)$ (82) and the radial height correlation function $C(k)$ (76) results as [7, 69]:

$$S(k) = k\,2\pi \int \mathrm{d}r\, r\, C(r)\, J_0(kr)\,. \tag{90}$$

Here $J_0(kr)$ is the Bessel function of the 1st kind:

$$J_0(kr) = \frac{1}{2\pi}\int_0^{2\pi} \mathrm{d}\phi\, \mathrm{e}^{\mathrm{i}kr\cos\phi}\,. \tag{91}$$

Examples of numerically calculated surface PSD $S(k)$ using (76)-(91) for $\alpha = 0$ and $\alpha = 1$ first calculated in [7] can be seen in Fig. 12. There, one can see a distinct peak that corresponds to an average size of a hump-shaped cells in the surface pattern (see Figs. 10 and 11), and a power-law trend for small wave numbers.

4.3 Numerical results

Fig. 10 shows some of the resulting surface patterns and the corresponding normalized height correlation functions $C(r)/w^2$ for relatively small systems (of size $N = 200$, in lattice units) for different parameter α values. The shape of the autocorrelation function at smaller distances gives an insight into the small-scale surface patterns. For example, in Fig. 10, one can see how the cellular patterns change, by increasing α: the autocorrelation function (76) changes from monotonically decreasing at $\alpha = -0.12$ (corresponding to 'flaky' surface profiles, with 'flakes' of widely varying size) to having a short flat region at $\alpha = 0$ (corresponding to a profile with 'cells' of similar size), and to a function with at least one distinct peak at $\alpha > 0$ whose distance increases with α (corresponding

to the surface 'cells' becoming almost round 'humps' whose size increases with α). See Sect. 5 for a broader discussion of these small-scale patterns.

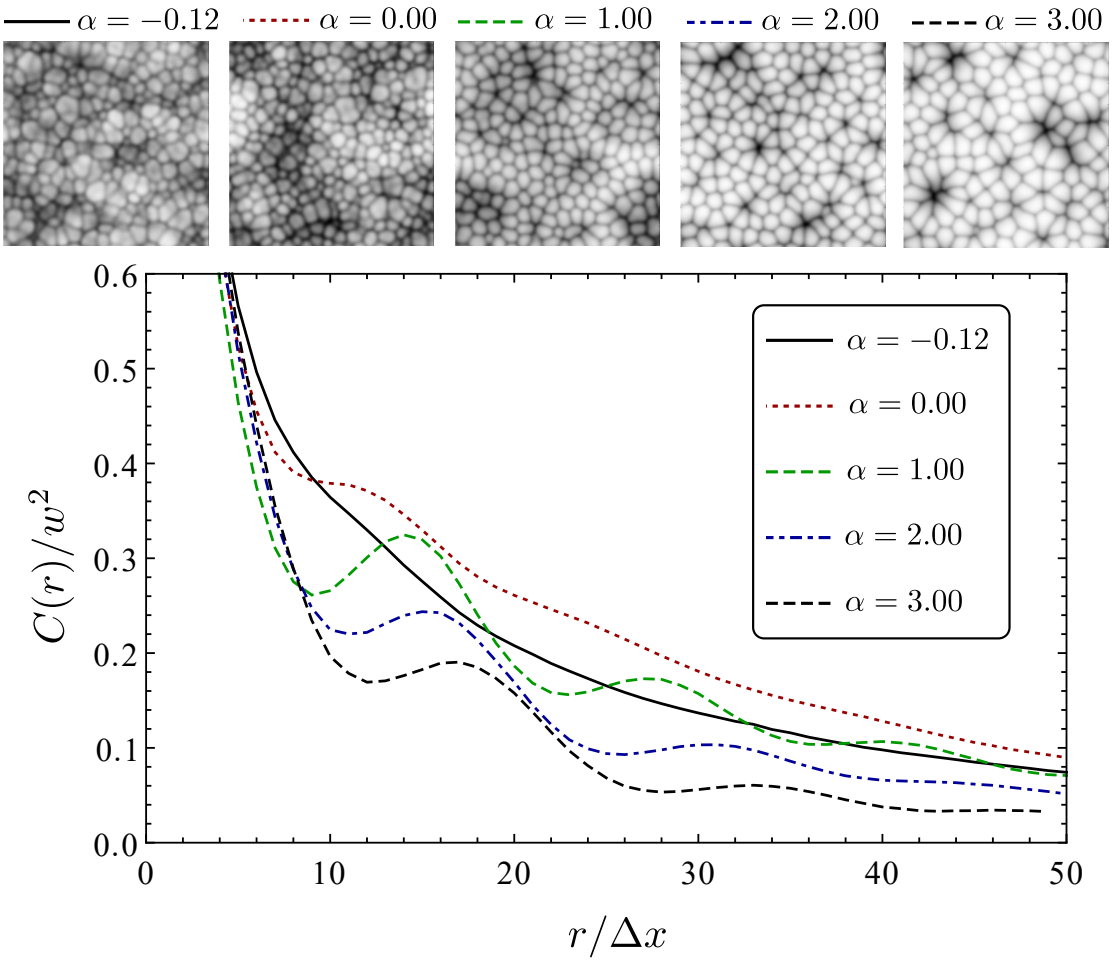

Figure 10: Top panel: Surfaces $h(\boldsymbol{r}, t)$ (values of the surface height h coded in gray-scale) evolving according to (69) at system size $N = 200$ ($L \approx 142$) with parameters $\alpha = -0.12, \ldots, 3$ at time $t = 10^5$ (in the stationary regime). Bottom panel: Normalized autocorrelation functions $C(r)$ as defined in (76) of the surfaces that are shown in the top panel.

Another thing that can be noticed in Fig. 10 is that the normalized correlation function $C(r)/w^2$ decays slowly for $\alpha = 0$ and faster for increasing α. Also, perhaps surprisingly, the autocorrelation function for $\alpha < 0$ decays faster than for $\alpha = 0$. These are the first indications of the influence of parameter α on long-range height correlations.

Simulations show that the resulting saturated surface roughness (68) increases with the system size. This indicates that the surface profiles of larger systems contain additional spatial Fourier components of smaller wave number k, since the structure on smaller scales remains virtually unchanged [7].

Large-scale height variations in surfaces produced by (69) become more distinct as the system size is chosen to be many times larger than the typical cell size (see Fig. 11).

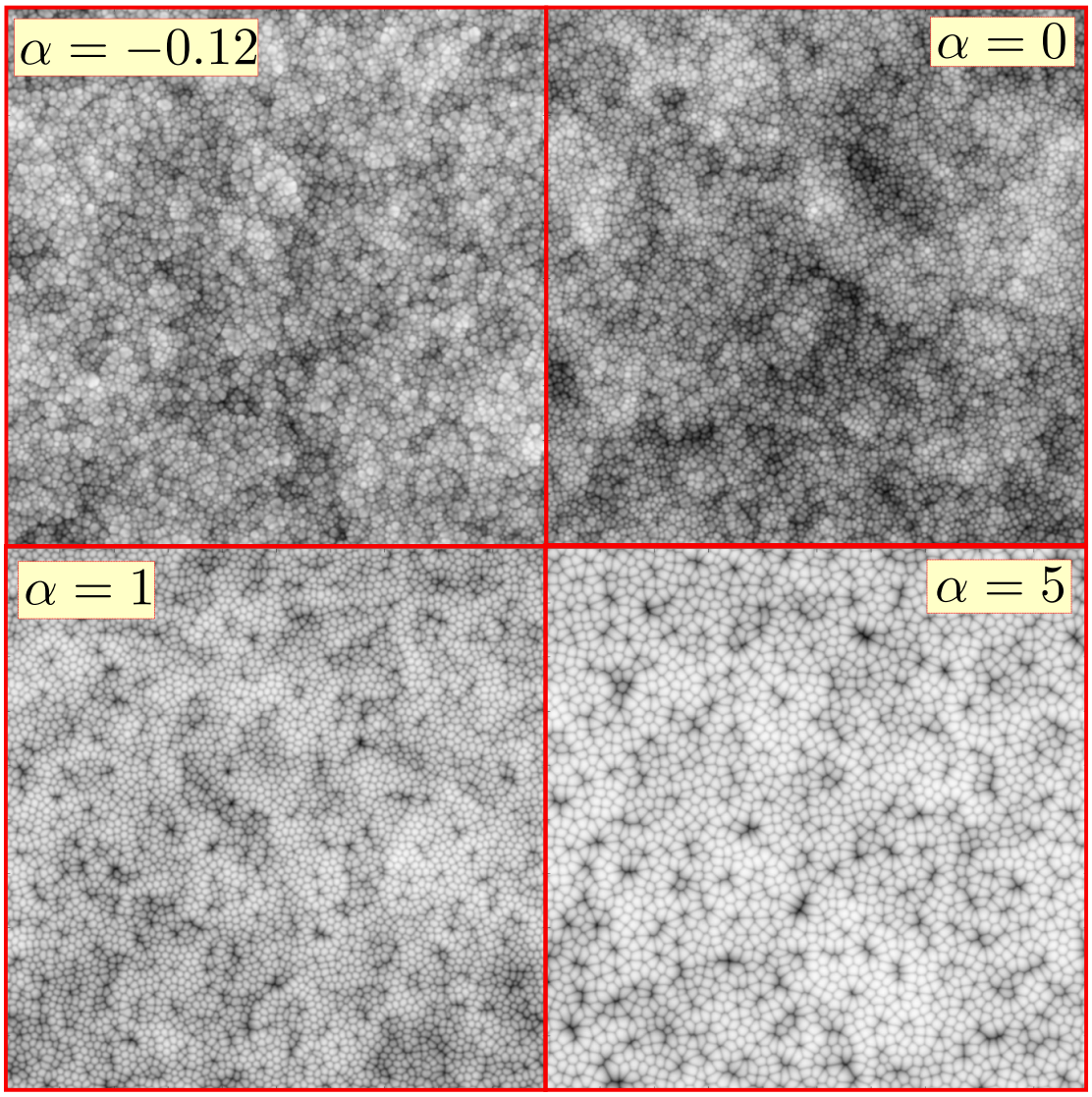

Figure 11: Surfaces (values of the surface height h coded in gray-scale) for the system size $N = 1000$ ($L \approx 711$) evolving according to (69) with parameters $\alpha = -0.12,\ 0,\ 1,\ 5$ at time $t = 6 \cdot 10^4$.

4.4 Finite-size scaling of roughness

As shown before in (82), the integral of the PSD $S(k)$ (90) over all wave numbers k equals the variance of the surface profile which is the square of surface roughness:

$$\frac{1}{2\pi} \int \mathrm{d}k\, S(k) = w^2 \ . \tag{92}$$

Since the surfaces in numerical simulations are represented on a discrete $(N \times N)$ lattice of finite size L with a discretization step Δx and periodic boundary conditions, the wave numbers that can fit into the system are $k_n = n\Delta k$ with $n = 1, \ldots, N$ and $\Delta k = 2\pi/L$. For large enough systems with $N \gg 1$, according to (92), the square of the surface roughness can then be approximated as:

$$w^2 \approx \frac{1}{2\pi} \int_{k_{\min}}^{k_{\max}} \mathrm{d}k \, S(k) \;, \tag{93}$$

where

$$k_{\min} \approx \frac{2\pi}{L} = \frac{2\pi}{N\Delta x} \,, \quad k_{\max} \approx \frac{2\pi}{\Delta x} \,. \tag{94}$$

If the discretization step Δx is kept constant (implying $k_{\max} = \mathrm{const}$), and the surface patterns at different system sizes L (up to the smallest wave number $k_{\min} \propto L^{-1}$) remain statistically the same, then, by increasing the system size L, the calculated dependence $w^2(L)$ should yield, according to (94), the shape of the surface PSD $S(k)$ for small wave numbers $k \to 0$.

Fig. 12 shows examples of surface spectra $S(k)$ defined in this section. From these, one can clearly see that, by increasing the system size, new low-wavenumber spatal modes appear producing the apparent power-law shape spectrum, while the small-scale patterns corresponding to higher wavenumbers remain virtually unchanged. This supports the following consideration in [7] where an assumption was made that the PSD $S(k)$ (90) of surfaces produced by (69) has a power-law shape for small wave numbers (below some value k_{s}):

$$S(k) = C\, k^{-\gamma} \;\; \text{for} \;\; k < k_{\mathrm{s}} \,. \tag{95}$$

By substituting (95) into (93), one gets three qualitatively distinct scaling behaviours $w^2(L)$ for $L > 2\pi\, k_{\mathrm{s}}^{-1}$, depending on the value of spectral exponent γ in (95):

$$\begin{cases} w^2(L) = C_1 - C_2\, L^{-(1-\gamma)} & \text{for} \quad \gamma < 1 \\ w^2(L) = C \ln L + B & \text{for} \quad \gamma = 1 \\ w^2(L) = D_1 + D_2\, L^{\gamma-1} & \text{for} \quad \gamma > 1 \end{cases} \tag{96}$$

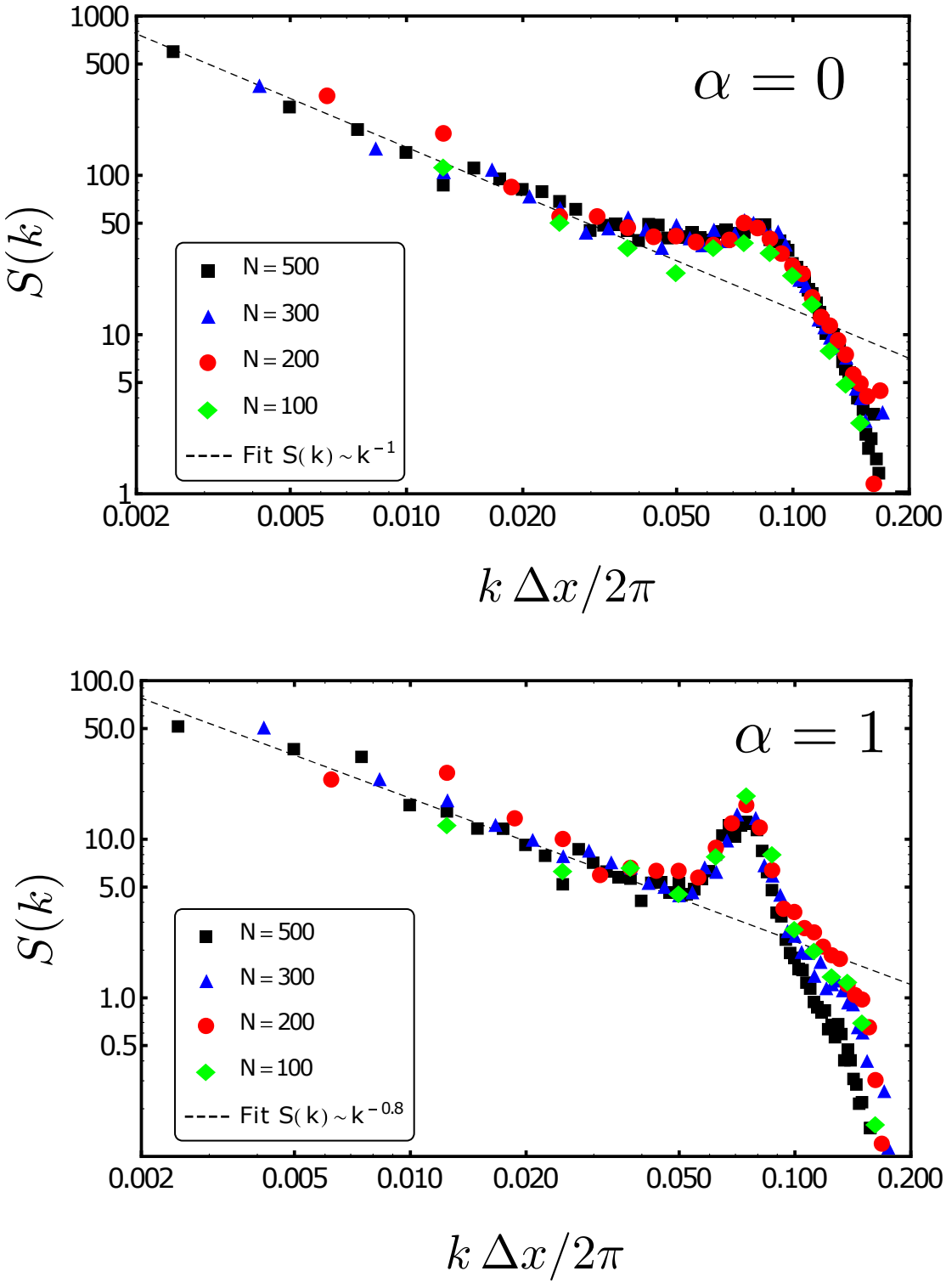

Figure 12: Surface spectra $S(k)$ defined as (84) and calculated from (90) for parameter values $\alpha = 0$ and $\alpha = 1$, each calculated for several system sizes ranging from $N = 100$ to $N = 500$. Dashed lines show power-law fits at small wave numbers k.

For asymptotically large systems $L \to \infty$, (96) would become

$$\begin{cases} w^2(L) \sim \text{const} & \text{for} \quad \gamma < 1 \\ w^2(L) \sim \ln L & \text{for} \quad \gamma = 1 \\ w^2(L) \sim L^{\gamma-1} & \text{for} \quad \gamma > 1\,, \end{cases} \tag{97}$$

corresponding to asymptotically constant roughness for $\gamma < 1$, logarithmically increasing square of the surface roughness for $\gamma = 1$, and power-law scaling for $\gamma > 1$.

It has been shown in [7] that the assumption (95) of a power-law surface PSD with $(0 < \gamma \leq 1)$ at small wave numbers is indeed valid for surfaces produced by (69) with parameter values $0 \leq \alpha \leq 1$, since the relations (96) fit the numerically calculated surface roughness exceptionally well.

Investigations of a broader parameter range, $-0.12 \leq \alpha \leq 5$, presented in [47], show that the same assumption (95) also holds for other parameter values. Fig. 13 and Fig. 14 show the calculated square of the surface roughness w^2 dependence on the system size $L = N\Delta x$. In order to fit the results with different α values in the same plot, the numerical results and their fits for each α have been divided by the corresponding w^2 values at $N = 250$. At $\alpha = 0$ the resulting spectral exponent $\gamma = 1$ gives the logarithmic dependence $w^2(N)$ (see (96)) which is a straight line in the log-linear scale. This scaling is the same as found by Manneville and Chaté for the two-dimensional KS equation [44] and corresponds to the EW type of behaviour [45] which is the pre-asymptotic to the KPZ scaling [46].

As the parameter increases from $\alpha = 0$ to $\alpha = 5$, the γ values are found to decrease from $\gamma = 1$ to $\gamma \approx 0.55$ (see Fig. 13). This corresponds to slower-than-linear growth of w^2 with $\ln N$. Hence, for large systems w^2 approaches a finite value. Perhaps unexpectedly, for $\alpha < 0$, the exponent γ has also been observed to become smaller than 1. Therefore, we conclude that, in the range of system sizes considered, the scaling properties of the generalized KS equation (69) differs from those of the EW (and KPZ) equation. when $\alpha \neq 0$.

This seemingly different scaling for $\alpha \neq 0$ must be the effect of the finite system size L, since it can be shown using renormalization group (RG) arguments (see, e.g., [51]) that the influence of the nonlinear term $\nabla^2(\nabla h)^2$ has to become irrelevant at asymptotically large scales (when $k \to 0$), and the scaling

for $L \to \infty$ has to be equivalent to the KS $\alpha = 0$ case. However, the present results suggest that this asymptotic regime is far from being reached for the systems in the range of sizes investigated here. The obvious influence of parameter α value on the scaling properties is most likely caused by the underlying change in the small-scale surface patterns (see Fig. 10) that interfere with the slow height variations of universal character. This would suggest that, in some practical cases, *different scaling properties* might be observed from those predicted by the RG arguments, even for relatively large systems.

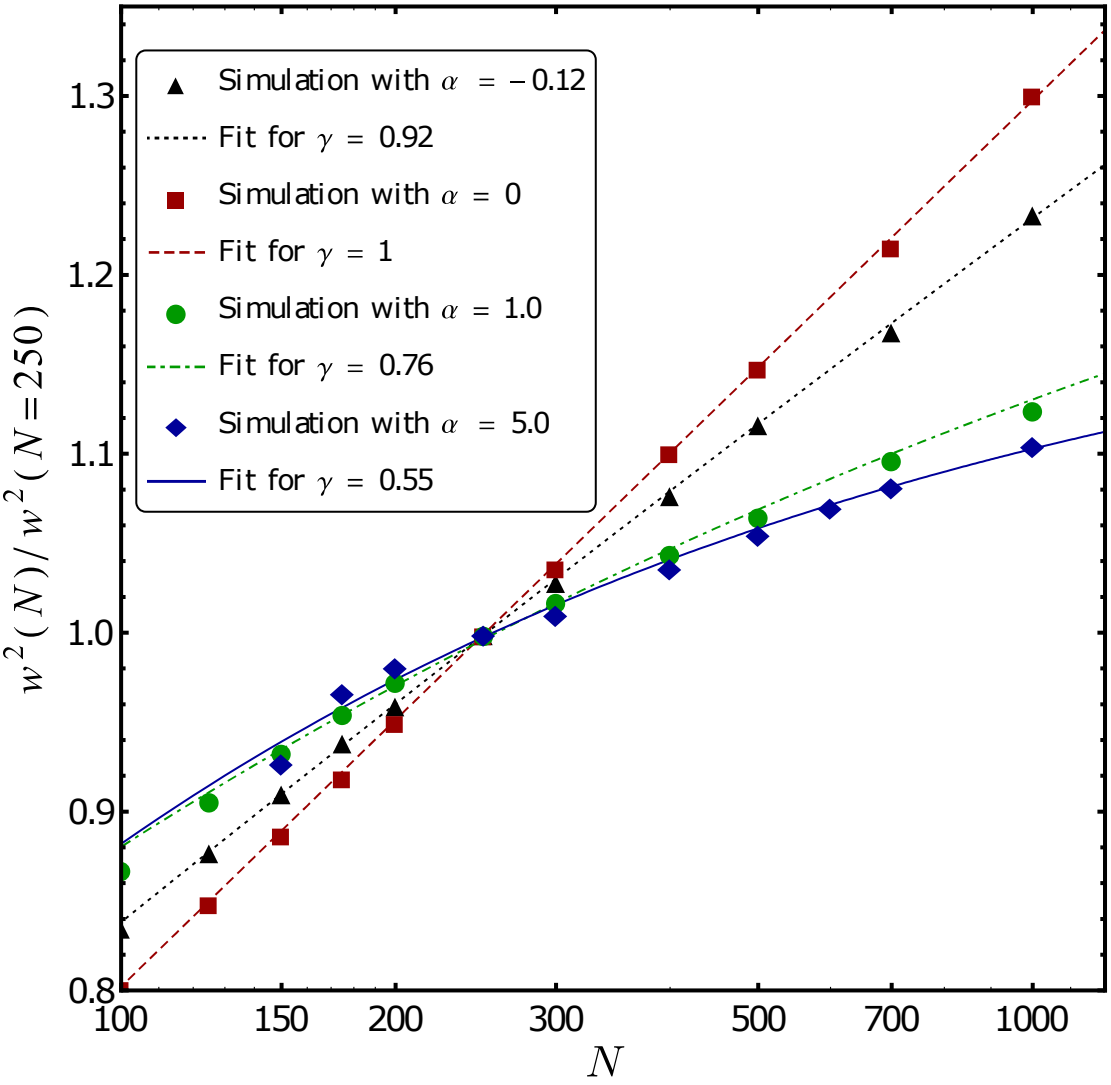

Figure 13: (log-linear scale) Time averaged square of the normalized surface roughness w^2 plotted as a function of the system size N (in lattice units). Symbols: numerical results for surfaces evolving according to (69) with different α values. Lines: fits of the numerical results by (96).

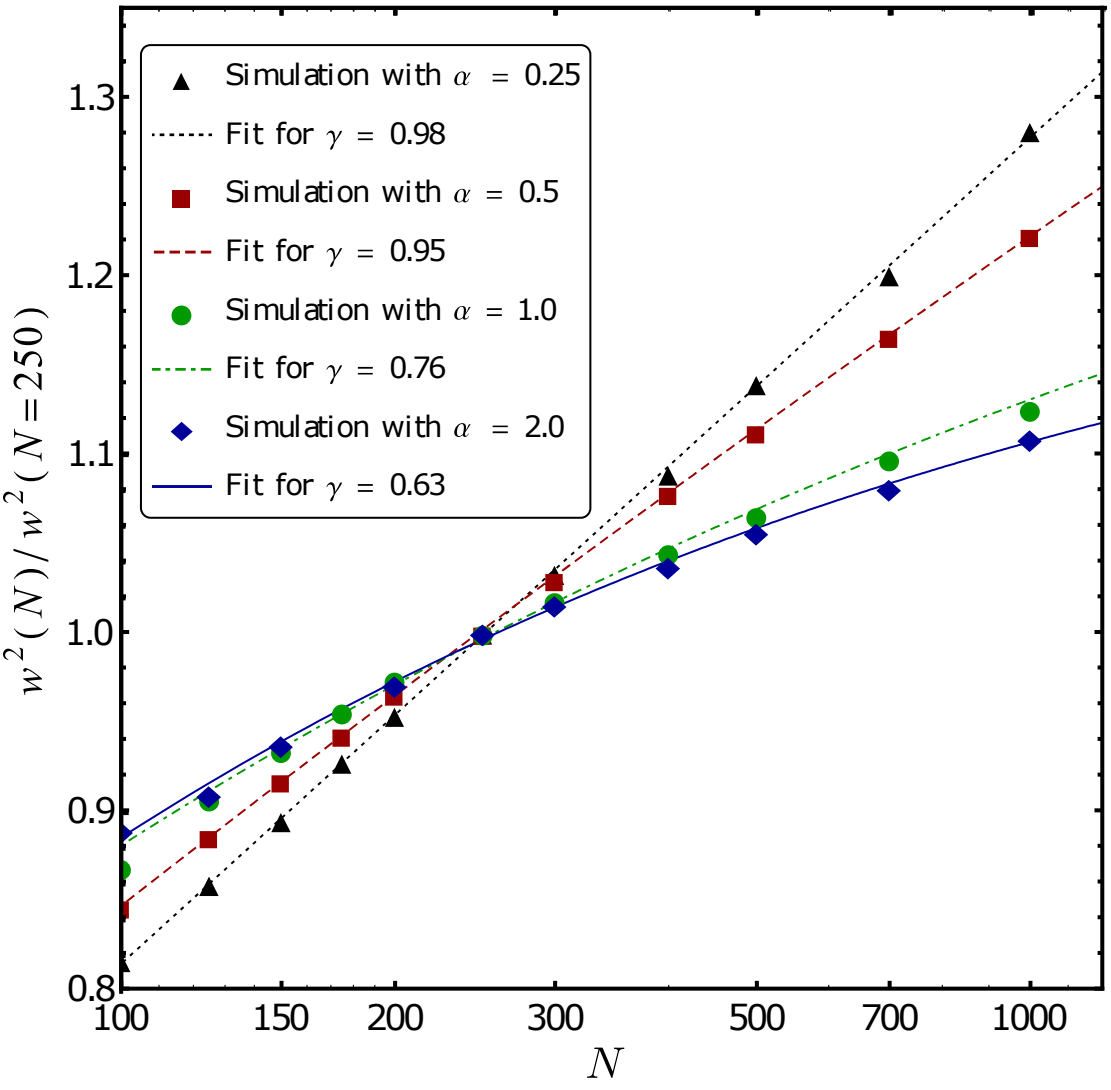

Figure 14: (log-linear scale) Time averaged square of the normalized surface roughness w^2 plotted as a function of the system size N (in lattice units). Symbols: numerical results for surfaces evolving according to (69) with parameter values $\alpha = 0.25,\ 0.5,\ 1,\ 2$. Lines: fits of the numerical results by (96).

5 Small-scale patterns

This section continues the investigation of surface patterns produced by gKS (69),

$$\partial_t h = -\nabla^2 h - \nabla^4 h - \alpha \nabla^2 (\nabla h)^2 + (\nabla h)^2 \,. \tag{98}$$

However, now we focus more on the characterization of the small-scale cellular patterns instead of the long range height variations.

A method for an indirect estimation of a characteristic length scale in disordered surface patterns is presented as a way to estimate the typical size of the surface's structural elements from the global quantities like surface area and surface roughness. In some computational surface growth models that produce cellular patterns, this estimation can be done much faster than any direct calculation from the height height autocorrelation functions or FFT. As a demonstration, this method is then applied to surfaces produced by the generalized Kuramoto-Sivashinsky equation that has been widely used as a model for amorphous solid surface growth.

5.1 Calculation of characteristic length in disordered cellular patterns

As already demonstrated in the previous section (see Fig. 10), the characteristic length R_c in the surface pattern (corresponding to the average diameter of the individual hump) can be defined by the position of the first peak in the height correlation function $C(r)$:

$$R_c = \min\{r > 0 | C'(r) = 0 \;\&\; C''(r) < 0\} \,. \tag{99}$$

However, an alternative way of calculating R_c from the surface spectrum $S(k)$ has proven to give more accurate results. Using this method, the characteristic length is expressed from the wavenumber k_c at which the spectrum has its [most pronounced] peak:

$$R_c = \frac{2\pi}{k_c} \,. \tag{100}$$

Fig. 15 shows examples of such spectra for different parameter values. We

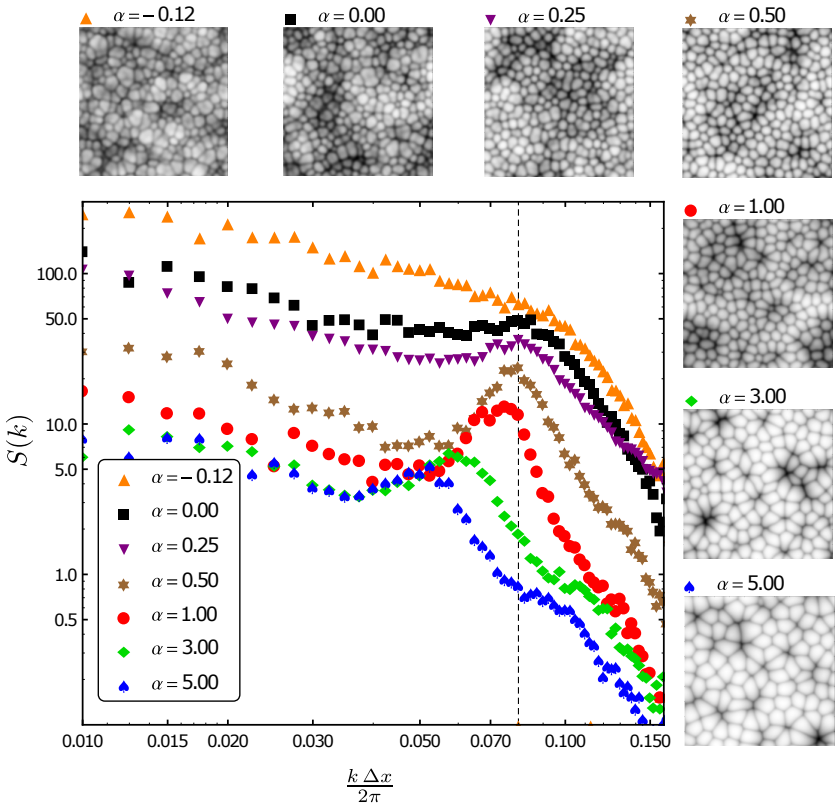

Figure 15: (log-log scale) Surface spectra $S(k)$ at higher wavenumbers calculated from (90) for various parameter values at system size $N = 500$ ($L \approx 355$) and $t = 100000$ (in the saturated regime). The corresponding surface profiles (top row and right column) are from of system size $N = 300$ ($L \approx 213$). The vertical dashed line denotes the wavenumber $k_0 = \frac{1}{\sqrt{2}}$ that is the strongest linearly amplified mode.

can see that the surface spectrum for $\alpha = 0$ has some slight peak where the corresponding autocorrelation function, Fig. 10, has none deeming former to be a better estimator for characteristic lengths. Also, the apparent lack of peak for $\alpha = -0.12$ suggests that no characteristic length can be defined in a sensible way in this case. The trend of increasing characteristic length R_c (shift of the peak in $S(k)$ towards lower wavenumbers) when the parameter α is increased is also clearly visible for $\alpha \geq 0.5$.

In order to observe the influence of parameter α on the small scale structure, the calculations with various parameter values $0 \leq \alpha \leq 5$ on relatively small systems (size $N = 200$ in lattice units) have been performed, so that the long range height variations have little influence on the morphology. For each parameter value, multiple realizations with different initial conditions have been performed and the calculated spectra $S(k)$ of the resulting saturated surfaces have been averaged. Some example spectra are shown in Fig. 19. Then, the

characteristic lengths R_c have been calculated for every parameter value. The same for the surface roughness w and the normalized excess surface area $a-1$, the latter defined in (109) and (114), page 67. The results are shown in Fig. 16.

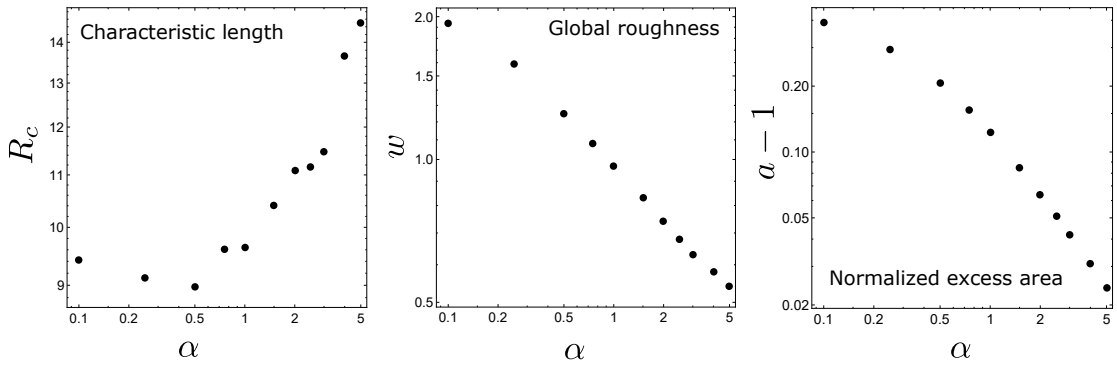

Figure 16: (log-log scale) Quantities characterizing the surfaces at different parameter α values for relatively small system sizes ($N = 200$): characteristic length R_c, surface roughness (width) w, normalized excess area $a - 1$.

It is not easy to make sense of these quantities separately, bet the following subsection shows that they are related in an unexpectedly simple way.

5.2 Indirect estimation of characteristic length

This section has already covered the ways to determine the characteristic length R_c corresponding to the average cell size in disordered cellular surface patterns directly using height-height autocorrelation functions and surface spectra. Nevertheless, the apparent similarity of the shapes of individual humps suggests that relations between the global properties of the surface may offer indirect, but much faster ways of determining the characteristic lengths of the pattern elements (cells/humps) - once some suitable assumptions on their geometrical shape are made.

Ansatz for the surface area of a single element

Despite the lack of any long range order, the cellular surface patterns produced by gKS seem to consist of similar looking individual humps of similar size. This suggests that the statistical properties of the whole cellular pattern might be equivalent to a pattern constructed of identical geometrical elements with averaged properties such as height and diameter. Therefore the following

expression for the surface area of a single surface element (hump) is assumed:

$$A_1 \sim r^2\left(1 + B\left(\frac{h}{r}\right)^{\nu}\right)^{\frac{1}{\nu}}\ , \tag{101}$$

where h is its height above the flat substrate, and r is its radius (if the element is a surface of revolution) or the half length of its base on the substrate. The parameters $B > 0$ and $\nu > 0$ depend on the shape of the surface element.

The relation (101) fits the expressions for the surface areas of some widely encountered geometric figures, as demonstrated in the examples below.

Some examples

The surface area (without the base) cone of radius r and height h

$$A_{\text{cone}} = \pi r\sqrt{r^2 + h^2} = \pi r^2\left(1 + \left(\frac{h}{r}\right)^2\right)^{\frac{1}{2}} \tag{102}$$

which corresponds to (101) with $B = 1$ and $\nu = 2$.

The surface area of a pyramid (again, not counting the area of its base) with the square base of side length l and height h

$$A_{\text{pyramid}} = 2l\sqrt{\left(\frac{l}{2}\right)^2 + h^2} = l^2\left(1 + \left(\frac{2h}{l}\right)^2\right)^{\frac{1}{2}} = 4r^2\left(1 + \left(\frac{h}{r}\right)^2\right)^{\frac{1}{2}} \tag{103}$$

with $l = 2r$ which also corresponds to (101) with $B = 1$ and $\nu = 2$.

As an extreme case (in the sense that it has walls perpendicular to the substrate), the surface area of a cylinder (not counting one of its bases, since it lies on a substrate) is

$$A_{\text{cylinder}} = \pi r(2h + r) = \pi r^2\left(1 + 2\left(\frac{h}{r}\right)\right) \tag{104}$$

which fits (101) as well with $B = 2$ and $\nu = 1$.

A more realistic example (in a sense that it would better represent a round hump) is a surface area of a *half of an ellipsoid of revolution* with radius r and the third axis (height) h whose approximate surface area can be expressed as

$$A_{\text{ellipsoid}} \approx 2\pi\left(\frac{r^{2\nu} + 2(rh)^{\nu}}{3}\right)^{\frac{1}{\nu}} = \frac{2}{3^{1/\nu}}\pi r^2\left(1 + 2\left(\frac{h}{r}\right)^{\nu}\right)^{\frac{1}{\nu}} \tag{105}$$

with $\nu \approx \frac{8}{5}$. This expression also fits (101) with $B = 2$ and $\nu = 1.6$. The latter expression is obtained from the highly referred to in published articles (although itself never published in an article form) and commonly used by internet resources (including Google Calculator, web-formulas.com, Wikipedia and many others) formula proposed by a Danish Geologist Knud Thomsen in an email which can be found online [70]. This formula, known as the Kund Thomsen's formula, expresses the surface area of an ellipsoid

$$\left(\frac{x}{a}\right)^2 + \left(\frac{y}{b}\right)^2 + \left(\frac{z}{c}\right)^2 = 1$$

with its principal semiaxes a, b and c as

$$A \approx 4\pi \left(\frac{(ab)^p + (ac)^p + (bc)^p}{3} \right)^{1/p} \tag{106}$$

where $p = 1.6075$. This formula yields the error at most 1.061%. This formula is preceded by the mathematically rigorous work by Klamkin [71] where he obtains that the surface area is always within the bounds of (106) with $p = 1$ and $p = 2$,

$$4\pi \left(\frac{ab + ac + bc}{3} \right) \leq A \leq 4\pi \left(\frac{(ab)^2 + (ac)^2 + (bc)^2}{3} \right)^{1/2},$$

which suggests that (106) with some $1 \leq p \leq 2$ would likely be a good approximation for the surface area of an ellipsoid.

Surface area of a grid of identical elements

Now, let us consider a flat substrate which is a square of side length L. We construct a surface by packing the substrate with geometrical elements – putting the elements directly next to each other, but with no overlap), see Fig 17. The surface area A_1 of each individual element scales as (101). When the lateral length of the substrate L is much greater than the radius r (or diameter $l \sim 2r$) of the base of the element, the number N of the elements that can fit on the substrate approximately scales as

$$N \sim \frac{L^2}{r^2}, \tag{107}$$

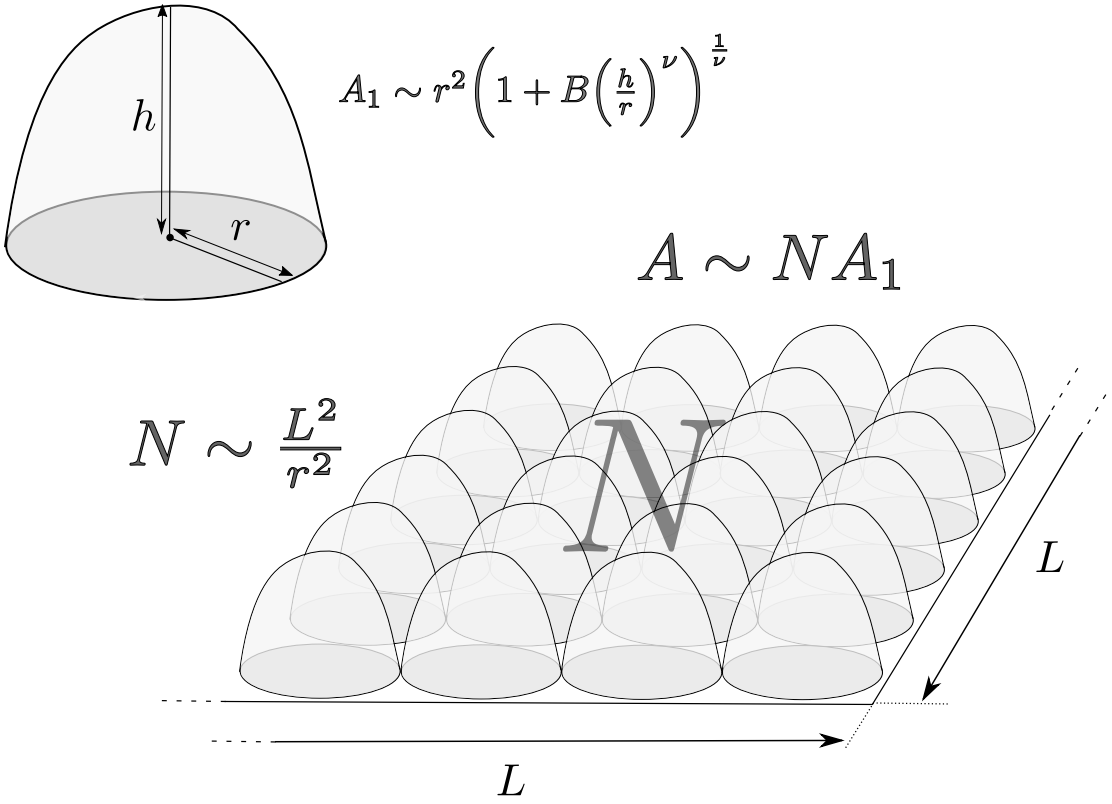

Figure 17: Schematic representation of the scaling argument, see main text. Top left: a single surface element with base radius r and height h and surface area A_1 which scales as (101). Bottom right: the surface of area A constructed by placing N such elements on the flat square of side length L.

and then the area of the whole surface can be given as

$$A \approx NA_1 \sim L^2\left(1 + B\Big(\frac{h}{r}\Big)^{\nu}\right)^{\frac{1}{\nu}}. \tag{108}$$

In order for the argument to stay independent of the lateral system size L the 'normalized' surface area a, that is, the average surface area per unit area of the substrate, is introduced:

$$a := \frac{A}{L^2} = \frac{1}{L^2}\int_0^L\int_0^L \mathrm{d}^2 r\,\sqrt{1+(\nabla h(\boldsymbol{r}))^2} = \Big\langle\sqrt{1+(\nabla h)^2}\Big\rangle_{\boldsymbol{r}}. \tag{109}$$

Substituting (108) into (108) gives

$$a \sim \left(1 + B\Big(\frac{h}{r}\Big)^{\nu}\right)^{\frac{1}{\nu}} \tag{110}$$

which gives the scaling relation for r

$$r \sim \frac{h}{(a^\nu - 1)^{1/\nu}} \tag{111}$$

For relatively smooth surfaces where $(a-1) \ll 1$ (note that $a > 1$ by definition (109)), the expansion to the lowest order in $(a-1)$ provides the approximation

$$a^\nu - 1 \approx \nu(a-1) \tag{112}$$

which, when substituted in (111), results in a simple scaling relation

$$(a-1) \sim \Big(\frac{h}{r}\Big)^{\nu}. \tag{113}$$

Here, the quantity $(a-1)$ can be interpreted as 'normalized excess surface area'. That is, given the area A of the surface above the flat square-shaped (with side length L) substrate of area $A_{\mathrm{substr}} = L^2$, the excess area due to the surface curvature can be defined as the difference $\Delta A = A - A_{\mathrm{substr}} \geq 0$ between these two areas. The average excess area per unit area of the substrate would then result in:

$$\frac{\Delta A}{A_{\mathrm{substr}}} = \frac{\Delta A}{L^2} = \frac{A - L^2}{L^2} = a - 1\,. \tag{114}$$

Connection with disordered cellular patterns

In order to apply the scaling relation to disordered cellular patterns, one needs to replace the constant parameters for height h and lateral size r of the elements in (113) by the corresponding statistical quantities. Since the surface roughness w is, by definition, a measure of height variation in the pattern, it is used instead of the height h. Similarly, r is replaced by the characteristic length R_c. The expression corresponding to (113) then becomes

$$(a-1) \sim \left(\frac{w}{R_c}\right)^{\nu}. \tag{115}$$

Saturated surfaces obtained from the simulations of gKS consist of humps of similar sizes for each parameter value at least in the range $0 \leq \alpha \leq 5$, with different parameter values resulting in different average hump sizes R_c (see Fig. 18) and, simultaneously, in different values for roughness w and normalized area a. If the shapes of individual humps turned out to be geometrically similar, the scaling relation (115) would approximately hold for moderate system sizes at which the long range height variations do not contribute significantly to the total surface roughness w.

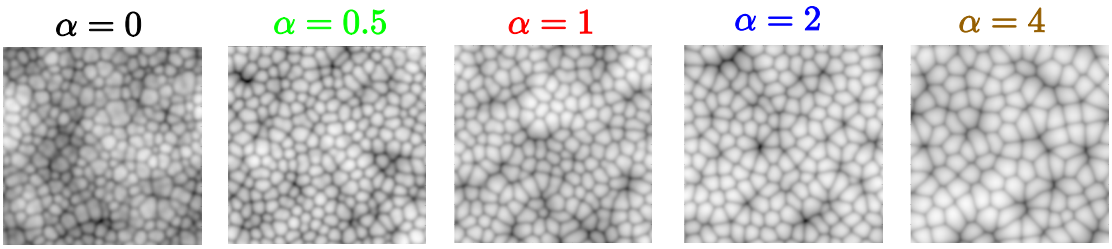

Figure 18: Small-scale cellular surface patterns in saturated surfaces produced by gKS equation for different values of parameter α and system size $L \approx 142$ (or $N = 200$ in lattice units). The corresponding surface spectra are shown in Fig. 19.

In order to test the validity of (115), simulations on gKS with 12 different parameter α values from the range $0 \leq \alpha \leq 5$ have been performed doing 5 realizations for each parameter value. System size L has been chosen relatively small, so that the influence of long range height variations would remain small, but large enough to contain a substantial number of small-scale humps. The resulting surfaces at time $t = 10^5$ (when the saturation has certainly been reached). The roughnesses w, the normalized areas a and the spatial spectra $S(k)$ have been evaluated for all these surfaces and then averaged over all real-

izations for every parameter α value used. Examples of the resulting spectra for several parameter values are shown in Fig. 19. The positions of the peaks in the spectra have then been determined by fitting parabolas around the peaks (dotted lines in Fig. 19). The characteristic length of the pattern R_c for each case has then been evaluated from the wave number k_c at which the corresponding spectrum has a peak:

$$R_c = \frac{2\pi}{k_c} \,. \tag{116}$$

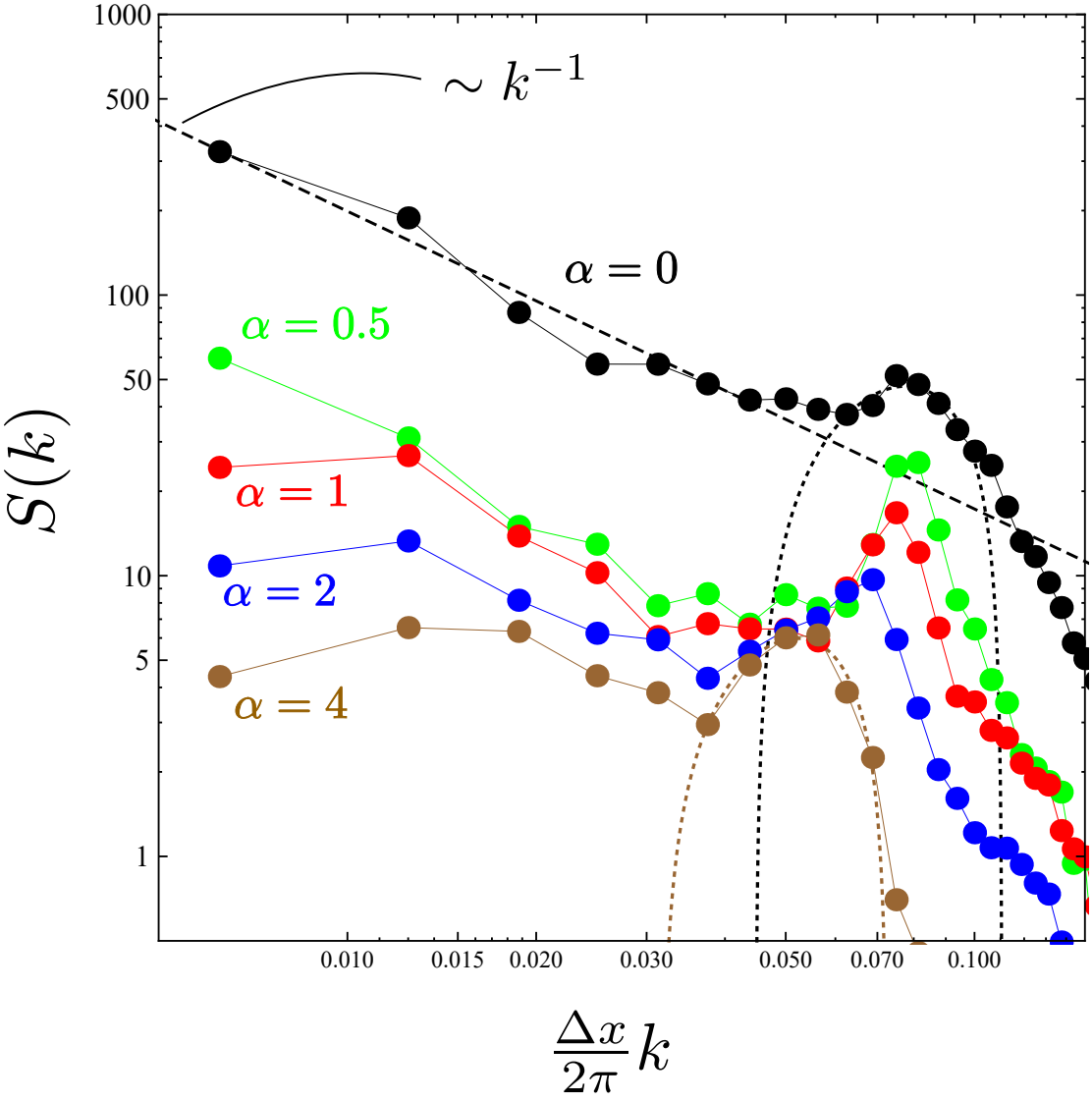

Figure 19: (log-log scale) Surface spectra and parabolic fits (dotted lines) around the peaks for the determination of the characteristic length R_c for several parameter α values. The dashed line corresponds to the power-law fit $S(k) \sim k^{-1}$ at small wave numbers when $\alpha = 0$ (see Fig. 12 in Sect. 4). Examples of the corresponding surface profiles are shown in Fig. 18.

These results, when plotted in a double logarithmic (log-log) plot as $(a-1)$

vs w/R_c (black dots in Fig. 20) form a straight line suggesting that the power-law expressed in (115) holds. In fact, the expression

$$a - 1 = B\left(\frac{w}{R_c}\right)^{\nu} \tag{117}$$

plotted as the red line in Fig. 20 seems to fit the directly calculated results extremely well with $B \approx 5.04$ and $\nu \approx 1.61$.

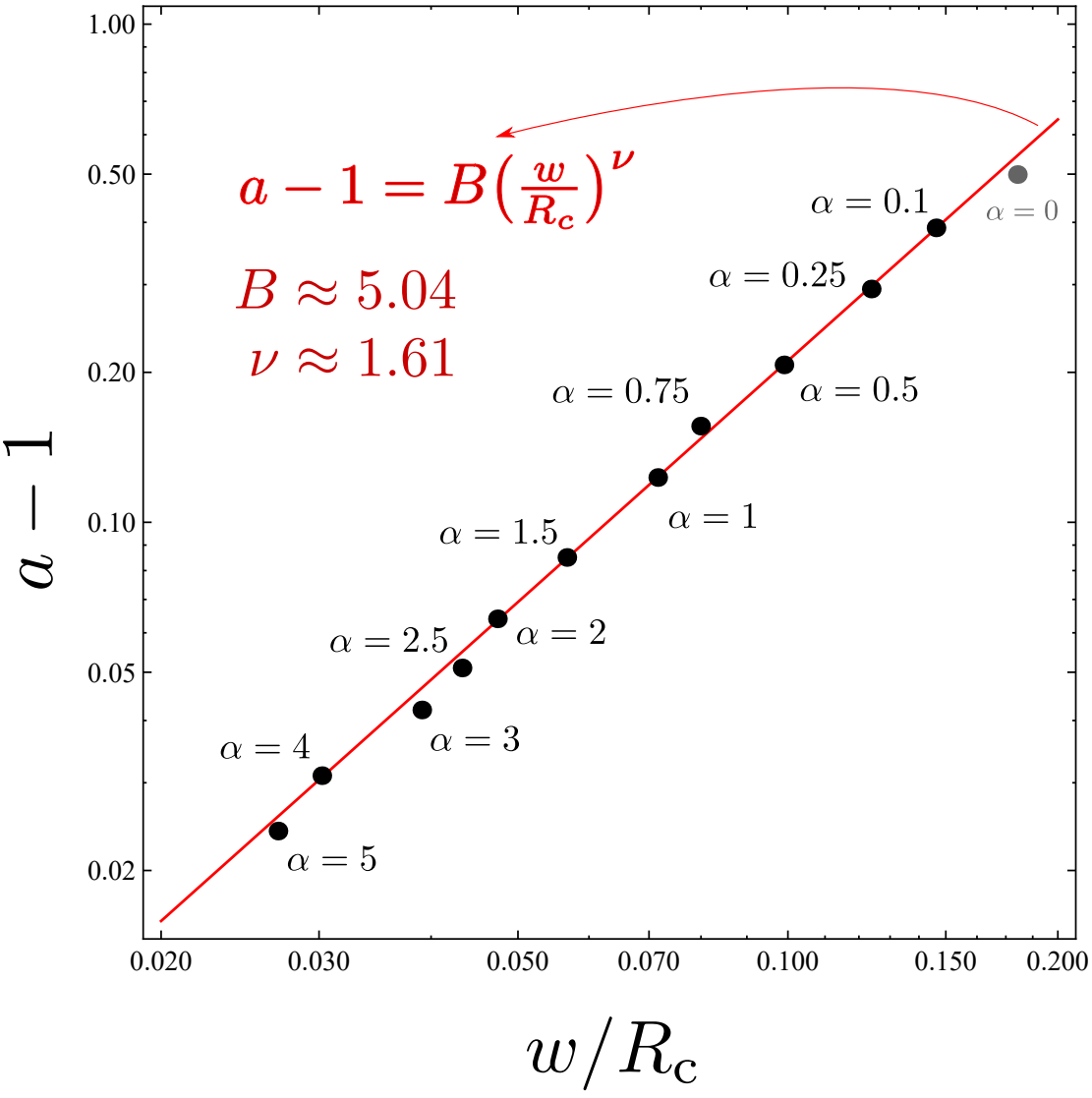

Figure 20: (log-log scale) Relation $(a - 1)$ vs w/R_c. Black circles: directly calculated values from numerical simulations. Red line: fit using scaling relation (113).

Some conclusions

The fact that the scaling relation (115) holds for the disordered surface patterns obtained from the gKS in a range of parameter values indicates that the individual humps, although differing in size, nevertheless retain geometrically similar shape on average when the parameter is varied.

Another and, perhaps, an even more surprising observation is that the exponent $\nu \approx 1.61$ obtained by fitting (115) to the directly calculated results lies within 0.16% from the value $\nu \approx 1.6075$ suggesting that the average properties of gKS surfaces scale in alomost the same way as if they were constructed from many identical humps shaped like halves of ellipsoids of revolution.

The validity of (117) allows one to estimate R_c as

$$R_c \approx B^{1/\nu} \frac{w}{(a-1)^{1/\nu}} \tag{118}$$

from the values w and a, which – at least in numerical simulations – can be evaluated much faster than the height autocorrelation functions $C(r)$ or spatial spectra $S(k)$ needed for the direct calculation of R_c.

The arguments presented in this subsection may perhaps be applied for other models producing disordered cellular patterns.

6 Analysis of roughness dynamics in the Kuramoto-Sivashinsky case

Model equation (1) produces disordered spatial patterns that evolve in time. As shown in Sect. 4, with an increase of the system size L new long range height variations appear in the resulting surface profiles in addition to the small scale patterns. The apparent scale-free character of these slow height variations is very different from the cellular patterns on small scales which have a characteristic length (the average size of a 'cell' or 'hump'). Also, the spatial properties of both, the small scale patterns and the large scale height variations, depend strongly on the value of parameter α in (1). This section investigates the corresponding dynamics of these surfaces.

In order to understand the complex spatio-temporal behaviour of (1), we investigate the dynamics of surfaces it produces by analysing the numerically obtained time series of the surface roughness $w(t)$ which contains the collective behaviour of all modes. The time series of $w(t)$ are investigated in the time interval $t \in [2 \cdot 10^4, 10^5)$ with sampling time $\tau_{\text{sample}} = 1$ (i.e., sampled every 200 time steps $\Delta t = 0.005$), that is, $8 \cdot 10^4$ values in total for every realization. The results are averaged over 5 to 10 realizations (differing in the initial surface profile) for every parameter α value. For the range of parameter values explored here, the surface evolution can be considered stationary and ergodic, since the statistical properties of $w(t)$ (average, standard deviation, skewness, autocorrelation function) seem to vary little from realization to realization. Moreover, their values calculated in large enough subintervals of the total time interval differ only slightly from each other.

In this section, the analysis of $w(t)$ is presented in more detail for parameter value $\alpha = 0$, that is, the Kuramoto-Sivashinsky case (2). The same analysis performed on other parameter values is discussed in Sect. 7.

6.1 Occurrence of slow modes

Fig. 21 shows a representative sample of a surface roughness $w(t)$ time series for $\alpha = 0$ and system sizes varying from $N = 125$ to $N = 1000$. Even

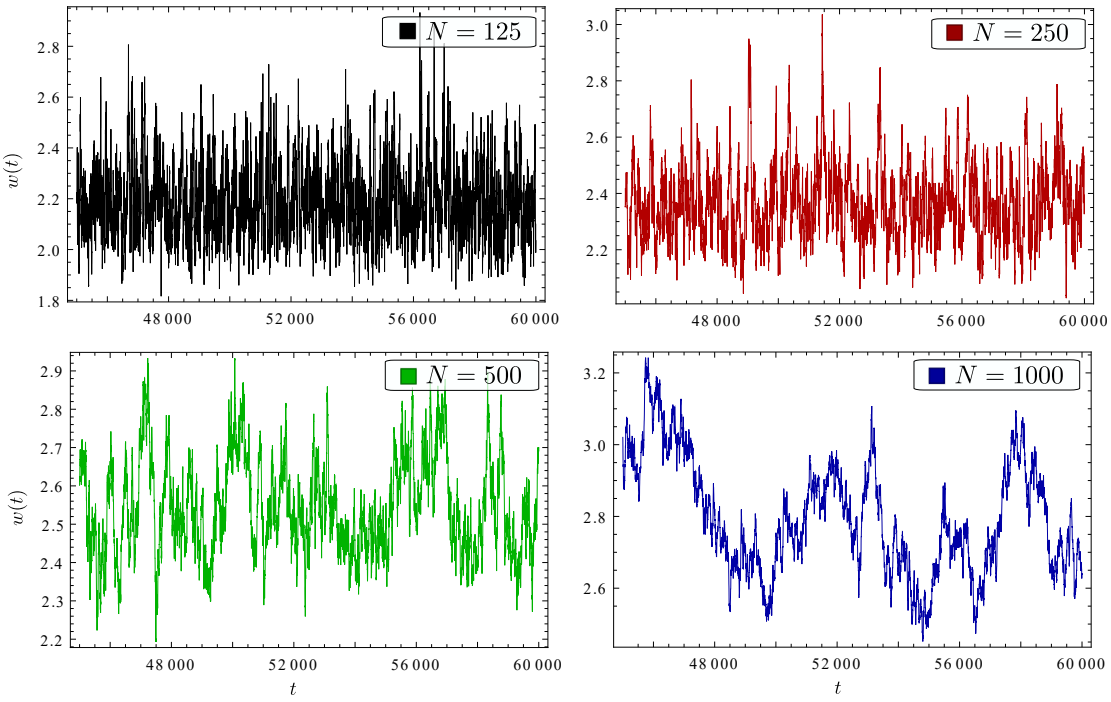

Figure 21: Time series of the surface roughness $w(t)$, $t \in [4.5 \cdot 10^4, 6 \cdot 10^4)$ for $\alpha = 0$ and different system sizes N (in lattice units).

though the roughness dynamics is dominated by white noise for small systems ($N = 125$), additional slow modes appear as the system size is increased. For relatively large systems ($N = 1000$), the time series in question is similar to a signal produced by a random walk.

This transition can be visualized even more clearly by using the recurrence plot technique [72–75] (see Fig. 22). There, a time series $s(t)$ is depicted by plotting a matrix $\boldsymbol{R}_{t_i,t_j}$. In the plot, the axes represent the discrete time t_i and t_j. A black dot ($\boldsymbol{R}_{t_i,t_j} = 1$) is put at a point (t_i, t_j) if the values of the time series $s(t)$ at these times coincide (recur) to a given accuracy ϵ. The pixel remains white otherwise (value $\boldsymbol{R}_{t_i,t_j} = 0$), that is:

$$\boldsymbol{R}_{t_i,t_j} = \Theta(\epsilon - |s(t_i) - s(t_j)|)\,, \tag{119}$$

where $\Theta(x)$ is the Heaviside step function. Each of the recurrence plots in Fig. 22 is made for a single realization of $w(t)$ in the time interval $t \in [8 \cdot 10^4, 10^5)$, i.e., one fourth of the total length of the time series is investigated.

The slow fluctuations of $w(t)$ that appear when the system size is increased can be attributed to the low wave number spatial modes that occur in larger systems. By investigating the scaling properties of these fluctuations, connections

between spatial and temporal properties of the corresponding large scale height variations can be made.

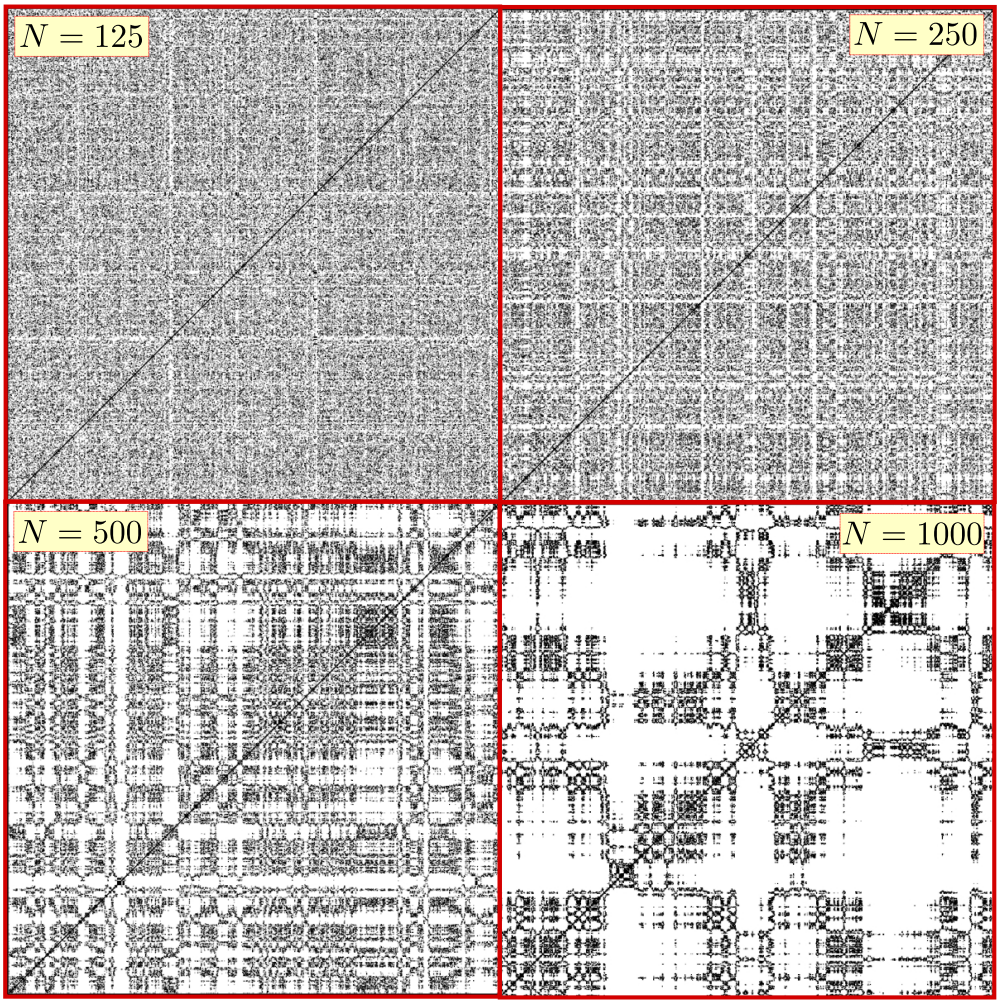

Figure 22: Recurrence plots of the one-dimensional time series of the surface roughness $w(t)$ for $t \in [8 \cdot 10^4, 10^5)$, $\alpha = 0$, and different system sizes N (in lattice units). Here $\epsilon = 0.002\,\sigma$, where σ is the standard deviation from the average of the corresponding time series for each N.

6.2 Autocorrelation functions

The character of the slow fluctuations that appear in the time series (TS) of the surface roughness $w(t)$ resulting from (1) for large systems (see Figs. 21 and 22) is captured by their autocorrelation functions,

$$A(\tau) = \big\langle (w(t) - \bar{w})(w(t+\tau) - \bar{w}) \big\rangle_t \,, \tag{120}$$

where $\bar{w} = \langle w(t) \rangle_t$ is the average value of $w(t)$ in the stationary regime. Fig. 23 shows the autocorrelation functions obtained from TS of $w(t)$ with $\alpha = 0$ for four different system sizes increasing by the factor of 2: $N = 125, 250, 500, 1000$. In the top panel of Fig. 23, the normalized (i.e., divided by the variance $\sigma_w^2 = \langle (w(t) - \bar{w})^2 \rangle_t \equiv A(0)$) autocorrelation functions are displayed in the log-linear scale. In this plot, one can immediately recognize the way in which the characteristic time scales in $w(t)$ grow with N. For instance, by defining some characteristic correlation time τ_{corr} as, for example, the lag τ at which the autocorrelation function decays to the 10% (dashed horizontal line) of its initial value at $\tau = 0$, i.e.,

$$\tau_{\mathrm{corr}} = \min\{\tau > 0 \,|\, A(\tau)/\sigma_w^2 \leq 0.1\}\,, \tag{121}$$

one can see that it increases by about the same factor (corresponding to almost constant shifts along a logarithmic scale of τ axis) as the system size N increases by a factor of 2. This indicates that the characteristic time τ_{corr} grows as a power law of N:

$$\tau_{\mathrm{corr}} \propto N^{\xi}\,. \tag{122}$$

Further insight into the dynamics can be gained by looking at the same autocorrelation functions in a semi-logarithmic plot, as displayed on the bottom panel of Fig. 23. Plotted this way, the autocorrelation functions $A(\tau)$ appear almost as straight lines (with an additional kink at very small τ) indicating that the their shape should be approximately exponential:

$$A(\tau) \approx \sigma_w^2\, \mathrm{e}^{-\lambda|\tau|}\,. \tag{123}$$

6.3 Power spectra and characteristic frequencies

In order to obtain more quantitative results, it is essential to look at the shape of the corresponding power spectra of $w(t)$. As stated by the Wiener-Khinchin theorem [76], the power spectral density (PSD) $W(f)$ of a signal can be obtained by Fourier transforming its autocorrelation function (120):

$$W(f) = \int_{-\infty}^{\infty} \mathrm{d}\tau\, A(\tau)\, \mathrm{e}^{-\mathrm{i}2\pi f \tau}\,. \tag{124}$$

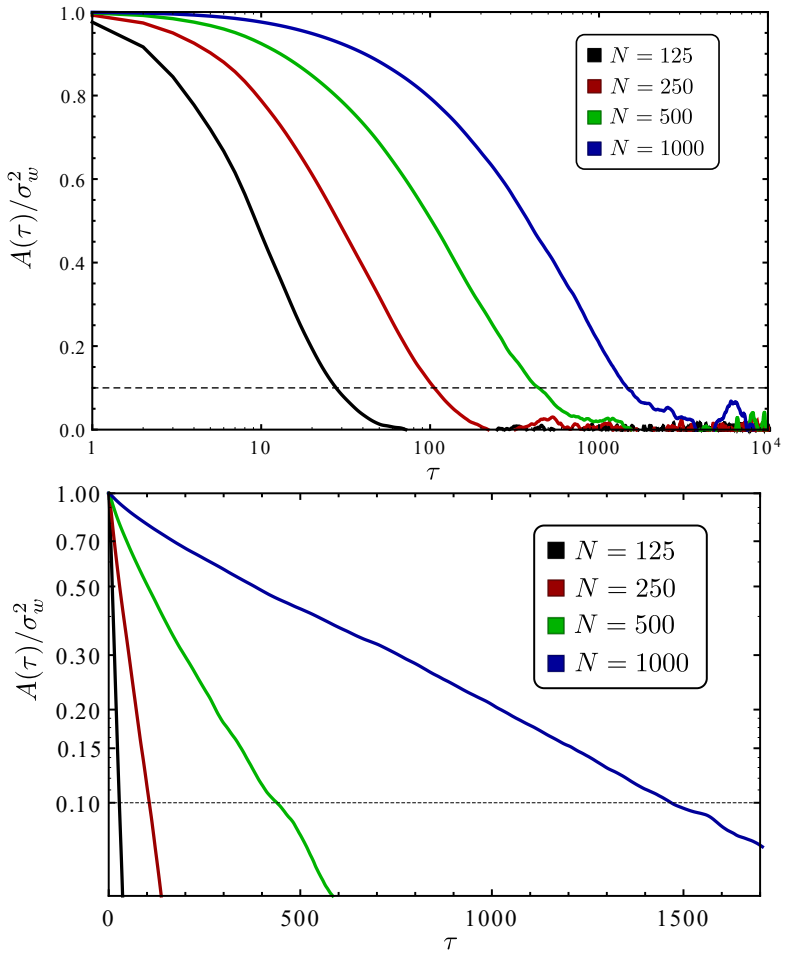

Figure 23: Normalized autocorrelation functions $A(\tau)$ of the surface roughness $w(t)$, $t \in [2 \cdot 10^4, 10^5)$ for $\alpha = 0$ and different system sizes (in lattice units) N. Top panel: log-linear scale. Bottom panel: semi-logarithmic scale. Horizontal dashed and dotted lines in both panels represent the $A(\tau)/\sigma_w^2 = 0.1$.

By substituting the exponentially decaying autocorrelation function $A(\tau) \propto \mathrm{e}^{-\lambda|\tau|}$ (as in (123)) into (124), the PSD $W(f)$ of a Lorentzian shape is obtained:

$$W(f) \propto \frac{f_0}{f_0^2 + f^2}\,, \tag{125}$$

where $f_0 = \lambda/2\pi$ is the characteristic frequency that signifies the cross-over between different behaviours of $W(f)$, namely:

$$W(f) \sim \begin{cases} \text{const} & , \quad f \ll f_0 \\ f^{-2} & , \quad f \gg f_0\,. \end{cases} \tag{126}$$

Thus, f_0 represents the lowest frequency (or the lowest decay rate $\lambda \propto f_0$) that affects the dynamics of $w(t)$. The above considerations suggest that f_0 must

correspond to the lowest wave number, $k_{\min} \propto L^{-1}$, of a spatial mode occurring in the system of size L.

Plotted in semi-logarithmic scale (bottom panel of Fig. 23), the autocorrelation functions $A(\tau)$ appear as almost straight lines corresponding to the approximate exponential decay (123) whose PSD is a Lorentzian (125). Nevertheless, there are deviations from this trend at very short lag times τ. These deviations correspond to additional fluctuations with a very short correlation time – a *white noise* whose PSD is a constant. Therefore, the resulting PSD of $w(t)$ can be fitted by a Lorentzian plus a constant:

$$W_{\text{fit}}(f) = \frac{A}{f_0^2 + f^2} + B \tag{127}$$

where A, B and f_0 are fit parameters.

The PSDs obtained from the autocorrelation functions of the surface roughness at $\alpha = 0$ for different system sizes $N = L/\Delta x$ are shown in the top panel of Fig. 24 together with their fits by (127). A closer analysis shows that a function with a generalized Lorentzian plus a constant B,

$$W_{\text{fit}}(f) = \frac{A}{(f_0^2 + f^2)^{\beta/2}} + B\,, \tag{128}$$

with $\beta = 1.8$ fits the calculated PSDs even better, see the bottom panel of Fig. 24. Note that β is *not* the growth critical exponent, as opposed to the usual kinetic roughening nomenclature [51].

The cross-over frequency f_0 obtained as a fit parameter represents the lowest frequency (corresponding to the longest time scale) in the kinetics of $w(t)$. In Fig. 24, it is clearly visible that f_0 decreases as the system size N is increased. Since the lowest wave number $k_{\min}$ of the spatial modes occurring in the system is inversely proportional to the system size, $k_{\min} \propto N^{-1}$, the $f_0(N)$ dependence connects the spatial and the temporal scales. Indeed, by defining the some critical wave number k_0 as

$$k_0 = \frac{2\pi}{L} \equiv \frac{2\pi}{\Delta x}\,\frac{1}{N} \propto k_{\min}\,, \tag{129}$$

one can obtain a dispersion relation $f_0(k_0)$ — a connection between the lowest wave number in the system and its corresponding frequency. The resulting f_0

dependence on $k_0 \Delta x/(2\pi) = N^{-1}$ for $\alpha = 0$ is shown in Fig. 25 in the double-logarithmic scale. Plotted this way, the results appear to lie on a straight line, meaning that the relation is approximately a power-law $f_0 \propto k_0^{\xi}$ with the exponent $\xi \approx 1.89$, as the fit shows (c.f. Fig. 25).

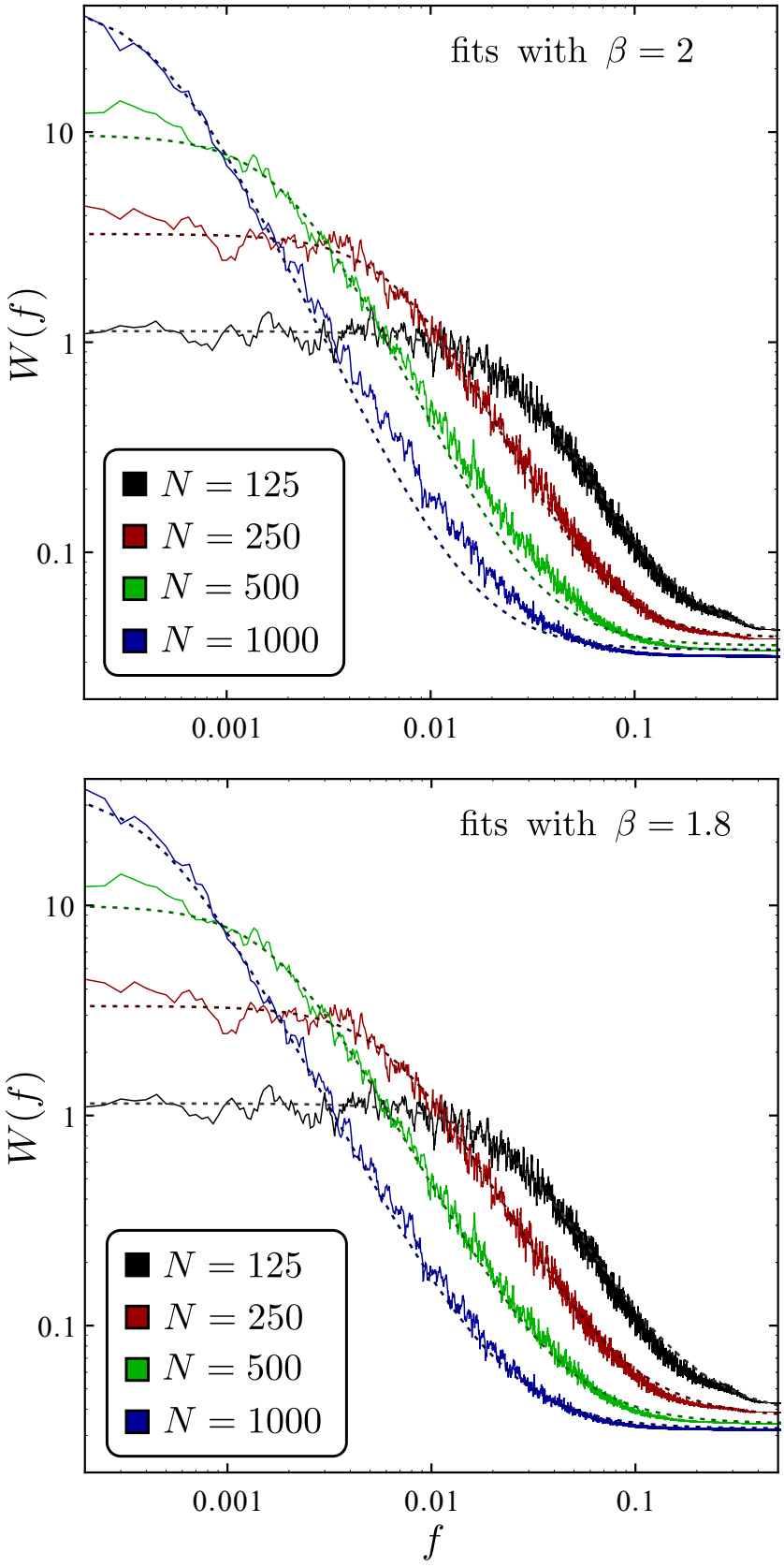

Figure 24: The power spectral densities $W(f)$ of the surface roughness $w(t)$ for $t \in [2 \cdot 10^4, 10^5)$, $\alpha = 0$, and different system sizes N. Solid lines: calculation results of (124) with (120). Dotted lines: fits of the calculated results by (128) with $\beta = 2$ (top panel) and $\beta = 1.8$ (bottom panel).

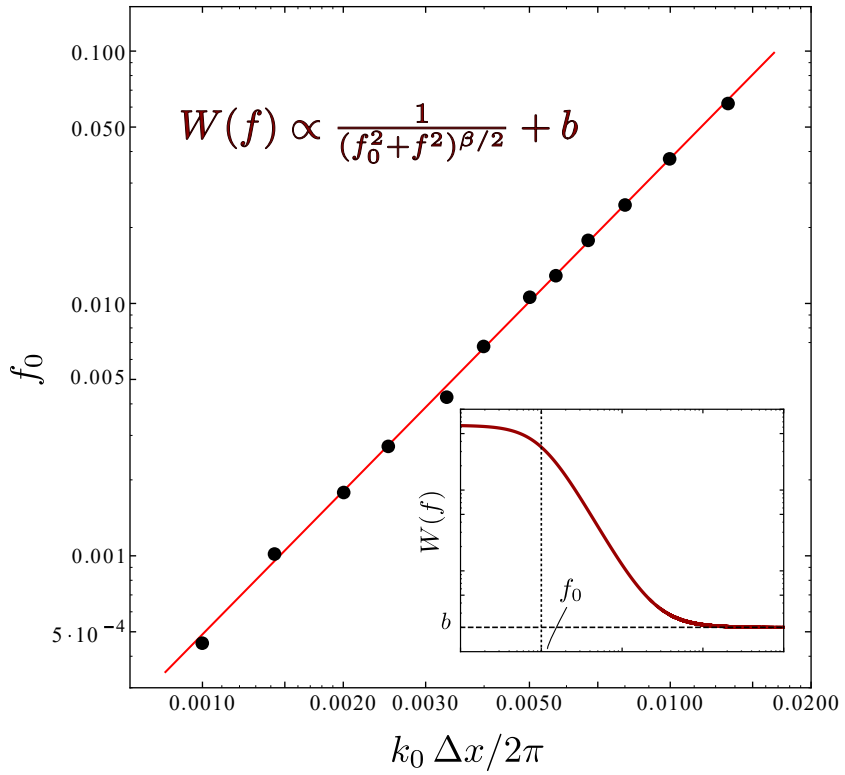

Figure 25: (log-log scale) Relation between the lowest frequency f_0 and the lowest wave number k_0 occurring in the system for $\alpha = 0$. The black filled circles are f_0 values obtained as fit parameters for numerical results by (128). The solid red line is the power-law fit $f_0 \propto k_0^{\xi}$ with $\xi \approx 1.89$. The inset on the bottom right shows f_0 for the PSD $W(f)$ defined by the expression shown on the top left.

7 Dynamics of roughness in the generalized case

The fluctuations of $w(t)$ change character as parameter α is varied. This can already be seen from their time series (Fig. 26). This section presents some of the results on spatio-temporal properties of surfaces evolving according to (1) with parameter values $\alpha \neq 0$ in order to point out the similarities and differences from the $\alpha = 0$ case presented in Sec. 6.

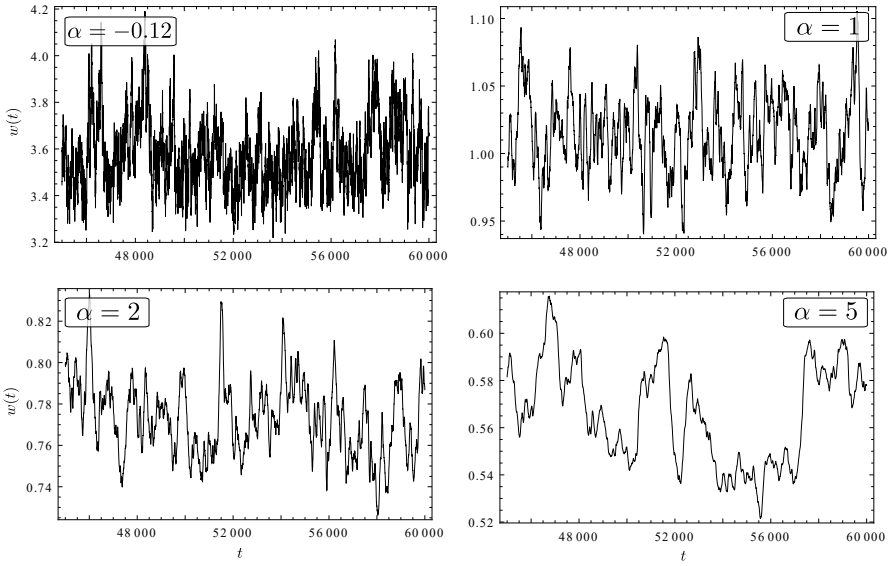

Figure 26: Time series of the surface roughness $w(t)$ for $t \in [4.5 \cdot 10^4, 6 \cdot 10^4)$, system size $N = 500$ (in lattice units), and different values of parameter α.

7.1 Spatio-temporal properties

The same type of analysis, as presented in Sec. 6 for parameter $\alpha = 0$, has also been performed for other parameter values.

As in the $\alpha = 0$ case, for $\alpha \neq 0$, the occurrence of slow modes can also be observed as the system size increases. However, since the character of low wave number spatial variations depends on α, as shown in Sec. 4, their temporal properties also differ.

The PSDs of $w(t)$ for $-0.12 \leq \alpha \leq 5$ can be fitted very well (see Fig. 30) by a generalized Lorentzian with an added constant (128) at different system sizes N (except for some cases discussed in the following subsection). The exponent

β in the fit (128) increases monotonically from $\beta \approx 1.7$ for $\alpha = -0.12$ to $\beta \approx 3$ for $\alpha = 5$. From these fits at different system sizes N, the relations between the lowest frequencies f_0 in the dynamics and lowest wave numbers of spatial variations $k_0 \propto N^{-1}$ are obtained (Fig. 27), as is done in Sec. 6 for $\alpha = 0$.

Fig. 27 reveals how the spatio-temporal behaviour of evolving surfaces depend on parameter α.

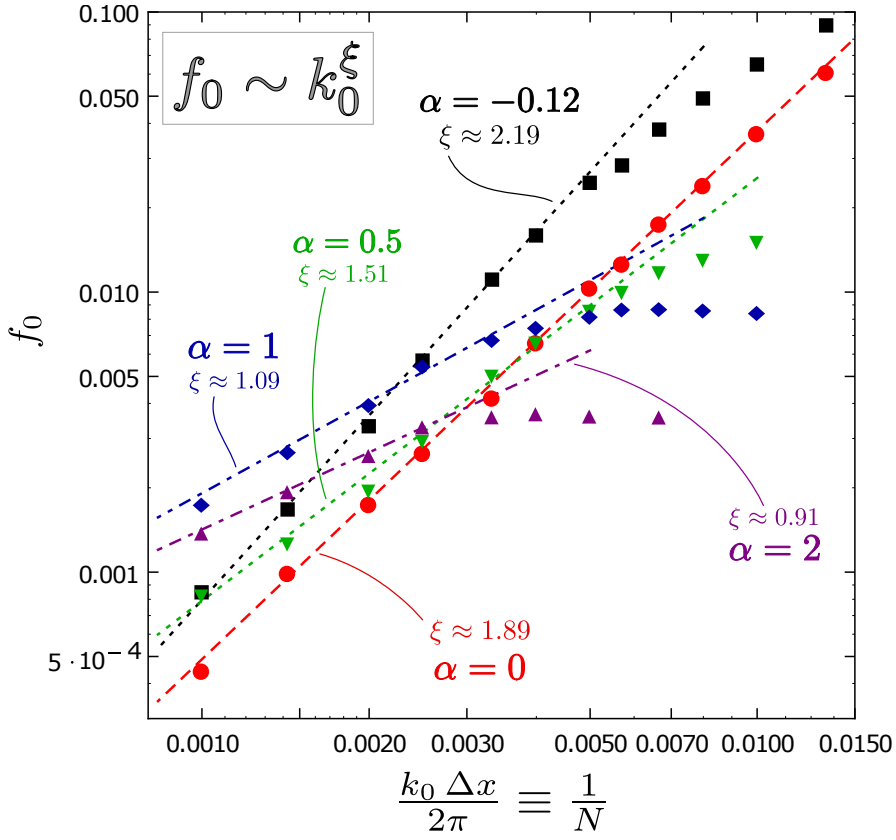

Figure 27: (log-log scale) The lowest frequency f_0 dependence on the lowest wave number k_0 in the dynamics of the surface roughness $w(t)$ for several parameter α values. Symbols: calculated values. Lines: power-law fits (with exponent ξ) of the results for small k_0.

The relations $f_0(k_0)$ shown in Fig. 27 indicate that for small k_0, the power-law behaviour $f_0 \sim k_0^{\xi}$ observed in Fig. 25 for $\alpha = 0$, also persists for $\alpha \neq 0$ with exponent ξ decreasing with increasing α: from $\xi \approx 2.2$ for $\alpha = -0.12$ to $\xi \approx 0.9$ for $\alpha = 2$. This power-law trend can be attributed to the dynamics of scale-free height variations, and the change of the exponent ξ with α can most likely be related to the corresponding change of the surface scaling properties (Sect. 4).

However, for $\alpha \neq 0$, this power-law behaviour flattens out at larger values of k_0 corresponding to small scales. This cut-off of the power-law trend is most

likely due to the coarser small-scale patterns produced by larger values of α (see Fig. 10) whose slower dynamics begins to overshadow, at smaller scales, the dynamics of scale-free height variations corresponding to the power-law trend.

For $\alpha = 5$ (not shown in Fig. 27), the possible power-law behaviour is more difficult to determine, since the curve $f_0(k_0)$ appears flat almost through the whole range of k_0, except for only two points with smallest k_0 — way less than enough to make conclusions.

One can interpret f_0 at some $k_0/2\pi = l_0^{-1}$ as the approximate rate of processes at the length scale l_0, or $n_0 \equiv l_0/\Delta x$ in lattice units. Then the results displayed in Fig. 27 imply that at smaller scales — say, $n_0 < 200$ ($k_0\Delta x/2\pi > 0.005$ in Fig. 27) — the rate is monotonically decreasing with α. On the other hand, for larger scales, this does not hold any more. For example, for $\alpha = 0,\, 0.5,\, 1$ the relation of between f_0 and α reverses (becomes monotonically increasing) already at $n_0 > 300$. For large enough scales, f_0 should become monotonically increasing with α for all values, at least in $-0.12 \leq \alpha \leq 2$, if the power-law trends $f_0(k_0) \propto k_0^{\xi}$ shown as straight lines in Fig. 27 continue for even larger systems, $N > 1000$.

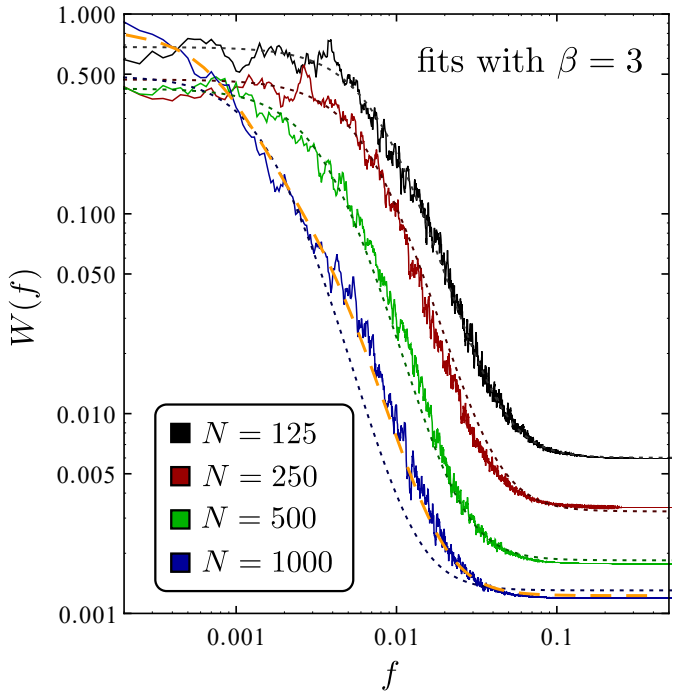

Figure 28: The PSDs $W(f)$ of $w(t)$ from $t \in [2 \cdot 10^4, 10^5)$ for $\alpha = 1$ and different system sizes. Solid lines: the calculated PSDs. Dotted lines: single-generalized-Lorentzian (128) fits with exponent $\beta = 3$. Long-dashed orange line: fit of the PSD at $N = 1000$ by two generalized Lorentzians (130) with the same exponent $\beta = 3$.

7.2 Fits by two generalized Lorentzians

The fits of the PSDs $W(f)$ by a generalized Lorentzian plus a constant (128) seem to be suitable for most cases investigated for $-0.12 \leq \alpha \leq 5$ with system sizes $100 \leq N \leq 1000$. However, for $\alpha = 0.5$ and $\alpha = 1$, and system sizes $N \geq 700$, some larger deviations from the fits can be observed. For example, Fig. 28 displays the apparent occurrence of a second hump in the PSD for $\alpha = 1$ at $N = 1000$ which renders the fit (128) less suitable, although at smaller N it works very well (dotted lines in Fig. 28). In these cases, however, the sum of two generalized Lorentzians and a constant with the same exponent β,

$$W_{\text{fit}}(f) = \frac{A_1}{(f_{01}^2 + f^2)^{\beta/2}} + \frac{A_2}{(f_{02}^2 + f^2)^{\beta/2}} + B\,, \tag{130}$$

fits the PSD almost perfectly (orange long-dashed line in Fig. 28 and red dashed line in Fig. 29).

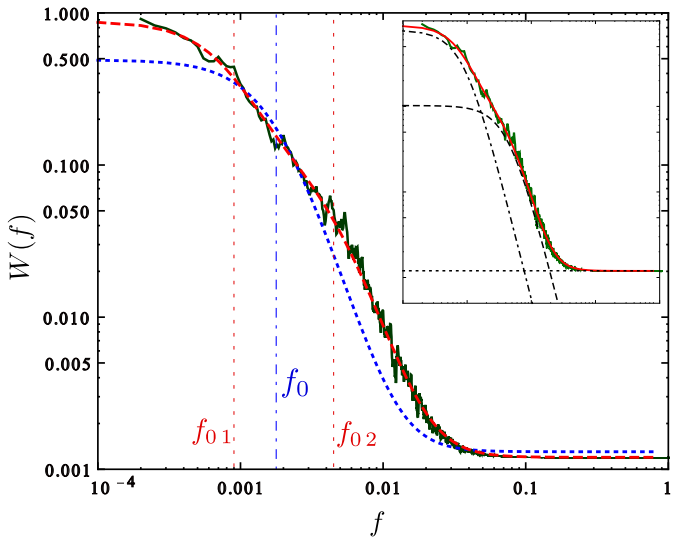

Figure 29: (Log-log scale) The PSD of the surface roughness $w(t)$ for $\alpha = 1$ and $N = 1000$ (solid dark green line) with fits by a single generalized Lorentzian (128) (dotted blue line) and by a two-generalized-Lorentzian fit (130) (dashed red line), c.f. Fig. 28. The vertical straight lines indicate the characteristic frequencies f_0, f_{01} and f_{02} of the fits. The inset shows the fit (130) decomposed into two Lorentzians and a constant.

As can be seen in Fig. 29, the characteristic frequencies f_{01} and f_{02} of the two-generalized-Lorentzian fit (130) have the frequency f_0 of the original single-generalized-Lorentzian fit (128) between them, i.e., $f_{01} < f_0 < f_{02}$. Moreover, the frequency f_0 seems to follow the power-law trend (blue diamonds and dash-

dotted line in Fig. 27), even if the fit is not that good as for smaller N values.

Fig. 30 displays the PSDs with their fits (128) and (130) for the whole parameter α range investigated at system size $N = 1000$.

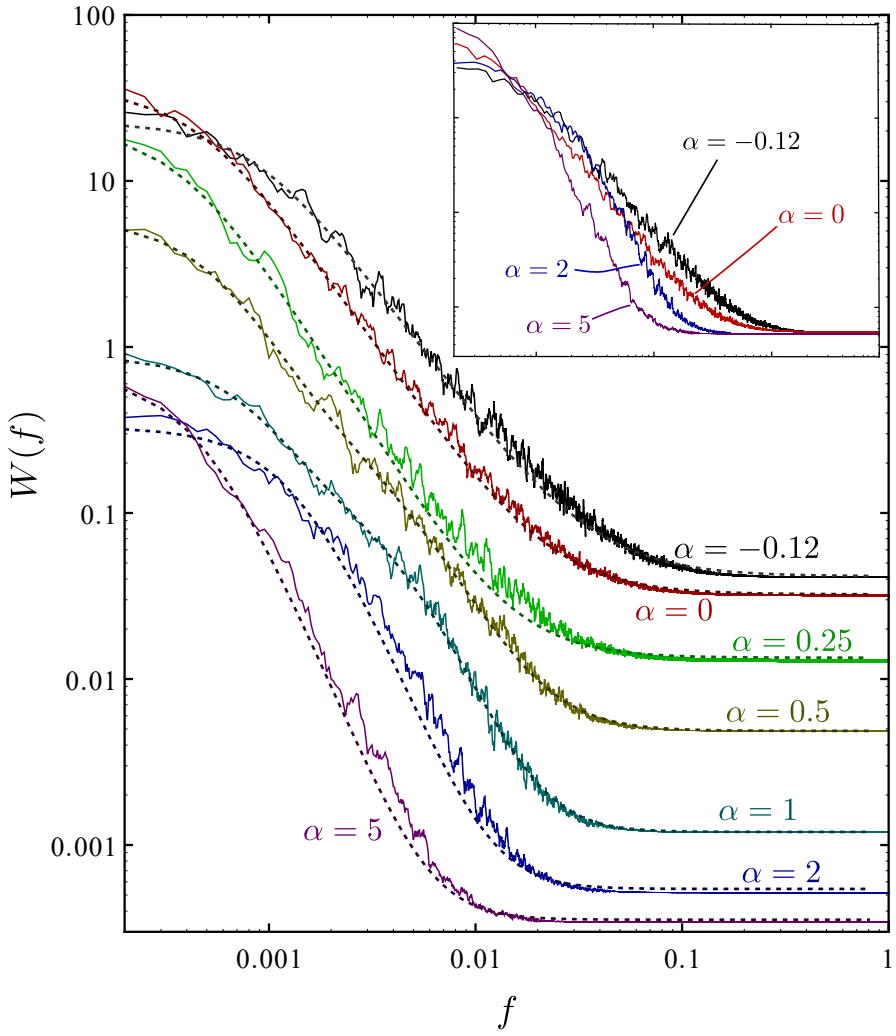

Figure 30: Power-spectral densities (solid lines) of the surface roughness $w(t)$ for a system size $N = 1000$ and different values of α with their fits (dotted lines): a two-generalized-Lorentzian fit (130) for $\alpha = 0.5$ and $\alpha = 1$, and a single generalized Lorentzian fit (128) for all other values. The inset shows some of the same PSDs normalized.

7.3 Some conclusions

The results presented in this section give some new insights into the complex spatio-temporal behaviour of surfaces produced by the two-dimensional generalized Kuramoto-Sivashinsky equation (1) and might be interesting to a broader circle of researchers working in the field of continuum systems with

complex nonlinear dynamics.

The scaling properties (96) of the saturated surface roughness indicate that additional large scale height variations of scale free character appear when the system size N is increased. The dynamics of these slow height variations can be investigated by analysing the time series of the fluctuating surface roughness $w(t)$ where the occurrence of slow modes with increasing system size can also be observed (see Fig. 21 and Fig. 22). This analysis shows that the resulting power-spectral densities (PSDs) can be expressed as the sum of a generalized Lorentzian and a constant, (128), or, in some cases, as two generalized Lorentzians (130), as shown in Figs. 24, 28 and 30.

The characteristic frequency f_0 obtained as a fit parameter corresponds to the smallest rate (largest time scale) that plays a role in the surface evolution. It can be attributed to the spatial mode of lowest wave number k_0 (which is inversely proportional to the system size) that can appear in the system. The dependence of this characteristic frequency on the system size gives the 'dispersion relation' $f_0(k_0)$ that connects spatial and temporal scales of surface dynamics. These relations have the power-law $f_0 \sim k_0^{\xi}$ character (see Fig. 27) for large systems (small k_0), suggesting that the underlying temporal behaviour is scale free. The exponent ξ is found to decrease with increasing value of parameter α. These results indicate that the dependence of the characteristic time scale of the dynamics on the parameter α changes with the spatial scale: on smaller spatial scales the characteristic time decreases very strongly with increasing α, whereas on large enough spatial scales the evolution is slower for smaller α.

It is hard to make rigorous conclusions regarding the connection between the exponent ξ and the dynamical exponent z found in scaling relations for interfaces (see, e.g., [35,51,77]). However, it is interesting to note that the value $\xi \approx 1.89$ obtained for the KS equation lies between the dynamical exponent values $z = 1.41$ of the the KPZ equation and $z = 2$ for Edwards-Wilkinson equation for two dimensions (see [51]).

The findings presented in this paper also raise some interesting questions for further research. For example, it is apparent from Fig. 26 and from the values of the PSD exponent β that the character of surface roughness dynamics depends quite strongly on parameter α. The question arises how temporal properties on various scales change with α and what are the statistical properties of the

apparent bursts observed for larger values of α.

The Lorentzian shape, $W(f) \sim (f_0^2 + f^2)^{-1}$, of the PSD and relation $f_0 \sim k_0^{\xi}$ with $\xi \approx 2$ for $\alpha \approx 0$ also suggests a possible analogy between the large-scale fluctuations of surface roughness and a diffusive process with the probability density Fourier transformed in space and time [78],

$$\hat{P}(k_0, f) \propto \frac{k_0^2}{(k_0^2 D)^2 + f^2} \,,$$

where D is the diffusion constant independent of the system size. This correspondence becomes apparent when $f_0 = Dk_0^2$ is substituted in (125). Thus, perhaps the slow kinetics of the surface roughness might even be reproduced by a random walk of a particle in some external potential which is implied by the fact that the process $w(t)$ is bounded and, consequently, k_0 does not go to zero for systems of finite size. For larger α values where the corresponding PSD exponent $\beta \approx 3$ and $\xi < 2$ this process would then correspond to anomalous diffusion. Moreover, the fact that, for some parameter values, one more generalized Lorentzian has to be added to the in order to fit the calculated PSD for large systems (see Figs. 28 and 29) suggests the emergence of one more time scale, or perhaps, the whole interval of time scales.

These changes in dynamics due to the increase of α can perhaps be attributed to the fact that Eq. (1) with larger α produces coarser and slower-evolving small-scale patterns (cells or bumps) whose corresponding dynamic time scales begin to significantly overlap with the time scales of the slow height variations. Any conclusive answers about both, the exact character and the occurrence mechanism, of these effects require more analytical work and data obtained from simulations on even larger systems.

In future work, it would be interesting to investigate the transition between the stationary long-time dynamics for small values of parameter α and non-stationary coarsening regime in the large α limit. Another interesting research direction concerns the distributions of surface height, global and local roughness [79–82] and how they change with α and scale with the system size. It would also be useful to know how all of these properties are influenced by noise.

8 Non-stationary local coarsening

The discussion in this work so far has been focused on the moderate parameter range $-0.12 \leq \alpha \leq 5$ of the gKS (98),

$$\partial_t h = -\nabla^2 h - \nabla^4 h - \alpha \nabla^2 (\nabla h)^2 + (\nabla h)^2 \,. \tag{131}$$

where, after a short (compared to the total observation time) transient period a stationary regime is reached (see Sect. 6).

Large parameter values (say, $\alpha > 20$), however, lead to the global coarsening of the surface patterns which is non-stationary in the sense that the temporal behavior does not converge to fluctuations about some average and, moreover, appears quite different for different realizations. As shown in Sect. 3, in the limit $\alpha \to \infty$ the gKS equation becomes equivalent to the cKS equation that produces coarsening pattern without saturation up until a single bump grows to the size spanning the whole finite system [52]. For finite parameter α values this coarsening comes to a halt at the point when the of humps in the coarse surface patterns reaches characteristic sizes that are only a few times smaller than the system size.

The behavior of gKS (131) in the intermediate parameter range, which can roughly be given as $6 < \alpha < 20$, shows another type of behavior that has not been previously reported. The dynamics observed in numerical simulations exhibits the following scenario illustrated in Fig. 31 for $\alpha = 10$. At first, the system seems to behave in the same way as is does for the moderate parameter range $-0.12 \leq \alpha \leq 5$ considered in earlier sections: after the initial linear instability that is manifested by the exponential growth of the surface roughness (see Sect. 2) followed by a short period of nonlinear coarsening and then by the saturation — where the system seems to behave in the stationary way (Sect. 3). In this part of the story, different realizations exhibit the same kinetics of surface roughness and other statistical parameters.

However, at later times which can be very different for different realizations, the system dynamics exhibits suddenly switches to very different kinetics: the roughness w starts to increase again and can grow up to several times larger than the 'saturation' value reached in the first part of the scenario. It is also

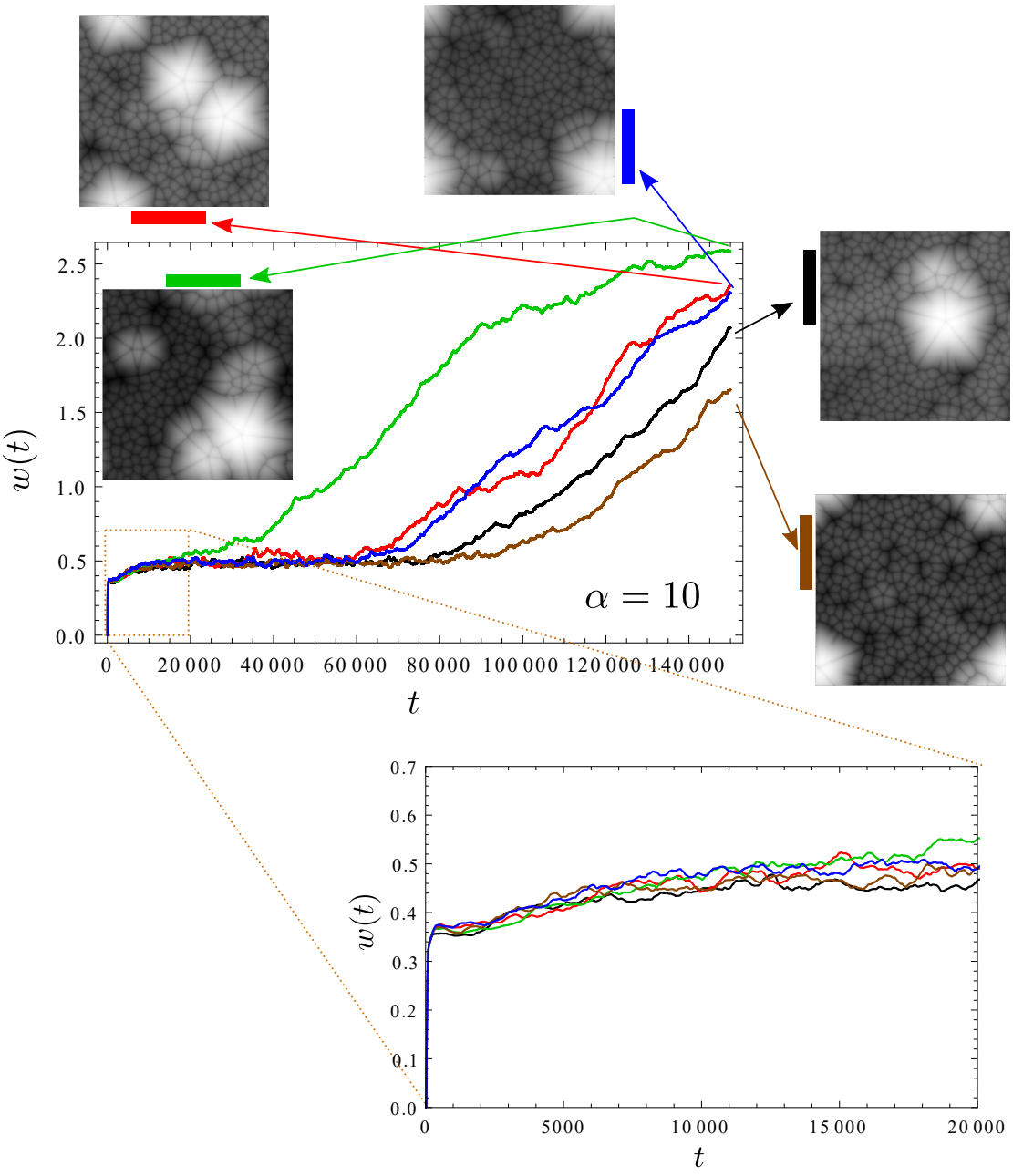

Figure 31: The kinetics of global surface roughness w for five different realizations with $\alpha = 10$ and system size $N = 500$ in lattice units ($L \approx 355$) up to $t = 150000$ and the corresponding surface profiles at the end of each realization. The initial part of the kinetics (up to $t = 20000$) is shown magnified.

interesting to note that, at the same time, the surface area remains virtually unchanged and has the same value for all realizations, see Fig. 32. This indicates coarsening of the pattern, that is, the growth of the characteristic length of the surface structure, as, for example, the scaling relation (115) in Sect. 5 indicates.

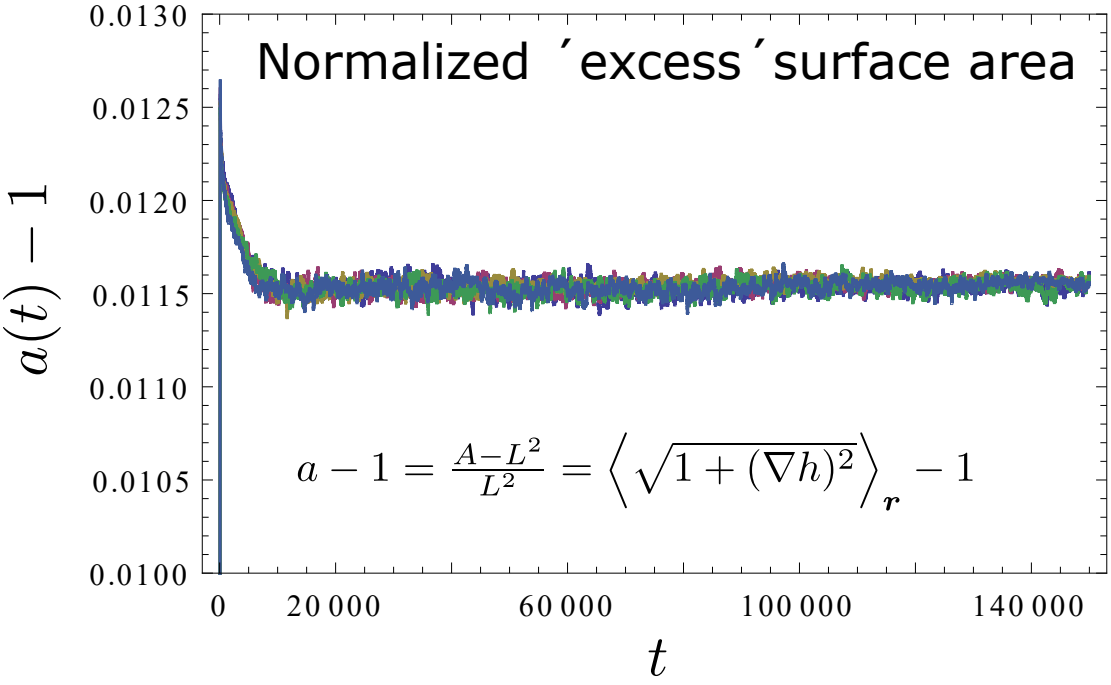

Figure 32: The kinetics of normalized excess surface area $a(t)-1$ defined in (114), Sect. 5, for the same five realizations shown in Fig. 31.

Looking at the surface profiles in Fig. 31 resulting from kinetics described above one notices peculiar local structures protruding from surfaces that otherwise have patterns similar to those observed for smaller parameter values discussed in earlier sections. The peculiar structures can perhaps be better appreciated when plotted in 3D. Fig. 33 shows an example of surface profiles from three different realizations with parameter $\alpha = 7.5$ and discretization step $\Delta x = 1$ at time $t = 200000$. The realizations are selected to demonstrate three different outcomes: no occurrence of local coarsening, late occurrence of two small local coarsening centers and occurrence of a single coarsening center early in the simulation resulting in one large structure.

8.1 Features of local coarsening behavior

The occurrence of the local coarsening has been systematically investigated by performing long simulations up to $t = 200000$ or, in some cases, $t = 300000$

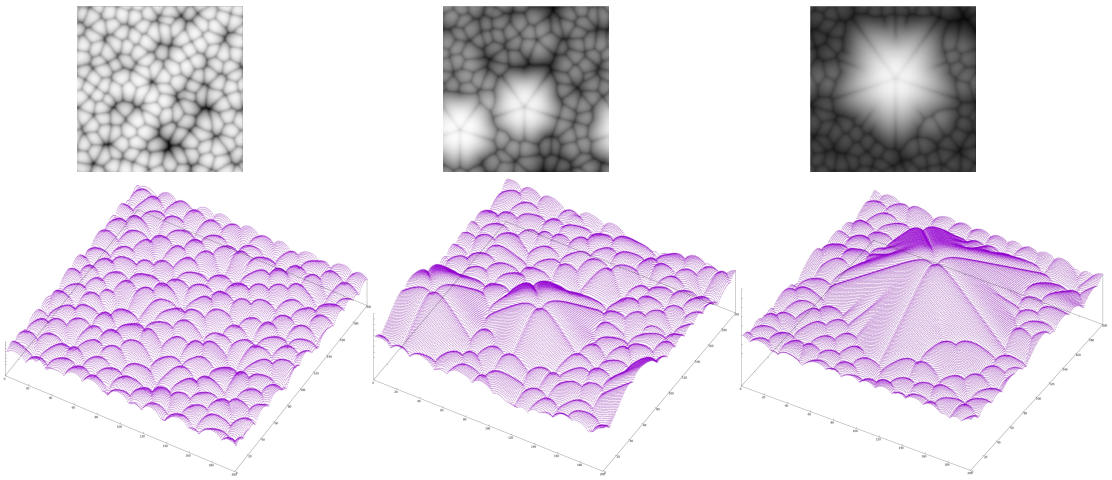

Figure 33: Three different outcomes from realizations with $N = 200$, $\Delta x = 1$ at $t = 200000$ for $\alpha = 7.5$.

for various combinations of parameter values $\alpha = 6,\ 6.5,\ 7,\ 7.5,\ 8,\ 9,\ 10,\ 25,\ 50$, spatial discretization step values $\Delta x = 0.71086127010534,\ 1$, time step values $\Delta t = 0.0025,\ 0.005,\ 0.008$, and noise levels (in stochastic case) $D = 0.0000005,\ 0.0000010,\ 0.0000020,\ 0.0000100$ [12], 5 realizations with different random initial surface profiles for each case. The main characteristics of the occurrence of the local coarsening can be summarized as follows:

- The local coarsening has been observed in the simulations of deterministic gKS with parameter values $6.5 \leq \alpha \leq 50$ occurring before the time $t = 200000$. For parameter values $\alpha \geq 8$, the local coarsening has occurred in all realizations performed, and for $6.5 \leq \alpha < 8$ it has appeared only in some realizations. For parameter values $\alpha \leq 6$ the local coarsening has not occurred in any of the realizations up to $t = 300000$.

- The probability of the occurrence of the local coarsening structures during the given simulation time appears to increase with increasing parameter value and decrease with increasing level of noise. The small number of realizations, of course, does not permit estimation of these probabilities with any reasonable accuracy, but these trends are quite visible, nevertheless.

- The locally initiated coarsening structures grow in diameter and height while their surroundings remain statistically similar, thus, forming large

[12]The stochastic case is obtained by adding the noise term η with noise power D, as defined in Sect. 2, Subsect. 2.3, p.33.

mounds in the surface profile. This also causes the global surface roughness to grow up to several times larger than the values measured before the appearance of local coarsening, see Fig. 35. The surface area, however, remains virtually unchanged at the same time.

8.2 Discussion

The behavior presented in this section has not, to the author's knowledge, been reported before in surface growth simulations or experiments. The reason for this might be the lack of research of the models with long enough simulation times, as those used in this work (see, for example, [66] where the simulation times of the 2D gKS are about 200 times shorter). The current experiments in amorphous surface growth also correspond only to the initial stages of surface growth, often hardly reaching the saturation regime as, for example, in [48,49]. The reason for the lack of experimentally observed structures of this type might also be the ever present thermal and deposition noise, since the noise has been found to reduce the probability of- or completely prevent the occurrence of local coarsening in the gKS model considered here, as well.

There are some obvious difficulties that hinder the systematic investigation of the local coarsening behavior. They can be summarized

- Extremely long simulation times are required to even reach the instances where the local coarsening occurs.

- Vastly different behavior results for different realizations with the same parameters, see Fig. 34. Therefore, many realizations are required in order to observe different possible scenarios in the simulation.

- The coarsening process is highly non-stationary, therefore it is almost impossible to make meaningful statements about its dynamics by investigating the kinetics of its global quantities using traditional statistical measures. The process, however, still has many active degrees of freedom which prevents the use of methods developed for dynamical systems.

- The statistical description of surface profiles is also unavailable, because the locally coarse structures eventually grow to the size spanning of the

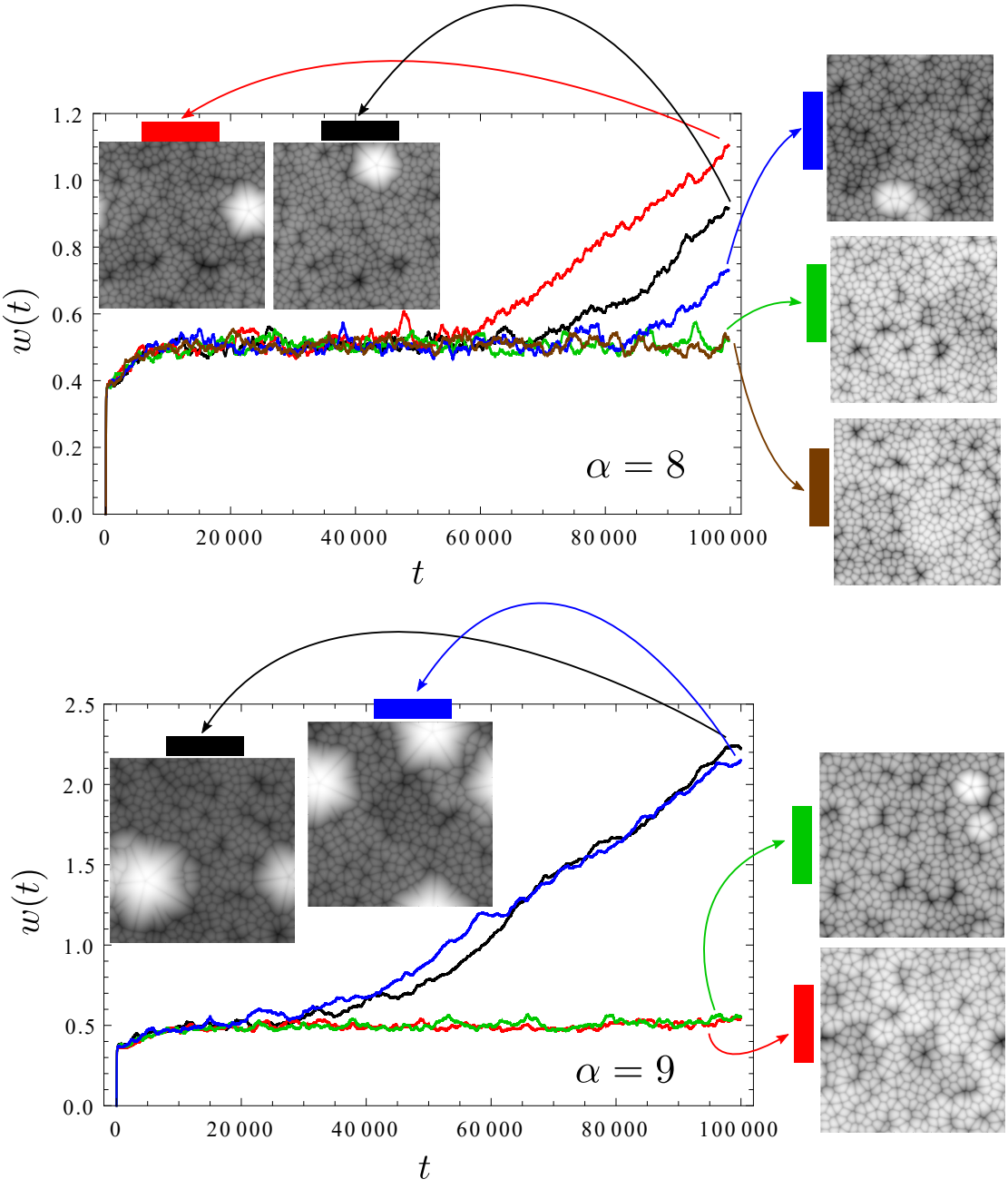

Figure 34: The kinetics of global surface roughness w for different realizations with $\alpha = 8$ (top panel) and $\alpha = 9$ (bottom panel), system size $N = 500$ in lattice units ($L \approx 355$) up to $t = 100000$ and the corresponding surface profiles at the end of each realization.

whole system and making the statistical description using the height distributions and correlations virtually useless.

For the reasons listed above, this section mainly consists of illustrative examples and qualitative description of the local coarsening.

One must not forget that all these peculiar effects might be the glitch of the numerical scheme used in computer simulations. There are, nevertheless, several arguments supporting the belief that the effects demonstrated in this section follow from the model itself and are not merely some artifacts of the numerical scheme: [13]

- The near-exact pentagonal symmetry at the center of the most locally growing coarse structures does not match the symmetry of the square lattice used for numerical integration, as one would expect for a glitch due to the spatial discretization. Also, no visible changes in the patterns occur when the spatial discretization step Δx is varied.

- The variation of the time step Δt in the finite difference scheme also does not seem to influence the observed behavior.

- The observed local coarsening does not produce any 'explosion' effects — all this growth seems to happen smoothly over very long simulation times which makes it hard to come up with any accumulation mechanism of numerical errors.

[13] Or, if they are, indeed, just artifacts, they are interesting, nevertheless, and seem not to be reported.

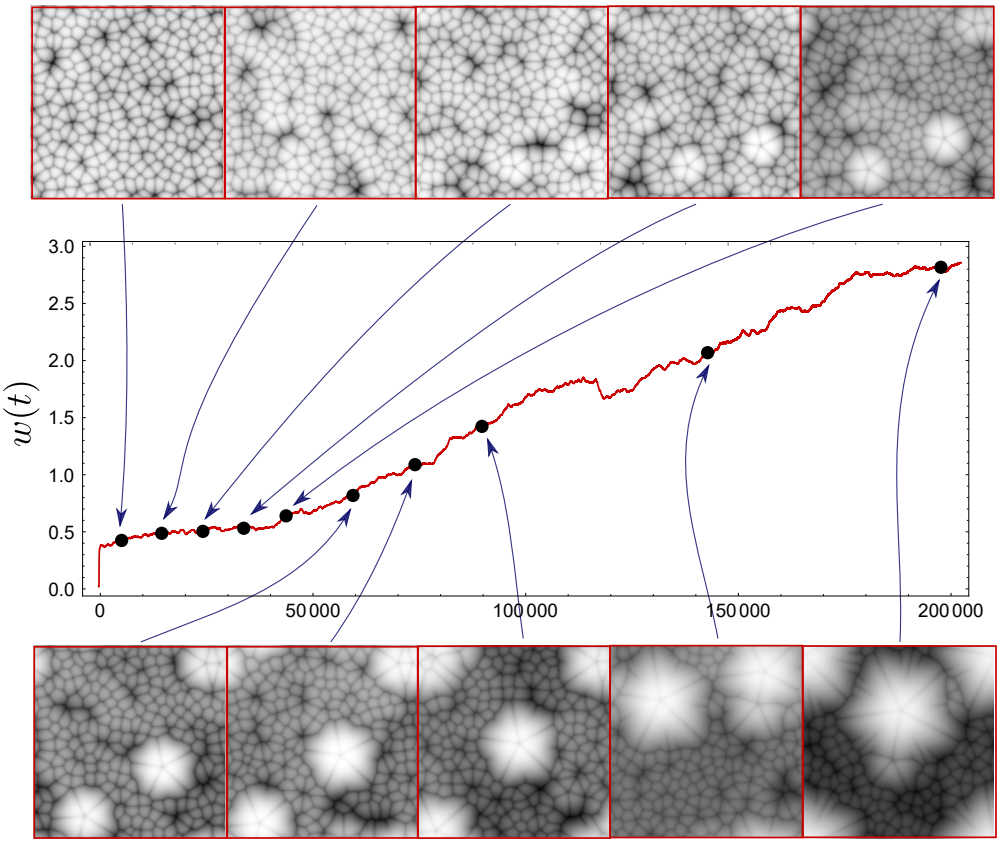

Figure 35: The kinetics of global surface roughness w for a single realization with $\alpha = 10$ and system size $N = 300$ in lattice units (also $L = 300$) up to $t = 200000$ and the corresponding surface profiles at different times are also shown in order to demonstrate the occurrence of the local coarsening. Here, a different spatial discretization step $\Delta x = 1$ has been used (instead of $\Delta x \approx 0.71086$ used in all previous simulations).

9 Conclusions

This short section summarizes the main results presented in this dissertation by providing several conclusions that could be drawn from the overwhelming variety of results obtained during the research conducted by the author.

The list of conclusions goes as follows:

1. The model for amorphous solid film growth based on the generalized two-dimensional Kuramoto-Sivashinsky equation (gKS) produces surfaces whose morphologies consist of disordered cellular patterns with characteristic length on small scales and slow height variations of self-affine character on large scales. The latter long range variations become more pronounced only at large system sizes.

2. The dynamics of surface evolution and the statistical properties of the resulting surface morphologies are determined by a single independent parameter of the rescaled growth equation. In the limit of zero parameter value this equation becomes the well known Kuramoto-Sivashinsky (KS) equation that produces stationary chaotic behavior and supposedly belongs to the KPZ universality class. At small nonnegative parameter values gKS also exhibits stationary spatio-temporal chaos typical for KS. Increasing the parameter value produces surfaces saturating at coarser patterns with less pronounced long range height variations.

3. The observed scaling behavior of the saturated surface roughness strongly suggests the power-law shape of the surface spectrum at small wave numbers and, thus, indicates self-affine character of the long range height variations. The scaling behavior obtained from numerical simulations of gKS shows strong dependence on the equation parameter up to the largest system sizes used: while in the KS limit the numerically obtained scaling behavior corresponds to the EW universality class which is pre-asymptotic (in terms of system size) of the expected KPZ behavior, larger parameter values in gKS produce qualitatively different apparent scaling. This observed scaling must therefore be the result of of the finite system size, be-

cause scaling arguments suggest that this parameter should not influence the large scale behavior.

4. Even larger parameter values result in surface evolution where no saturation in the KS sense takes place and, in the limit of infinite parameter values, different rescaling of gKS produces an equation known as the conserved Kuramoto-Sivashinsky (cKS) equation whose evolution consists in non-stationary coarsening of the cellular pattern which is limited only by the finite system size.

5. As mentioned above, for a range parameter values, the disordered cellular surface pattern is found to saturate at some particular average cell size (characteristic length) that depends on the parameter value. A scaling relation has been found that connects this characteristic length to the surface roughness and the surface surface area showing that the cellular patterns are statistically similar at different parameter values also allowing for a quick and quite accurate estimation of the characteristic length without direct calculation using 2D FFT or height autocorrelation functions.

6. Increasing the system size, new long range modes appear. By analyzing the autocorrelations and spectra of the global surface roughness, it is possible to connect the observed the time scales of the global dynamics to the system size, i.e. to relate spatial and temporal properties of the system. The relation appears to have a power-law shape for large systems in a range of parameter values investigated. The value of the exponent of this power law that must be related to its dynamic exponent has been found to vary quite strongly depending on the parameter value indicating that the regime of universal dynamics expected for asymptotically large systems has not been reached at the system sizes considered in this work.

7. For larger parameter values, the break-down of stationary saturated surface dynamics has been observed. This sudden change of behavior has been observed in a wide range of parameter values and can be attributed to the occurrence of locally growing coarse structures. The individual locally coarse structures appear to have to same pentagonal symmetry for different combinations of simulation parameters. The local coarsening starts at vastly varying times and follows different scenarios for different realiza-

tions during the simulation, depending on the detailed initial conditions for each realization. Adding the stochastic noise term to the gKS seems to reduce the probability of occurrence of local coarsening and prevent it altogether for higher nose levels. The stability of these effects against the varying spatial and temporal discretization steps, also the fact that the occurring structures do not follow the symmetry of the lattice seem to support the notion that they are not just some artifact of numerical integration. Even if the local coarsening were an artifact of the numerical simulation, it is, nevertheless, quite interesting and previously unreported.

Bibliography

1. E. C. Harris, *Principles of archaeological stratigraphy* (Elsevier, 2014).

2. G. S. May, S. M. Sze, *Fundamentals of Semiconductor Fabrication* (New York: John Wiley & Sons, 2004).

3. S. Bae, H. Kim, Y. Lee, X. Xu, J.-S. Park, Y. Zheng, J. Balakrishnan, T. Lei, H. R. Kim, Y. I. Song, et al., Roll-to-roll production of 30-inch graphene films for transparent electrodes, Nature nanotechnology **5**(8), 574–578 (2010).

4. M. C. Cross, P. C. Hohenberg, Pattern formation outside of equilibrium, Rev. Mod. Phys. **65**, 851–1112 (1993).

5. M. Castro, R. Cuerno, M. Nicoli, L. V?zquez, J. G. Buijnsters, Universality of cauliflower-like fronts: from nanoscale thin films to macroscopic plants, New Journal of Physics **14**(10), 103039 (2012).

6. M. Hairer, Solving the kpz equation, Annals of Mathematics **Volume 178**(Number 2), 559–664 (2013).

7. V. Juknevicius, Long range height variations in surface growth, The European Physical Journal B **89**(2), 1–8 (2016).

8. M. Raible, S. Mayr, S. Linz, M. Moske, K. Samwer, et al., Amorphous thin-film growth: Theory compared with experiment, EPL (Europhysics Letters) **50**(1), 61 (2000).

9. M. Raible, S. J. Linz, P. Hänggi, Amorphous thin film growth: Effects of density inhomogeneities, Physical Review E **64**(3), 031506 (2001).

10. M. Raible, S. J. Linz, P. Hänggi, Growth instabilities of vapor deposited films: atomic size versus deflection effect, The European Physical Journal B-Condensed Matter and Complex Systems **27**(3), 435–442 (2002).

11. R. Cuerno, A.-L. Barabási, Dynamic scaling of ion-sputtered surfaces, Physical review letters **74**(23), 4746 (1995).

12. T. Kim, C.-M. Ghim, H. Kim, D. Kim, D. Noh, N. Kim, J. Chung, J. Yang, Y. Chang, T. Noh, et al., Kinetic roughening of ion-sputtered pd (001)

surface: beyond the kuramoto-sivashinsky model, Physical review letters **92**(24), 246104 (2004).

13. M. Castro, R. Cuerno, L. Vázquez, R. Gago, Self-organized ordering of nanostructures produced by ion-beam sputtering, Physical review letters **94**(1), 016102 (2005).

14. R. Gago, L. Vázquez, O. Plantevin, T. H. Metzger, J. Muñoz-García, R. Cuerno, M. Castro, Order enhancement and coarsening of self-organized silicon nanodot patterns induced by ion-beam sputtering, Applied physics letters **89** (2006).

15. R. Cuerno, M. Castro, J. Muñoz-García, R. Gago, L. Vázquez, Nanoscale pattern formation at surfaces under ion-beam sputtering: A perspective from continuum models, Nuclear Instruments and Methods in Physics Research Section B: Beam Interactions with Materials and Atoms **269**(9), 894–900 (2011).

16. J. Muñoz-García, R. Cuerno, M. Castro, Short-range stationary patterns and long-range disorder in an evolution equation for one-dimensional interfaces, Physical Review E **74**(5), 050103 (2006).

17. J. Muñoz-García, R. Gago, L. Vázquez, J. A. Sánchez-García, R. Cuerno, Observation and modeling of interrupted pattern coarsening: surface nanostructuring by ion erosion, Physical review letters **104**(2), 026101 (2010).

18. G. Sivashinsky, Nonlinear analysis of hydrodynamic instability in laminar flames i. derivation of basic equations, Acta astronautica **4**(11-12), 1177–1206 (1977).

19. D. Michelson, G. Sivashinsky, Nonlinear analysis of hydrodynamic instability in laminar flames ii. numerical experiments, Acta Astronautica **4**(11-12), 1207–1221 (1977).

20. G. Sivashinsky, On self-turbulization of a laminar flame, Acta Astronautica **6**(5-6), 569–591 (1979).

21. Y. Kuramoto, *Chemical oscillations, waves, and turbulence* (Springer-Verlag, 1984).

22. K. Sneppen, J. Krug, M. Jensen, C. Jayaprakash, T. Bohr, Dynamic scaling and crossover analysis for the kuramoto-sivashinsky equation, Physical Review A **46**(12), R7351 (1992).

23. C. Jayaprakash, F. Hayot, R. Pandit, Universal properties of the two-dimensional kuramoto-sivashinsky equation, Physical review letters **71**(1), 12 (1993).

24. B. M. Boghosian, C. C. Chow, T. Hwa, Hydrodynamics of the kuramoto-sivashinsky equation in two dimensions, Physical Review Letters **83**(25), 5262 (1999).

25. M. Paniconi, K. Elder, Stationary, dynamical, and chaotic states of the two-dimensional damped kuramoto-sivashinsky equation, Physical Review E **56**(3), 2713 (1997).

26. M. Rost, J. Krug, Anisotropic kuramoto-sivashinsky equation for surface growth and erosion, Physical review letters **75**(21), 3894 (1995).

27. K. B. Lauritsen, R. Cuerno, H. A. Makse, Noisy kuramoto-sivashinsky equation for an erosion model, Physical Review E **54**(4), 3577 (1996).

28. K. Dreimann, S. J. Linz, Continuum modeling of ion-beam eroded surfaces under normal incidence: Impact of stochastic fluctuations, Chemical Physics **375**(2), 606–611 (2010).

29. C. Diddens, S. J. Linz, Continuum modeling of particle redeposition during ion-beam erosion, The European Physical Journal B **86**(9), 1–13 (2013).

30. C. Diddens, S. J. Linz, Continuum modeling of particle redeposition during ion-beam erosion, The European Physical Journal B **88**(7), 1–22 (2015).

31. V. Yakhot, Large-scale properties of unstable systems governed by the kuramoto-sivashinksi equation, Physical Review A **24**(1), 642 (1981).

32. I. Procaccia, M. H. Jensen, V. S. L'vov, K. Sneppen, R. Zeitak, Surface roughening and the long-wavelength properties of the kuramoto-sivashinsky equation, Physical Review A **46**(6), 3220 (1992).

33. M. Kardar, G. Parisi, Y.-C. Zhang, Dynamic scaling of growing interfaces, Physical Review Letters **56**(9), 889 (1986).

34. M. J. Vold, Computer simulation of floc formation in a colloidal suspension, Journal of Colloid Science **18**(7), 684–695 (1963).

35. F. Family, T. Vicsek, Scaling of the active zone in the eden process on percolation networks and the ballistic deposition model, Journal of Physics A: Mathematical and General **18**(2), L75 (1985).

36. S. Wolfram, Cellular automaton fluids 1: Basic theory, Journal of statistical physics **45**(3), 471–526 (1986).

37. U. Frisch, B. Hasslacher, Y. Pomeau, Lattice-gas automata for the navier-stokes equation, Physical review letters **56**(14), 1505 (1986).

38. B. J. Wylie, Application of two-dimensional cellular automaton lattice-gas models to the simulation of hydrodynamics (1990).

39. J.-P. Rivet, J. P. Boon, *Lattice gas hydrodynamics*, volume 11 (Cambridge University Press, 2005).

40. V. Jukneviciu̇s, J. Armaitis, Lattice gas automaton modelling of a vortex flow meter: Strouhal-reynolds number dependence, arXiv preprint arXiv:1701.08754 (2017).

41. V. L'vov, I. Procaccia, Comment on "universal properties of the two-dimensional kuramoto-sivashinsky equation", Physical review letters **72**(2), 307 (1994).

42. C. Jayaprakash, F. Hayot, R. Pandit, Jayaprakash, hayot, and pandit reply, Physical review letters **72**(2), 308 (1994).

43. M. Nicoli, E. Vivo, R. Cuerno, Kardar-parisi-zhang asymptotics for the two-dimensional noisy kuramoto-sivashinsky equation, Physical Review E **82**(4), 045202 (2010).

44. P. Manneville, H. Chaté, Phase turbulence in the two-dimensional complex ginzburg-landau equation, Physica D: Nonlinear Phenomena **96**(1), 30–46 (1996).

45. S. F. Edwards, D. Wilkinson, The surface statistics of a granular aggregate, in *Proceedings of the Royal Society of London A: Mathematical, Physical and Engineering Sciences* (The Royal Society, 1982), volume 381, 17–31.

46. T. Nattermann, L.-H. Tang, Kinetic surface roughening. i. the kardar-parisi-zhang equation in the weak-coupling regime, Physical Review A **45**(10), 7156 (1992).

47. V. Juknevičius, J. Ruseckas, J. Armaitis, Large scale spatio-temporal behaviour in surface growth, The European Physical Journal B **90**(9), 163 (2017).

48. B. Reinker, M. Moske, K. Samwer, Kinetic roughening of amorphous zr 65 al 7.5 cu 27.5 films investigated in situ with scanning tunneling microscopy, Physical Review B **56**(15), 9887 (1997).

49. S. Mayr, M. Moske, K. Samwer, Identification of key surface processes for vapor deposited amorphous metallic film growth, in *Journal of Metastable and Nanocrystalline Materials* (Trans Tech Publ, 2000), volume 8, 221–230.

50. S. Mayr, K. Samwer, Tailoring the surface morphology of amorphous thin films by appropriately chosen deposition conditions, Journal of applied physics **91**(5), 2779–2784 (2002).

51. A.-L. Barabási, H. E. Stanley, *Fractal concepts in surface growth* (Cambridge university press, 1995).

52. M. Raible, S. J. Linz, P. Hänggi, Amorphous thin film growth: Minimal deposition equation, Physical Review E **62**(2), 1691 (2000).

53. M. Raible, S. J. Linz, P. Haenggi, Amorphous thin film growth simulation methods for stochastic deposition equations, Acta Physica Polonica B **33**, 1049 (2002).

54. S. G. Mayr, M. Moske, K. Samwer, M. E. Taylor, H. A. Atwater, The role of particle energy and pulsed particle flux in physical vapor deposition and pulsed–laser deposition, Applied Physics Letters **75**(26), 4091–4093 (1999).

55. S. Mayr, M. Moske, K. Samwer, Identification of key parameters by comparing experimental and simulated growth of vapor-deposited amorphous zr 65 al 7.5 cu 27.5 films, Physical Review B **60**(24), 16950 (1999).

56. S. Mayr, K. Samwer, Model for intrinsic stress formation in amorphous thin films, Physical review letters **87**(3), 036105 (2001).

57. W. M. Tong, R. S. Williams, Kinetics of surface growth: phenomenology, scaling, and mechanisms of smoothening and roughening, Annual Review of Physical Chemistry **45**(1), 401–438 (1994).

58. P. Meakin, Fractals, scaling and growth far from equilibrium (1998).

59. S. Facsko, T. Bobek, A. Stahl, H. Kurz, T. Dekorsy, Dissipative continuum model for self-organized pattern formation during ion-beam erosion, Physical Review B **69**(15), 153412 (2004).

60. S. Vogel, S. J. Linz, Continuum modeling of sputter erosion under normal incidence: Interplay between nonlocality and nonlinearity, Physical Review B **72**(3), 035416 (2005).

61. S. Vogel, S. J. Linz, How ripples turn into dots: modeling ion-beam erosion under oblique incidence, EPL (Europhysics Letters) **76**(5), 884 (2006).

62. N. J. Shevchik, Growth instabilities in the deposition of amorphous films, Journal of Non-Crystalline Solids **12**(2), 141–149 (1973).

63. A. Mazor, D. Srolovitz, P. Hagan, B. Bukiet, Columnar growth in thin films, Physical Review Letters **60**(5), 424 (1988).

64. W. W. Mullins, Theory of thermal grooving, Journal of Applied Physics **28**(3), 333–339 (1957).

65. P. E. Kloeden, E. Platen, H. Schurz, *Numerical solution of SDE through computer experiments* (Springer Science & Business Media, 2012).

66. J. Muñoz-García, R. Cuerno, M. Castro, Coupling of morphology to surface transport in ion-beam-irradiated surfaces: normal incidence and rotating targets, Journal of Physics: Condensed Matter **21**(22), 224020 (2009).

67. M. Castro, R. Cuerno, Comment on "kinetic roughening of ion-sputtered pd (001) surface: beyond the kuramoto-sivashinsky model", Physical review letters **94**(13), 139601 (2005).

68. O. Bikondoa, D. Carbone, V. Chamard, T. H. Metzger, Ion beam sputtered surface dynamics investigated with two-time correlation functions: a model study, Journal of Physics: Condensed Matter **24**(44), 445006 (2012).

69. G. Palasantzas, Roughness spectrum and surface width of self-affine fractal surfaces via the k-correlation model, Physical Review B **48**(19), 14472 (1993).

70. Numericana. Knud Thomsen (2004), `http://www.numericana.com/answer/ellipsoid.htm`, accessed: 2017-08-20.

71. M. S. Klamkin, Elementary approximations to the area of n-dimensional ellipsoids, The American Mathematical Monthly **78**(3), 280–283 (1971).

72. J.-P. Eckmann, S. O. Kamphorst, D. Ruelle, Recurrence plots of dynamical systems, EPL (Europhysics Letters) **4**(9), 973 (1987).

73. J. Gao, H. Cai, On the structures and quantification of recurrence plots, Physics Letters A **270**(1), 75–87 (2000).

74. N. Marwan, M. C. Romano, M. Thiel, J. Kurths, Recurrence plots for the analysis of complex systems, Physics reports **438**(5), 237–329 (2007).

75. H. Kantz, T. Schreiber, *Nonlinear time series analysis*, volume 7 (Cambridge university press, 2004).

76. A. M. Yaglom, *An introduction to the theory of stationary random functions* (Courier Corporation, 2004).

77. K. B. Lauritsen, H. C. Fogedby, Critical exponents from power spectra, Journal of statistical physics **72**(1-2), 189–205 (1993).

78. N. G. Van Kampen, *Stochastic processes in physics and chemistry*, volume 1 (Elsevier, 1992).

79. G. Foltin, K. Oerding, Z. Rácz, R. L. Workman, R. K. P. Zia, Width distribution for random-walk interfaces, Phys. Rev. E **50**, R639–R642 (1994).

80. Z. Rácz, M. Plischke, Width distribution for (2+1)-dimensional growth and deposition processes, Phys. Rev. E **50**, 3530–3537 (1994).

81. T. Antal, M. Droz, G. Györgyi, Z. Rácz, Roughness distributions for $1/f^{\alpha}$ signals, Phys. Rev. E **65**, 046140 (2002).

82. F. A. Reis, Scaling of local roughness distributions, Journal of Statistical Mechanics: Theory and Experiment **2015**(11), P11020 (2015).

List of publications and presentations

Full text publications

The research covered in this dissertation and related topics has been presented in 3 publications listed below.

A1. **V. Juknevicius**, Long range height variations in surface growth, European Physical Journal B **89**(2), 1-8 (2016).

A2. **V. Juknevicius**, J. Armaitis, Lattice gas automaton modeling of a vortex flow meter: Strouhal-Reynolds number dependence, Lith. J. Phys. 56, 191–199 (2016).

A3. **V. Juknevicius**, J. Armaitis, J. Ruseckas, Large scale spatio-temporal behavior in surface growth, European Physical Journal B **90**(9) 163 (2017).

Conference presentations

The research covered in this dissertation was communicated in 6 conference presentations of which 3 were talks and 3 posters presented by the author. The list, in reverse chronological order, follows.

B1. V. Juknevičius, Long-range height variations and kinetics of roughness in surface growth, in *42-oji Lietuvos nacionalinė fizikos konferencija: Programa ir pranešimų tezės* (Vilnius, Lithuania, 2017), p. 106. // Poster by V. Juknevičius

B2. V. Juknevičius, Long range height variations in surface growth, in *Perspectives in Nonlinear Dynamics 2016* (Berlin, Germany, July 25-29 2016). // Oral presentation by V. Juknevičius

B3. V. Juknevičius, Scaling in Generalized 2D Kuramoto-Sivashinsky Equations, in *Perspectives in Nonlinear Dynamics 2016* (Berlin, Germany, July 25-29 2016). // Poster by V. Juknevičius

B4. V. Juknevičius, Apibendrintųjų Kuramoto-Sivashinsky lygčių savybės mastelio keitimo atžvilgiu, in *41-oji Lietuvos nacionalinė fizikos konferencija: Programa ir pranešimų tezės* (Vilnius, Lithuania, 2015), p. 358. // Poster by V. Juknevičius

B5. V. Juknevičius, Long-range scaling in generalized Kuramoto-Sivashinsky equations, in *Open Readings 2015* (Vilnius, Lithuania, 2015), p. 91. // Oral presentation by V. Juknevičius

B6. V. Juknevičius, Koreliacijos ilgais atstumais dvimačių apibendrintųjų Kuramoto-Sivashinsky lygčių generuojamuose paviršiuose, in *Penktoji jaunųjų mokslininkų konferencija "Fizinių ir technologijos mokslų tarpdalykiniai tyrimai*" (Vilnius, Lithuania, 2014), p. 17. // Oral presentation by V. Juknevičius. Selected as one of the best presentations in the conference

Two more poster presentations by the author related to another research topic have been presented in conferences during the same time period.

C1. V. Juknevičius, J. Ruseckas, B. Kaulakys, Impulsiniai procesai ir 1/f triukšmas netvarkiose medžiagose, in *41-oji Lietuvos nacionalinė fizikos konferencija: Programa ir pranešimų tezės* (Vilnius, Lithuania, 2015), p. 357. // Poster by V. Juknevičius

C2. V. Juknevičius, J. Ruseckas, B. Kaulakys, $1/f^{\beta}$ fluctuations from sequences of rectangular pulses, in *7th International Conference on Unsolved Problems on Noise* (Barcelona, Spain, July 13-17 2015) // Poster by V. Juknevičius presented by co-author

Personal contribution of the author

The author of the dissertation has chosen the topic of the research, formulated its directions, selected and reviewed the scientific publications related to the research, written the software for the computer simulations of surface growth and performed all of the numerical simulations as well as the analytical derivations, data analysis, interpretation and visualization presented in this dissertation.

All scientific results presented in this work, except for the ones cited from the list of references, have been obtained by the author of this thesis.

Acknowledgements

First and foremost, I would like to express my gratitude to my supervisor Prof. Bronislovas Kaulakys who has tolerated my rebellious spirit and uncanny resistance to work on the problems related to the $1/f$-noise.

I would also like to thank Prof. Stafan J. Linz (University of Münster, Germany) for first introducing me to the field of continuum surface growth models in general and to the generalized Kuramoto-Sivashinsky equation in particular. I am very grateful to Christian Diddens (University of Twente, The Netherlands) for easing my start into this field by conveying his conceptual knowledge of the subject and helping with some technical details.

Many thanks go to my colleagues and collaborators Jogundas Armaitis and Julius Ruseckas for valuable discussions and efficient team work while producing journal publications and corresponding to the referees, also, perhaps, even more importantly, for providing some much needed guidance at times of difficulties in the research. On top of that, I am very thankful to Jogundas also for being a great friend who always offered constructive advice, computational power and moral support when they were most needed.

I would like to express many thanks to my other colleagues for a variety reasons: to Rytis Kazakevičius for generating cheerful atmosphere and frequent comic reliefs at the workplace, to Tomas Andrijauskas for stimulating general discussions about mathematics, computing and music at our occasional visits to some pub after work, to Viktor Novičenko for many useful and interesting discussions concerning the current work and science in general and for being a ping-pong partner of comparable skills, to Aleksejus Kononovičius for sharing his experience in writing publications and for giving some advice on writing this thesis, to Aušra Vektarienė for friendly moral support during the periods when I had little hope of ever successfully finishing my PhD studies.

I am enormously thankful to my best friend Vytautas Matulevičius (who would, perhaps, find this acknowledgement funny in at least 42 ways) for all kinds of help, support, for many joyful moments and for making the last more than 16 years of my life — ever since we have become good friends — much happier and way more intellectually fulfilling than it would otherwise have been.

I have countless other friends to thank who, each in their own way — directly or indirectly — helped me through the years of my studies: Remigijus Senavaitis, Martynas Pelakauskas, Robert Müller, Jonas Fuchs, Mantas Tarolis, Povilas Rastenis, Justinas Bareikis, Augustas Gaučas (Žuvis), Ieva Linkevičiūtė, Kamilė Michailovskytė, Laima Zlatkutė, Justina Jatkauskaitė, to name just a few.

I am also thankful to that complex network of forces in Nature for causing me and Monika to find each other... twice that night, because we haven't lost each other ever since.

At last, I would like to thank my parents for conceiving me and for supporting me afterwards, throughout my whole life so far, also, for believing in me more than I believed in myself during all these long years of my seemingly never-ending education. Also, I thank my brother for the hospitality, occasional advice and motivation by word and by example.